MEASUREMENTS AND MONTE CARLO SIMULATIONS OF X-RAY BEAMS IN RADIOSURGERY

by

Katharina E. Sixel

Department of Physics

McGill University, Montréal

June 1993

A Thesis submitted to the

Faculty of Graduate Studies and Research

in partial fulfillment of the requirements for the degree of

Doctor of Philosophy

ISBN 0-315-91715-6

Canada

Shortened title:

Measurements and Monte Carlo simulations of x-ray beams

ABSTRACT

Radiosurgery is characterized by high radiation doses, delivered via small diameter radiation beams in a single session, placing stringent requirements on the numerical and spatial accuracy of dose delivery to the target volume within the brain. In this thesis, physical and clinical aspects of radiosurgery are discussed, including a method for the production of cylindrical dose distributions with rectangular beams using cylindrical dynamic rotation.

The measurements of radiosurgical x-ray beam parameters are presented. Monte Carlo simulations determine that a measured increase in depth of dose maximum with increasing field size is a result of primary dose deposition in phantom for small diameter beams.

An analytical representation based on a curve-fitting process is developed to parametrize radiosurgical x-ray beam percentage depth doses as a function of depth in phantom, field diameter and beam energy using bi-exponential and polynomial functions.

Measurements of dose in the build-up region of x-ray beams ranging from 1x1 cm^2 to 30x30 cm^2 show that the depth of dose maximum increases rapidly with increasing field size at small fields, reaches a maximum around 5x5 cm^2 and then gradually decreases with increasing field size for large fields. Monte Carlo simulations attribute the effect observed at large fields to the scatter contamination of the primary beam from the linac head. This scatter contamination is measured by a half-block technique and further experiments show that it consists of electrons originating in the flattening filter of the linac.

RÉSUMÉ

La radiochirurgie est caractérisée par des doses élevées de radiation, administrées par des faisceaux de faibles diamètres, lors d'une session unique. Cela nécessite une administration au volume-cible à l'intérieur du cerveau d'une dose rigoureusement exacte numériquement et spatialement. Dans cette thèse, les aspects physiques et cliniques de la radiochirurgie sont discutés, y compris une méthode de production de distributions de doses cylindriques avec des faisceaux rectangulaires en utilisant une rotation dynamique cylindrique.

Nous présentons les mesures des paramètres du faisceau de rayons X de radiochirurgie. Des simulations de Monte Carlo sont utilisées pour démontrer que l'augmentation mesurée de la profondeur de dose maximale avec l'agrandissement du champ résulte d'une déposition de dose primaire dans le fantôme pour des faisceaux de radiochirurgie de faibles diamètres.

Nous développons une représentation basée sur un procédé d'ajustement analytique pour obtenir les paramètres du rendement en profondeur du faisceau de photons de radiochirurgie en fonction de la profondeur dans le fantôme, du diamètre du champ et de l'énergie du faisceau.suivant des fonctions bi-exponentielles et polynomiales.

Les mesures de doses dans la région entre la surface d'entrée et le point de dose maximale pour des faisceaux de rayons X allant de 1x1 cm^2 à 30x30 cm^2 montrent que pour une énergie donnée, la profondeur de la dose maximale augmente rapidement avec l'augmentation de la grandeur du champ pour les petits champs, atteint un maximum autour de 5x5cm^2 puis décroit graduellement avec l'agrandissement des champs pour les grands champs. Les simulations de Monte Carlo montrent que pour les grands

champs, l'effet provient de la contamination du faisceau primaire par la diffusion du faisceau dans la tête de l'accélérateur. La technique du demi-bloc permet de mesurer cette contamination de diffusion et des expériences subséquentes montrent qu' elle est composée d'électrons provenant du filtre égalisateur de l'accélérateur.

ACKNOWLEDGEMENTS

I sincerely thank my supervisor, Dr. E.B. Podgorsak for the opportunity to work with him, and for his guidance and support during the course of my research. He has given me the freedom to do independent work, and yet has always been available for assistance when needed.

I am grateful to all members of the Medical Physics department at the Montreal General Hospital for numerous and valuable discussions on various aspects of this thesis. It was a pleasure to work in such a dynamic environment. In particular, my collaboration with Dr. Wieslaw Wierzbicki proved to be an enjoyable and successful endeavour. Many thanks are also due to Mmes Lysanne Normandeau and Micheline Gosselin for their efforts in translating the abstract.

Financial support was received from the National Sciences and Engineering Research Council of Canada for the first two years of study, and through Dr. Podgorsak from the Medical Research Council of Canada for my final year. As well, the Physics department and the Medical Physics Unit provided financial reimbursement for student teaching assistance. The financial support from all sources is gratefully acknowledged.

Finally, I thank those whose support and love, as always, matters the most: my husband Robert Henry, and my parents Margrit and Friedrich Sixel.

PREFACE

The research described in this thesis has been carried out independently by the author under the supervision of Dr. E.B. Podgorsak in the Medical Physics department of the Montreal General Hospital, a teaching hospital of McGill University. The work constitutes an original contribution to the field of medical physics in general and to radiosurgery in particular. Several aspects of this work have already been presented at national (1,2,3) or international (4,5,6) medical physics meetings and also have been published as abstracts in conference proceedings (7,8,9) or in the journal *Medical Physics* (10,11,12). In addition, some results have recently been published (13,14,15) or accepted for publication (16,17) as refereed papers in various medical physics journals.

The thesis is divided into eight chapters, with *Chapters 4* through *7* representing the main body of the work. Each chapter deals with a particular experimental aspect of radiosurgery and/or x-ray beams. *Chapter 1* serves as a general introduction to the field of radiosurgery, giving the physical and clinical background. *Chapters 2* and *3* introduce experimental techniques and apparatus used throughout the work described in subsequent chapters. *Chapter 8* represents the final summary and conclusions of the thesis.

A means of irradiating cylindrical radiosurgical targets is presented in *Chapter 4*. This concept was introduced in the author's Master of Science thesis, and subsequent quantitative measurements given here prove the validity of the technique. The cylindrical dynamic rotation is unique in that it introduces two further degrees of freedom to a radiosurgical technique: the collimator rotation and variable field size. The

measured dose distributions resulting from an implementation of cylindrical dynamic rotation clearly show that even high level isodose surfaces (90%) are cylindrical in shape.

Next, we undertake a systematic study of radiosurgical beam parameters as a function of field size and beam energy. These parameters consist of beam profiles, percentage depth doses and scatter correction factors. In the measurement of percentage depth doses, an increase in the depth of dose maximum with increasing field size is observed for all x-ray beam energies studied. Monte Carlo calculations are used to divide the total dose deposited into primary and scatter dose components. Analysis of these components as a function of depth in phantom reveals that primary dose deposition, not the scattered dose, determines the depth of dose maximum at small field sizes. These aspects are covered in *Chapter 5*.

In *Chapter 6*, an analytical representation of radiosurgical percentage depth dose data is given. This representation consists of a family of bi-exponential functions fit to measured percentage depth dose data of varying beam diameter for a particular beam energy. The bi-exponential parameters are then plotted as a function of field size and fit to 2nd order polynomial. Thus, for a given beam energy, percentage depth dose data can be calculated by substituting the desired field size and depth into the four polynomials and the bi-exponential equation. Comparison of measured and calculated data shows excellent agreement at all depths, field sizes and beam energies.

The dose in the build-up region for a complete set of field sizes, ranging from small size radiosurgical beams to large size beams used in standard radiotherapy, and several beam energies is studied in *Chapter 7*. For all beam energies, the depth of dose maximum first increases with an

increasing field size at small fields, reaches a maximum depth for a 5x5 cm^2 field and then decreases with increasing field size. Monte Carlo studies show that the shift in depth of dose maximum at small field sizes is due to primary dose deposition in the phantom but that the shift at large field sizes is due to beam softening by the contamination radiation originating in the machine head. This machine head scatter was measured and then subtracted from the total dose in the build-up region. Once the scatter is removed, the shift in depth of dose maximum is eliminated. Measurements show that the head scatter component consists of electrons originating in the field flattening filter of the linear accelerator producing the x-ray beam.

The original contributions of this thesis can be summarized as follows:

- The implementation and measurement of cylindrical dose distributions in dynamic rotation radiosurgery.
- A systematic study of beam profiles, percentage depth doses and scatter correction factors of radiosurgical x-ray beams as a function of beam energy and field size.
- Measurement and analysis of an increase in the depth of dose maximum with increasing field size of radiosurgical x-ray beams.
- Simulations of radiosurgical beams with an exisiting Monte Carlo code and the division of total dose deposited into primary and scattered dose components.
- The development of an analytical representation of radiosurgical percentage depth dose data and an evaluation of the parametrized data as compared to the measured data.

- A systematic study of the depth of dose maximum as a function of field size and beam energy for a complete range of field sizes and several beam energies.
- Simulations of the build-up region dose with an exisiting Monte Carlo code for a complete range of radiotherapeutic and radiosurgical field sizes.
- Measurement and analysis of the head scatter component of large radio-therapeutic fields.
- Subtraction of the head scatter dose from the total measured dose of radiotherapeutic beams and the elimination of the observed decrease in depth of dose maximum with increasing field size at large field dimensions.

References

1. K.E. Sixel and E.B. Podgorsak, *Depth of dose maximum as a function of photon beam energy and field size*, Joint meeting of the Canadian Organization of Medical Physicists (COMP) and the Canadian Medical and Biological Engineering Society (CMBE), Ottawa, Ontario, May 12-15, 1993. (presenting author: Sixel)
2. W. Wierzbicki, K.E. Sixel and E.B. Podgorsak, *An analytical representation of radiosurgical depth dose data*, Joint meeting of the Canadian Organization of Medical Physicists (COMP) and the Canadian Medical and Biological Engineering Society (CMBE), Ottawa, Ontario, May 12-15, 1993. (presenting author: Wiersbicki)

3. C. Pla, K.E. Sixel and E.B. Podgorsak, *Cylindrical versus multiple isodose isodose distributions in stereotactic radiosurgery*, Joint meeting of the Canadian Organization of Medical Physicists (COMP) and the Canadian Medical and Biological Engineering Society (CMBE), Ottawa, Ontario, May 12-15, 1993. (presenting author: Pla)
4. K.E. Sixel and E.B. Podgorsak, *Cylindrical dose distributions in dynamic rotation radiosurgery*, Annual meeting of the Americal Association of Physicists in Medicine (AAPM), San Francisco, California, July 21-25, 1991. (presenting author: Sixel, awarded 3rd place in Young Investigator's Symposium)
5. K.E. Sixel and E.B. Podgorsak, *Build-up region of high energy photon beams in radiosurgery*, Joint meeting of the American Association of Physicists in Medicine (AAPM) and the Canadian Organization of Medical Physicists (COMP), Calgary, Alberta, August 23-27, 1992. (presenting author: Sixel)
6. C. Pla, K.E. Sixel and E.B. Podgorsak, *Calculation of cylindrical isodose distributions in stereotactic radiosurgery*, Joint meeting of the American Association of Physicists in Medicine (AAPM) and the Canadian Organization of Medical Physicists (COMP), Calgary, Alberta, August 23-27, 1992. (presenting author: Pla)
7. K.E. Sixel and E.B. Podgorsak, *Depth of dose maximum as a function of photon beam energy and field size*, (abstract) Proceedings of the 39th meeting of the Canadian Organization of Medical Physicists (COMP) and the 19th meeting of the Canadian Medical and Biological Engineering Society (CMBE), Ottawa, Ontario, May 12-15, pp. 214-215, 1993.

8. W. Wierzbicki, K.E. Sixel and E.B. Podgorsak, *An analytical representation of radiosurgical depth dose data*, (abstract) Proceedings of the 39th meeting of the Canadian Organization of Medical Physicists (COMP) and the 19th meeting of the Canadian Medical and Biological Engineering Society (CMBE), Ottawa, Ontario, May 12-15, pp. 258-259, 1993.

9. C. Pla, K.E. Sixel and E.B. Podgorsak, *Cylindrical versus multiple isodose isodose distributions in stereotactic radiosurgery*, (abstract) Proceedings of the 39th meeting of the Canadian Organization of Medical Physicists (COMP) and the 19th meeting of the Canadian Medical and Biological Engineering Society (CMBE), Ottawa, Ontario, May 12-15, pp. 260-261, 1993.

10. K.E. Sixel and E.B. Podgorsak, *Cylindrical dose distributions in dynamic rotation radiosurgery*, (abstract) Med. Phys. **18**: 621, 1991.

11. K.E. Sixel and E.B. Podgorsak, *Build-up region of high energy photon beams in radiosurgery*, (abstract) Med. Phys. **19**: 843, 1992.

12. C. Pla, K.E. Sixel and E.B. Podgorsak, *Calculation of cylindrical isodose distributions in stereotactic radiosurgery*, (abstract) Med. Phys. **19**: 843, 1992.

13. K.E. Sixel, E.B. Podgorsak and L. Souhami, *Cylindrical dose distributions in pseudodynamic rotation radiosurgery: an experimental study*, Med. Phys. **20**: 163-170, 1993.

14. B.G. Clark, E.B. Podgorsak, L. Souhami, A. Olivier, K.E. Sixel and J.-L. Caron, *A halo-ring technique for fractionated stereotactic radiotherapy*, Brit. J. Radiol. **66**: 522-527, 1993.

15. K.E. Sixel and E.B. Podgorsak, *Build-up region of high energy x-ray beams in radiosurgery*, Med. Phys. **20**: 761-764, 1993.

16. W. Wierzbicki, K.E. Sixel and E.B. Podgorsak, *An analytical representation of radiosurgical depth dose data*, Phys. Med. Biol. 38: (in press), 1993.

17. K.E. Sixel and E.B. Podgorsak, *Build-up region and depth of dose maximum of megavoltage x-ray beams as a function of field size*, Med. Phys. (in press), 1993.

TABLE OF CONTENTS

LIST OF FIGURES

LIST OF TABLES

CHAPTER 1

INTRODUCTION

1.1 Radiosurgery: A general overview

Radiosurgery is an external beam brain irradiation technique using stereotactic apparatus for accurate target localization and patient immobilization. A high dose of radiation in the form of a narrow diameter photon or heavy charged particle beam is applied, usually in a single session, to the treatment of brain disease. The initial aim of radiosurgery was to produce necrosis in the intracranial target volume with a very high dose (several thousand cGy) delivered in a single fraction without adversely affecting the surrounding brain tissue. Currently, the radiosurgical doses are somewhat lower (on the order of 2000 cGy) and the aim is to control the disease without producing necrosis. The lesions treated are usually those not amenable to conventional surgery because of their inaccessible location in the brain. By far the most common lesions treated with radiosurgery are inoperable arterio-venous malformations (AVM), although small tumours, such as pituitary adenomas and acoustic neurinomas, are also treated. Lately, attempts have been made to use radiosurgery and the more recently developed stereotactic radiotherapy (fractionated radiosurgery) in the treatment of small, well circumscribed metastatic brain lesions.

Radiosurgery is used to selectively affect small intracranial structures with diameters of several mm to several cm. Given the small size of the target volumes and the high doses involved, the requirements for successful radiosurgery are very stringent. The physical and clinical requirements for radiosurgery have been summarized as follows (1): (i) accurate determination of the target volume (within 1 mm) with stereotactic techniques; (ii) sharp dose fall-off in regions immediately

outside the target; (iii) calculation of three dimensional isodose distributions to determine the dose distribution inside and outside the target; (iv) direct superposition of isodose distributions on diagnostic images showing the anatomic location of the target and other vital structures; (v) accurate spatial (within 1 mm) and numerical (within 5%) delivery of dose to the predetermined target; (vi) accurate knowledge of the dose required for treatment of a particular disease; (vii) treatment accomplished in a reasonable amount of time; (viii) low skin dose (to avoid epilation) and low eye lens dose (to avoid cataract formation); and (ix) low or negligible scatter and leakage dose to radiosensitive organs (to avoid somatic and genetic effects of radiation).

A variety of modern radiosurgical techniques, used clinically today, meet these requirements. All techniques rely on stereotactic localization techniques to guide a number of well collimated radiation beams onto a predetermined target.

The term radiosurgery and the technique itself were introduced in 1951 by Lars Leksell (2,3) who proposed the use of orthovoltage radiation to produce local destruction of tissue in the target volume. The target was irradiated by 200-300 kVp x rays from a number of different angles to produce a focal effect at the lesion. It soon became evident that radiation in the orthovoltage range was not penetrating enough to give the required rapid dose fall-off outside the target. Therefore, radiosurgery with orthovoltage x-ray beams was discontinued in the late 1950s. The idea of focal irradiation, however, was carried over to other, more suitable radiation beams, first to protons from cyclotrons (4-6) then to focused cobalt-60 gamma rays (7) and more recently to megavoltage x rays from linear

accelerators (8-11), to heavy charged particles, such as helium, carbon and neon, from synchrocyclotrons (12,13) and even to neutrons from an isocentrically mounted cyclotron (14).

Concurrently with using proton beams for radiosurgery, Leksell was also developing a dedicated radiosurgical unit based on cobalt-60 gamma ray beams. A prototype of this unit was used clinically by 1968 and contained 179 cobalt sources, spread uniformly over a spherical segment of 60°x160° (7). Each source produced a circular beam, which was aimed toward a common point (focus) within the unit. This unit then evolved into the commercially available gamma unit (Leksell Gamma unit, Elekta Instrument AB, Stockholm, Sweden), which currently incorporates 201 cobalt-60 sources and is sometimes referred to as the *gamma knife*.

The high capital and operating costs of gamma units and cyclotrons, combined with difficulties in accurate target localization, ensured that until recently radiosurgery was available in only a few specialized centers around the world. However, the success rate of radiosurgical treatments over the past three decades has stimulated the search for less expensive and more accessible means of performing radiosurgery. In 1974 Larsson introduced the idea of using isocentric linear accelerators (linacs) as radiation sources in radiosurgery (15). Since the mid 1980s a variety of linac-based radiosurgical techniques has been introduced clinically. All linac techniques require stereotactic frames for target localization, and for patient set-up and immobilization during the treatment. Isocentric linacs in the 4 MV to 25 MV range are readily available in most major medical centers, where they are used for standard cancer radiotherapy. The modifications and additions needed to adapt modern linacs to radiosurgery

are relatively simple and inexpensive, and the number of centers offering radiosurgery as a treatment alternative is rapidly increasing.

1.2 Physical aspects of radiosurgery

1.2.1 *STEREOTACTIC FRAMES*

The stereotactic frames used in radiosurgery are usually those used for general neurological stereotaxy with minor adaptations. Typical frames are cubical or cylindrical in shape with an orthogonal or cylindrical coordinate system affixed to the structure. They are attached to the patient's head by means of several pins that penetrate the frame's structure diagonally and are held in burr-holes in the skull. The position of points within the head is then related to the coordinate system defined by the frame. With the frame rigidly attached to the patient's head, these same points can be accessed invasively in stereotactic biopsies or surgery, or noninvasively with radiation beams in stereotactic radiosurgery.

These frames, in conjunction with advances in imaging modalities, such as computed tomography (CT), magnetic resonance (MR) imaging and digital subtraction angiography (DSA), have greatly improved the accuracy of localizing intracranial targets. Localizing accuracy within ±1 mm, generally considered the achievable limit, is possible for all three stereotactic coordinates with DSA using orthogonal image pairs (16). With CT and MR imaging, the current stereotactic localization accuracy is on the order of ±1 mm for the two in-plane coordinates and ±(half the slice

thickness) for the out-of-plane coordinate (16). To use the frame with modern imaging techniques, several design considerations must be taken into account. Closed electrical loops and ferrous components that would distort the magnetic field must be avoided for MR imaging. Material that is structurally strong but of low x-ray attenuation coefficient will minimize CT artifacts. CT especially is highly suitable for stereotaxy, as it is inherently free of geometric distortions (16), eliminating the need for corrections for differential magnification as required for MR imaging.

Accurate location of the imaged section within the frame is accomplished by simultaneously imaging appropriate reference markers usually affixed to the stereotactic frame and referred to as *fiducial markers*. The markers consist of a suitable contrast material fixed in a Z- or N-shape to plates which attach to the frame. During imaging with CT or MR, at least 3 Z-shaped marker sets intersect each transverse slice. These 3 sets define the position of the transverse plane of scan in relationship to the stereotactic frame. The relative positions of the three rods of each Z-marker set define the section position at that point. This allows the third coordinate of any point of interest to be determined in addition to the other two coordinates within the 2-dimensional transverse image plane.

The fiducial marker plates are removed after the patient has been imaged. Once the diagnostic information and target position are obtained, orthogonal acrylic target localization plates are attached to the cubical frame structure in the same way as the fiducial marker plates. The information on the target position (coordinates of the target center) can now be transfered to the stereotactic frame and thus to the patient, and the target subsequently positioned with respect to the radiosurgical beam delivery

system. The frame is used to position the target center into the appropriate point on the treatment unit which is the focus of the gamma unit, point of intersection between the beam central axis and couch rotation axis on a cyclotron, or the isocenter of a linac. Once the correct treatment position is achieved, the frame is used to immobilize the patient such that the target remains in the appropriate position for the duration of the treatment.

An example of a cubical stereotactic frame is given in Fig. 1.1. Shown is a variation on the Leksell stereotactic frame (Elekta Instruments AB, Stockholm, Sweden) which was built in-house at McGill University. The base is made of aluminum, the posts of plastic and the pins of aluminum with titanium tips. The frame uses a combined fiducial marker/target localization Lucite box which attaches to the base. The cartesian coordinate system grids as well as fiducial marker lines are clearly visible on the right lateral side and the anterior side, as is a set of marks designating the location of a typical target. The localization box is used during imaging, as well as to position the target volume into the linac isocenter but is removed during the irradiation. This frame can also be used in a factionated treatment schedule. The base remains affixed to the patient for the entire factionated treatment schedule, while the localization box is attached only for patient positioning prior to each treatment fraction.

1.2.2 *RADIOSURGERY WITH HEAVY CHARGED PARTICLES*

Radiosurgery with heavy charged particles was started in the late 1950s in Uppsala by Larsson *et al* (4), in Berkeley by Lawrence *et al* (5) and

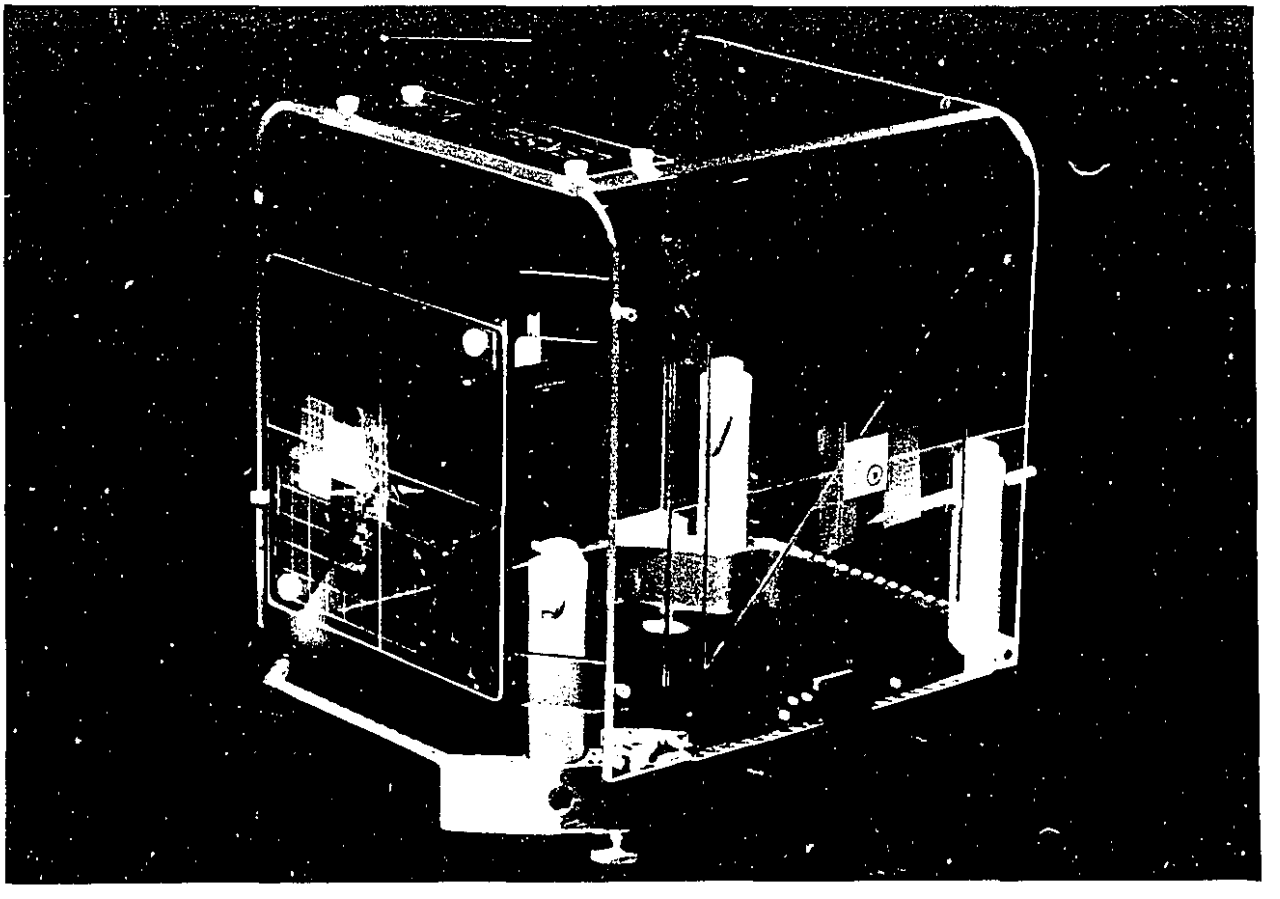

Figure 1.1 An example of a stereotactic frame. This frame is in-house-built, and is shown with the Lucite fiducial marker/target localization box attached. The location of a typical target is also shown.

later in Boston by Kjellberg *et al* (6), all using proton beams produced in cyclotrons. The principle of using heavy charged particles in radiosurgery is based on the dose deposition pattern of a beam of such particles which lose energy through Coulomb interactions with the atoms and nuclei of the attenuating medium; the brain tissue in the case of radiosurgery. At the surface, the particles have a high velocity and a correspondingly small energy loss. With an increasing depth in the medium, the rate of energy loss increases as the velocity of the particle decreases. Near the end of the particle range, when travelling quite slowly, the rate of energy loss suddenly increases and then abruptly falls to zero as the particle comes to rest. This increase in energy deposition is called the Bragg peak. The range and position of the Bragg peak are proportional to the initial energy of the charged particle and inversely proportional to its mass and charge as well as to the atomic number of the attenuating medium.

The dose in the Bragg peak, which is about 3 times greater than on the surface, allows the dose to be concentrated in the target volume, while minimizing the dose to the healthy tissue surrounding the tumour. In proton beam radiosurgery this difference is further amplified by approaching the target with several beams (about 6 to 12) from different directions.

In addition to being far too expensive for widespread, routine clinical use, there are several problems associated with Bragg peak radiosurgical techniques. Typically, the peak itself is too narrow (on the order of 5 mm) to cover most intracranial targets with a single beam. Thus the peak must be broadened in some way, either by superimposing beams of various energies at the target or by using bolus materials. In this case the differential

between the Bragg peak and surface dose is largely lost. Secondly, as the beam approaches the target from various directions the exact distance between the target center and the brain surface must be determined with stereotactic procedures in order to place the Bragg peak into the target center for each individual beam. Thus radiosurgery with heavy charged particles is complicated and labor intensive, without any proven corresponding increase in clinical benefits.

1.2.3 *RADIOSURGERY WITH THE GAMMA UNIT*

Photon beam radiosurgery is performed either with the gamma unit or with isocentric linear accelerators. The gamma unit is commercially available and has been described in detail by several of its users (17-19). First developed in the 1960s, the unit has evolved to presently incorporate 201 cobalt-60 sources, each with a nominal activity of 1 TBq (~30 Ci) and a half life of 5.26 years. Two models of the gamma unit are available: in one, the sources are distributed evenly over a 160°x60° sector of the hemispherical source core; in the other, the sources are distributed on a ring containing the transverse plane and extending 36° into the upper hemisphere. In Fig. 1.2(a) we show the points of beam entry into the patient's skull during the radiosurgical treatment for the first version (1). All beams are collimated with a primary collimator and directed towards a common focus with a relatively short source-axis distance (SAD) of ~39.5 cm.

The final collimation is achieved with a special helmet containing 201 tungsten collimators and positioned in such a way that the collimators

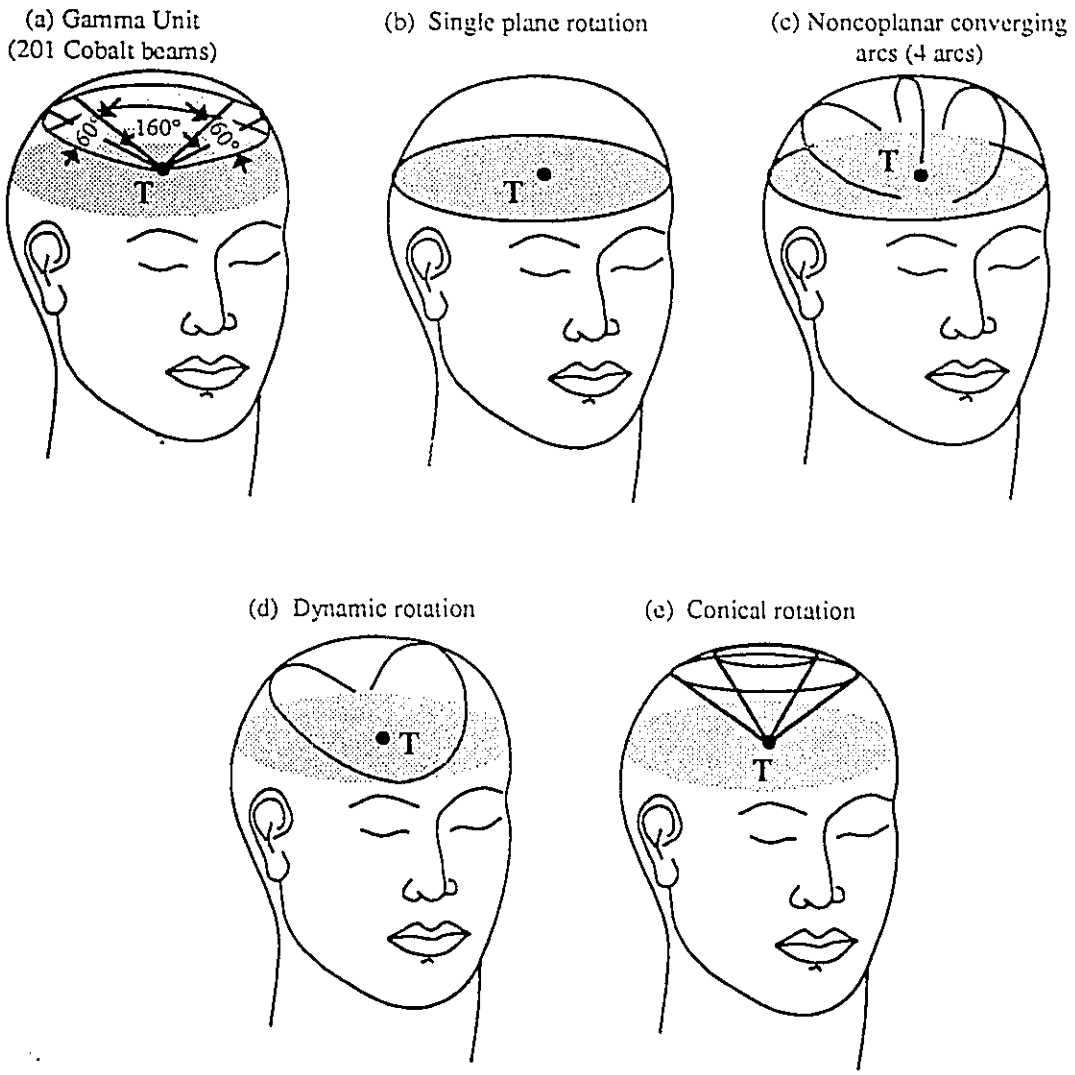

Figure 1.2 Points of beam entry into the patient's skull for various radiosurgical techniques: (a) Gamma Unit, (b) single plane rotation with a linear accelerator, (c) non-coplanar converging arcs with a linear accelerator (4 arcs), (d) dynamic rotation with a linear accelerator and (e) conical rotation with a linear accelerator.

align with the primary collimators when the proper treatment position is reached. The size of these secondary collimators, which produce field diameters from 8 mm to 18 mm at the focal point of the gamma unit, determines the target volume that is treated. The patient is positioned stereotactically with respect to the helmet so that the center of the target volume coincides with the focal spot of the unit when the shutter is opened and the patient is brought into the treatment position.

The main advantage of the gamma unit is its high spatial precision of dose delivery. This is a result of treatment achieved with stationary sources, i.e., there are no moving parts during the treatment, resulting in a maximum misalignment of each beam at the focal point within fractions of a mm (17,18). The disadvantages of the gamma unit are its high capital cost, including the cost of constructing a specially shielded room to accommodate the activity of 201 radioactive sources, the high cost of periodic replacement the cobalt-60 sources and its dedicated application to radiosurgery alone, which all preclude a widespread use and general availability. Currently, there are about two dozen gamma units in clinical operation around the world and several thousand patients have been treated successfully with the unit to date. Because of is extensive and proven record, radiosurgery with the gamma unit is often used as a standard against which other, newer techniques are measured.

1.2.4 *LINAC BASED RADIOSURGICAL TECHNIQUES*

It has been shown in the past decade that standard radiotherapy linacs may be modified relatively inexpensively for use in radiosurgery. The x-ray beam radiation fields used in radiosurgery are usually circular with diameters ranging from 1.0 cm to 4.0 cm. Additional collimators are generally added to standard collimators to achieve the small, well defined circular fields needed for treatment and to minimize the beam penumbra. Remotely controlled motorized couch or treatment chair rotation, brackets or a floor stand for mounting the stereotactic frame, interlocked readouts for angular and height positions of the couch and gantry, and a special brake to immobilize the longitudinal and lateral couch motions during the treatment are the further adaptations needed to allow the use of isocentric linacs for radiosurgery.

All linac-based radiosurgical techniques require moving parts to achieve a sharp dose fall-off outside the target volume. The dose is delivered by relying on variations in the gantry and couch positions, which raises questions as to the ability of linac-based techniques to meet the stringent requirements on mechanical stability and spatial accuracy of radiosurgery. The isocenter of the linac, which is the point of intersection between the horizontal gantry rotation axis and the vertical rotation axis of the couch or chair, should be within ±1 mm for any arbitrary gantry and couch or chair position. It has been shown (20) that this specification can be met by the manufacturers of modern linacs. Although the accuracy of dose delivery achievable with a linac is inferior to that of the gamma unit, it is of the same order of magnitude as the target localization accuracy

possible with modern imaging techniques, and can therefore be considered acceptable.

The linac-based radiosurgical techniques are divided into four main groups: *single plane rotation*, *multiple non-coplanar converging arcs*, *dynamic rotation* and *conical rotation*. Each technique is characterized by a particular set of individual rotational motions of the linac gantry or patient from given start to stop angles. When discussing these techniques, we define the angles and planes of gantry and couch rotation, as depicted in Fig. 1.3, with θ representing the angle of gantry rotation in a vertical plane and ϕ representing the angle of couch rotation in a horizontal plane (1).

Radiosurgery with a *single plane rotation* was developed by Houdek *et al* at the University of Miami (11). It is the simplest radiosurgical technique, similar to rotational techniques used in conventional radiotherapy, except that the radiation field is very small, the dose is given in a single session and a stereotactic frame is used for treatment set-up and patient immobilization during treatment. The patient is placed supine on a stationary couch fixed at $\phi=0°$, and the gantry rotated in a single plane from $\theta=0°$ to $\theta=360°$. The dose fall-off outside the target in the direction perpendicular to the plane of rotation is very steep, essentially identical to that of a stationary beam. In the plane of rotation (transverse plane), however, the dose fall-off is relatively shallow as a result of the dose superposition outside the target volume for an infinitely large number of parallel-opposed beams. As shown in Fig. 1.2(b), the beam entry trace for a full single plane rotation is in a transverse plane and coincides with the beam exit trace.

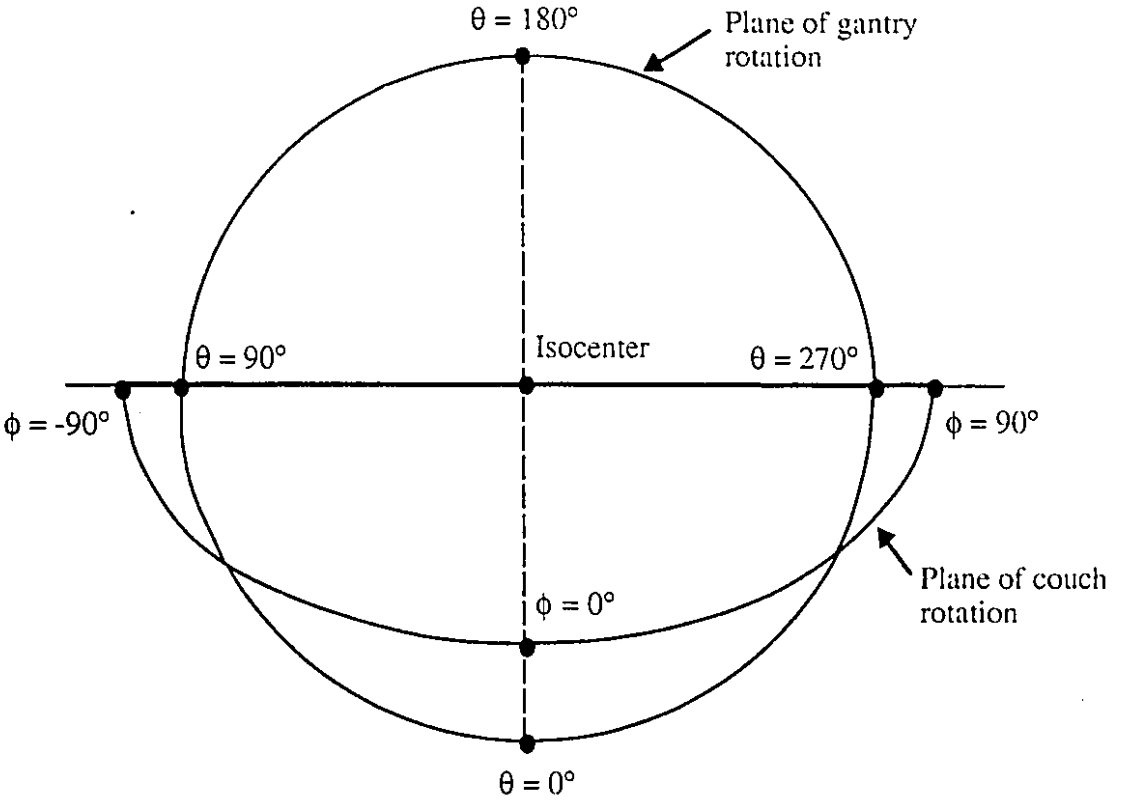

Figure 1.3 Planes of motion of the gantry and treatment couch or chair in linear accelerator-based radiosurgery. The angular convention used for the gantry rotation angle θ and the couch rotation angle ϕ is also shown.

To improve the dose fall-off obtained with the single plane rotation, Betti and Derechinsky (8), Colombo *et al* (9,21) and Hartmann *et al* (10) have developed the *multiple non-coplanar converging arcs* technique on isocentric linear accelerators. The center of the target is placed stereotactically into the isocenter of the linac, and a series of arcs, each with a different stationary treatment chair (8) or treatment couch (9,10) position, is used to spread the dose outside the target area over as large a volume as possible. To avoid parallel-opposed beams, the arcs are usually kept smaller than 180° and all beam entry points lie in the upper hemisphere, while all beam exit points lie in the lower hemisphere.

Hartmann's group in Heidelberg (10) performs radiosurgery on a 15 MV linac. Additional circular collimators define fields at the isocenter ranging from 9 mm to 29 mm. Beam diameters are defined at the 50% isodose line, and consequently collimators for treatments are selected based on the ability of this isodose surface to cover the target volume. Dose gradients are defined in terms of a fall-off from the 50% line. Irradiations in different non-coplanar planes with respect to a target point are achieved by rotating the patient in a horizontal plane on the treatment couch. Up to eleven 140° arcs of radiation are given while moving the couch by discrete angles. The gantry rotates from 20° to 160° or from 200° to 340° while the couch is positioned at up to eleven intervals from 90° to -90°.

Recently, Lutz *et al* (22,23) at the Joint Center for Radiotherapy in Boston have shown that reasonable dose fall-offs can be obtained with as few as four non-coplanar arcs. One 260° arc is given in the transverse plane with the couch fixed at 0°. Three 100° arcs, two from 40° to 140° with the couch first at 90° and then 45°, and one from 220° to 320° with the couch

at -45°, are spread over the rest of the head. The additional collimators form fields from 12.5 mm to 30.0 mm diameter defined at the 90% isodose line. The beam entry trace on the patient's skull for this treatment method is chosen as a typical example of the converging arcs technique and is depicted in Fig. 1.2(c).

Dynamic rotation radiosurgery, which was developed by Podgorsak *et al* (24,25) at McGill University in Montreal, incorporates simultaneous couch and gantry rotations to achieve a steep dose fall-off outside the target volume. The gantry rotates through 300° from θ=30° to θ=330°, while simultaneously the couch rotates through 150° from ϕ=75° to ϕ=-75° at half the gantry's speed. Thus, for each two degrees of gantry rotation, the couch rotates by one degree. The beam entry trace always lies in the upper hemisphere of the head, implying that all beam exit points lie in the lower hemisphere. Thus, although all beams intersect in the target volume and the gantry travels through almost a full circle, the coincidence between an entrance beam and an exit beam, which would degrade the sharpness of the dose fall-off outside the target volume, is avoided for all beams. The resulting beam trace on the patient skull resembles a baseball seam and is shown in Fig. 1.2(d). Though the technique appears technically complex, it is relatively simple and efficient to use once the continuous couch rotation capability has been installed. In the dynamic rotation used at our center the 90% isodose curve is chosen to coincide with the target volume. Beam diameters range from 5 mm to 40 mm in steps of 2.5 mm.

Recently, McGinley *et al* (26) developed a *conical rotation* technique in which the patient rotates on a special treatment chair from ϕ=0° to ϕ=360° while the gantry is stationary at a given angle θ between 90° and 180°. The

stereotactic frame is attached to a pedestal, which in turn is mounted to the base plate of the patient support assembly. Up to three stationary gantry positions (θ=100°, 120° and 145°) are used for a typical treatment, resulting in coaxial circles for beam entry traces in the upper hemisphere and a conical irradiation pattern, as illustrated for two gantry positions in Fig. 1.2(e).

1.2.5 *COMPUTERIZED TREATMENT PLANNING FOR RADIOSURGERY*

A treatment planning system, which calculates and displays a three-dimensional isodose distribution based on the patient's anatomy within the stereotactic frame, is another important component of a radiosurgical service. For all techniques described above, the treatment goal, which is maximizing the target dose while minimizing the dose to surrounding tissue is achieved by aiming the radiation beam toward the target from a large number of non-coplanar directions. The calculation of radiosurgical dose distributions is therefore a 3-dimensional problem. Stereotactic 3-dimensional patient data obtained from CT, MR or DSA images is the basis for any radiosurgical treatment planning system. This data allows one to calculate the target location, as well as the depth in tissue for each point-of-interest on the dose matrix, thus enabling an accurate calculation of the dose matrix for each individual radiation beam.

Once the dose matrix is calculated, the resulting distribution is normalized such that the dose at the isocenter has a value of 100%. A fixed,

high percentage isodose surface (typically 90%) which is spherical when radiation beams are circular is then chosen to coincide with the edge of the target volume. The dimensions of this volume determine the appropriate field size needed to treat a particular lesion. An essential requirement of such a treatment planning system is that the calculated isodose contours can be directly superimposed onto the CT, MR or DSA images of the patient. This enables the physician to visualize the dose distribution not only in the target volume, but also in the surrounding sensitive structures within the brain.

In the past, centers offering a radiosurgical service had to develop their own treatment planning systems and only more recently 3-dimensional planning systems have become commercially available. Unfortunately, many of these systems still do not display dose distributions directly on localization images. Furthermore, they are not very user-friendly and are relatively expensive to purchase. In general, centers focussing on radiosurgical research and development continue to use their in-house developed software for radiosurgical dose distribution calculation.

The dose fall-off outside the target volume is measured in terms of the distances in which the dose falls from the target edge to lower isodose surfaces, such as 50%, 20% and 10%. The shorter is this distance, the steeper is the dose fall-off outside the target and the more suitable is the technique for radiosurgical procedures. When evaluating a technique for clinical use, the sharpness of the dose fall-off as well as the isotropy of the dose distribution must be taken into account, the aim being to have dose fall-offs sharp and ideally of equal sharpness in all directions. For typical radiosurgical techniques, only the high level isodose surfaces (e.g., 50%

and above) are isotropic, the lower level isodose surfaces become progressively more anisotropic, reflecting particularities of a given treatment technique, resulting from technical constraints imposed in beam angulation. The isodose distributions may then be characterized by two dose fall-offs: the best (sharpest) and worst (shallowest), with all other fall-offs between the two extremes. The larger the difference between the two dose fall-offs, the worse is the anisotropy of the isodose distribution, and the less applicable is the technique for clinical radiosurgery.

Dose-volume histograms (DVH) can also be used to characterize a given treatment technique (27-30). Providing a quantitative comparison of a 3-dimensional dose distribution, DVHs are calculated by dividing the brain volume into voxels, with the thickness depending on the image slice thickness (usually from 1 mm to 5 mm) and the area depending on the resolution of the dose calculation matrix. The dose value in each of the voxels is classified into a percentage dose increment which can range from 100% (the maximum dose) to zero in predefined steps. Thus a frequency distribution of dose values within the brain is obtained. When plotted in integral form as a function of dose, this data gives the volume of tissue encompassed by a certain isodose surface. Clearly, the smaller this volume, the less healthy tissue is irradiated and the better suited for radiosurgery a given technique may be. Comparison of dose volume histograms for different radiosurgical treatment techniques used to date clinically have shown that differences in the size of the irradiated volumes occur only at isodose levels below 20%.

Dose volume histograms are useful, not only as a means of comparing different treatment techniques, but also to evaluate a particular

plan for a given patient in order to obtain an optimum plan. DVHs can be used to determine the dose received by a vital structure with a lower radiation tolerance, such as the brain stem. Furthermore, it has been advocated that DVH be used to develop a database of normal tissue tolerance levels (31) and as a quantitative means of estimating complication rates associated with radiosurgery (32).

In the past, all targets were assumed to be spherical in shape, and any difference between the spherical target-defining isodose surface and the actual target shape was ignored. However, more recently, work has been done to conform high level isodose surfaces to the target shape, as will be discussed elsewhere in this thesis. In this situation, dose volume histograms can then be used to compare the treatment volume irradiated in a given technique with the true target volume (33,34). The amount of healthy tissue encompassed by the prescription isodose surface *vs* the amount of target volume encompassed by the same isodose surface can be used to judge a given technique.

1.3 Clinical aspects of radiosurgery

1.3.1 *CLINICAL CONSIDERATIONS FOR RADIOSURGERY*

Radiosurgery is usually performed on an outpatient basis. At McGill, a typical patient has the stereotactic frame placed onto the skull under local anesthesia, followed by imaging procedures and treatment planning. The patient is then positioned on the linac, the target center is

placed to coincide with the machine isocenter and the radiation dose is delivered with the dynamic rotation technique. The frame is then removed and the patient is usually discharged on the same day. Typically, the entire procedure takes 3-4 hours.

For the radiosurgical techniques described in the previous section, the resulting high dose volumes are essentially spherical, while many intracranial lesions are of an irregular shape. Because of their small dimensions within the brain, these lesions are usually approximated by spheres, as treating even the most elongated shape with a spherical volume includes only a relatively small volume of healthy tissue. However, recent interest in radiosurgery has been to devise a means of shaping isodose contours to conform to the shape of the actual target volume. One such method is the use of multiple isocenters. This technique is particularly popular with users of the gamma unit (35), for which the variety of field sizes is limited to four, as is the maximum attainable field size (18 mm diameter). Thus more than one isocenter is needed to properly cover larger or elongated targets. The main disadvantages of this technique are the extensive treatment planning required, the increased treatment time and the large dose inhomogeneities produced in the target volume.

Other techniques to shape isodose surfaces are still in the developmental stages and have not yet been applied clinically. They will be discussed in more detail later in this thesis, where we also present our technique for treatment of cylindrical rather than spherical targets. Due to the lack of clinical experience, it is not yet clear whether the increase in effort and time for treatment planning and dose delivery needed to shape isodose surfaces will be offset by a reduction in complication rates.

Radiosurgery is frequently used to treat histologically benign lesions, thus scattered and leakage doses of radiation to sensitive organs must be kept low to avoid potential somatic and genetic effects. In both the gamma unit (36) and linac-based techniques (25) the surface doses are usually less than 1% of the target dose and the scattered radiation to the thyroid, breast and gonads amounts to only 0.2%, 0.06% and 0.02% of the target dose, respectively. At these doses, the risk of radiation carcinogenesis is small, and offset by the risk of morbidity from the lesion to be treated (37).

Based on radiobiological considerations it is well known that normal tissue tolerates fractionated irradiation better than it tolerates irradiations delivered in a single session (38). This potential increase in the therapeutic ratio has led some centers to apply the techniques of radiosurgery to the delivery of radiation in multiple fractions (39-42). The interest in fractionated treatment schedules using radiosurgery techniques is rapidly growing, as are the reports on patients treated with this approach. With an increased patient data base the clinical advantages of multiple fractions will be easier to assess.

The technical considerations of fractionated stereotactic radiosurgery are more complex than those of single session treatments, as all irradiations must be delivered with stereotactic techniques. Fractionated schemes differ from center to center. At McGill University the patient is treated with six fractions typically of 7 Gy each delivered every second day (43). Between 1987 and 1991 the first treatment was given using a stereotactic frame for target localization, treatment planning and patient immobilization during the treatment. Before the frame was removed after the first treatment, the target center was marked on the patient's skin with

tattoos, the frame was then removed and the subsequent five treatments used a standard neurosurgical halo-ring for patient immobilization, while the tattoo marks in conjunction with wall and ceiling laser-positioning devices ensured proper placement of the target center into the linac isocenter. The halo ring was left in place on the skull for the duration of the course of treatment. Stringent quality assurance procedures were required to maintain spatial accuracy under these conditions and should be considered by a center contemplating this treatment modality.

In 1992, a more precise irradiation technique was developed at McGill University, based on the in-house-built stereotactic frame which was shown previously in Fig. 1.1 (44). In preparation for the first treatment, the stereotactic frame is attached to the patient's skull and the coordinates of the target center are determined and marked onto the Lucite target localization box. With the help of the laser positioning devices, the patient is placed into the treatment position on the linac. The Lucite target localization box is then removed, the target information is tattooed on the patient's skin and the patient is given the first treatment. The tattoo marks in conjunction with the target information on the Lucite target localization box are used for patient set-up on the linac for the subsequent five treatments. The experience with this new technique for fractionated treatment schedules has shown that the in-house-built frame is easily left attached to the patient's skull for the 12 day duration of the fractionated regimen and that positioning with the Lucite target localization box verified with tattoo marks ensures a high level of precision for individual fractionated treatments.

1.3.2 *CLINICAL APPLICATIONS OF RADIOSURGERY*

The lesions treated with radiosurgery can be placed into one of four categories: *functional disorders*, *vascular lesions*, *benign tumours* and *malignant tumours*. Radiosurgery was originally developed to treat functional disorders using doses as high as 250 Gy for intractable pain (trigeminal neuralgia), Parkinson's disease, epilepsy and psychoneurosis (38). However, the results of these treatments were inconclusive, and the number of patients treated was quite small. With the advent of other treatment modalities for many of these disorders, this application of radiosurgery has been largely discontinued.

Arteriovenous malformations (AVMs) are congenital intracranial lesions characterized by a tangle of pathologic vessels, dilated afferent and efferent vessels and a rapid circulation time. Although AVMs are histologically benign, they can be the cause of life-threatening hemorrhage, with the overall lifetime risk of death estimated to be 29%, and of severe long-term morbidity found in 23% of survivors (45). Clearly, the established presence of an AVM is cause to offer treatment at the time of diagnosis as a preventive measure.

Although surgery remains the treatment of choice for peripheral lesions, radiosurgery has become a treatment option for AVMs located in inaccessible regions of the brain. The pioneering work in this field is attributed to the Karolinska Hospital in Sweden (46). Over 600 patients with AVM have been treated with the gamma unit. The excellent results have stimulated the subsequent development of linac-based radiosurgical techniques. Following irradiation, regardless of treatment technique, a

complete angiographic obliteration of the AVM is expected to occur within one year for 35-40% of the patients and within two years for 70-80% (38). Three factors seem to play a role in the success rate of radiosurgery for AVM: nidus coverage, prescribed dose and size of the lesion. A partial coverage of the AVM nidus by a dose of less than 20-25 Gy will result in an incomplete obliteration. Protection against hemorrhage is only provided when the AVM is completely obliterated, thus a detailed assessment of the vascular lesion is imperative prior to radiosurgery to ensure that the nidus is accurately defined and will be properly covered with an adequate radiation dose.

Other vascular disorders treated with radiosurgery have a less conclusive success rate. A small number of patients with angiographically occult vascular malformations (cavernous angiomas) have been treated (37), but clinical results have not been optimal. At McGill University, 10 patients have been treated with radiosurgery for this disorder, but only in two patients was a radiological reduction in the size of the lesion observed, although a symptomatic improvement was seen in six (38). Further clinical experience and a greater understanding of the natural history of these lesions is needed to properly establish the value of radiosurgery in their management.

Acoustic neurinoma is a relatively rare, histologically benign tumour. Because of its location within the brain, it can be the cause of considerable morbidity including hearing loss, balance loss, trigeminal or facial nerve palsies and hydrocephalus. Though surgery remains the standard form of treatment, it is not without risk, with the vast majority of patients developing complete hearing loss in the operated ear and/or

permanent facial weakness (38). Radiosurgery, with its lower morbidity has thus become an attractive alternative to microsurgery in selected patients.

A substantial number of patients with acoustic neurinomas have been treated with the Stockholm and Pittsburgh gamma units (37). Experience has shown that a dose of about 20 Gy will cause a reduction in tumour volume in over 50% of the patients, with stable disease in 40% to 50%. After 2 years, preserved hearing was observed in about 50% of the cases, and complete deafness in only about 20%. Less than 30% of the patients developed new facial neuropathies, with full recovery experienced within a year of treatment. Given the importance of hearing preservation, radiosurgery is clearly emerging as a valid therapeutic option for selected acoustic neurinomas.

Meningiomas are histologically benign tumours for which surgery has been the mainstay of treatment. However, radiosurgery has also been used as a treatment modality for small unresectable or recurrent lesions. Clinical experience in Pittsburgh and Heidelberg has shown a tumour control rate above 90% (37). Treatment failure occured for large tumours that were not completely contained within the targeted volume. To date the results of radiosurgical treatments in selected patients with intracranial meningiomas are encouraging, yet optimal doses and treatment schedules must still be established.

Radiosurgery with proton beams in the treatment of tumours in the pituitary region, such as acromegaly, Cushing's disease, Nelson's syndrome and prolactinomas, has resulted in a substantial success rate. Over 800 patients have received stereotactic helium-ion pituitary

radiosurgery at the Lawrence Berkeley Laboratory in California (6). Most patients experienced a marked clinical and biochemical improvement within the first year, while complications have been infrequent. The experience with photon radiosurgery in these tumours is more limited, yet here too the success rate reported to date has been a clinical remission in more than 75% of the patients treated (47). Again, further studies are needed to define optimal treatment doses, but the evidence that photon beam radiosurgery is a viable treatment form is very encouraging.

Other benign conditions, for example craniopharyngioma, chordomà, choriod plexus papilloma and hemangioblastoma, have been treated with radiosurgery in various centers (38). However, the number of cases falling into these categories has been too small to report clinical results, and more data is needed to determine precisely the role that radiosurgery would play in the management of these diseases.

Stereotactic radiosurgery is also beginning to take on a greater role in the palliative care of inoperable, recurrent solitary brain metastases (37). These tumours affect 20% to 30% of patients with systemic cancer, with the traditional treatment being surgery if possible, followed by whole brain irradiation. Radiosurgery is emerging as an alternative primary treatment modality, especially for solitary cerebral metastatic tumours as well as for those patients who have failed previous whole brain irradiation. Clinical neurological response occurs rapidly, one or two days after treatment, with few complications reported.

Finally, several centers have reported treating a small number of patients with low and high grade astrocytomas with radiosurgery (37), either in a single session treatment or in multiple fractions. At McGill,

clinical improvements were seen in all 9 patients treated to date 2 to 3 months following irradiation, while biological response has been much slower, with a tumour reduction in only 4 of the patients (38).

From the brief clinical overview presented above, it is clear that radiosurgery plays an important role in the treatment of brain disease. It is a well established modality in the management of AVM, with a proven success rate of more than 70%, regardless of type of radiation or irradiation technique used. In other clinical situations, the results are less conclusive. However, radiosurgery is becoming a major treatment option for tumours, such as acoustic neurinomas, meningiomas, pituitary adenomas and solitary metastatic brain disease. As further clinical experience is gained, the parameters used in treatment planning, such as treatment dose, target volume definition and treatment schedule, will be defined better, hopefully resulting in an even greater success rate.

1.3.3 *COMPLICATIONS: ACUTE AND LATE EFFECTS OF RADIOSURGERY*

Acute side effects of radiosurgery are uncommon. The frame placement causes some degree of discomfort, and for patients undergoing fractionated treatments, skin infection can be observed around the screw insertion site (38). It has been reported that in the 24 hours following proton radiosurgery, headache, fever and increased risk of seizure has occured in a few patients (48). The greatest risk seems to be to patients treated for acoustic neurinomas. The experience with the gamma unit at

the Karolinska Hospital in Sweden shows that trigeminal neuropathy and facial neuropathy developed in 18% and 15%, respectively, of patients treated for this disorder (49). The incidence of such complications was higher in Pittsburgh, where a gamma unit is also used for radiosurgical treatments. Here, trigeminal neuropathy and facial neuropathy occured in 37% and 33% of the patients, respectively (50). For both centers, the observed complications were transient and began to improve from one to 17 months after onset.

Late side effects of radiosurgery are characterized by radiation necrosis and/or oedema occur in 2% to 6% of the patients (38). However, detailed prospective analyses with serial imaging studies have yet to be performed and so the real incidence of radiological changes resulting from radiosurgery has not yet been established.

At McGill University, the results of the first 112 patients treated with dynamic radiosurgery have recently been reviewed (38). Of the treated lesions, 59 were AVMs, 13 brain metastases, 11 gliomas, 11 cavernous angiomas and 22 a variety of other malignant or benign diseases. Acute and late complications resulting from the radiosurgical treatments developed in 6.3% of the patients (7 of 112 patients). Of these, 2 patients experienced acute effects, one transient nausea and homonymous hemianopsia following treatment for an AVM, and the other transient facial neuropathy following treatment for an acoustic neurinoma. Late complications occured in 5 patients who developed radiation necrosis between 5 to 21 months following irradiation.

The small number of patients who developed complications preclude the establishment of a relationship between complications and prescribed

dose, fractionation, collimator diameter, previous irradiation or the anatomical region of the lesion that was treated. Further clinical experience will be required to establish the real tolerance of various brain structures to radiosurgery and to define the optimal dose prescription related to volume, previous irradiation, number of isocenters, fractionation, and lesion type and location.

1.4 Thesis outline

We now present a brief outline of the specific aspects of radiosurgical x-ray beams which are discussed in this thesis. In *Chapter 2*, an overview of the experimental techniques and apparatus used for beam measurements is given. The equipment which generates the investigated radiation beams is described. This includes two linear accelerators as well as a superficial x-ray unit. The linear accelerator adaptations necessary to produce radiosurgical beams and to perform a radiosurgical treatment are discussed. Next we present the measuring devices and radiation detectors, and finally, the phantom materials used in conjunction with these detectors.

In *Chapter 3*, we also deal with experimental apparatus and techniques, but now we focus on Monte Carlo calculations. The general principles of Monte Carlo techniques are presented and then the specific code used in Monte Carlo simulations throughout this thesis is described in terms of its capabilities and features. We show the program structure and user access to the specific subroutines, without giving extensive detail

regarding the actual transport mechanism. Variance reduction techniques, which increase the speed of the simulations, are important features of a Monte Carlo code. Thus we devote a section of *Chapter 3* to the variance reduction techniques used in our calculations. Finally, we mention the hardware and compiler that we used to perform the Monte Carlo simulations.

Recent interest in radiosurgery has focussed on shaping isodose contours, as it has been observed that many volumes to be treated are not spherical but ellipsoidal or even more complex in shape. In *Chapter 4*, we propose a means for obtaining cylindrical dose distributions in a single treatment. The method is based on rectangular fields and an additional rotation of the treatment collimator to follow a projected target in the coordinate frame of the treatment couch. By rotating the collimator and by adjusting its longitudinal opening to the projected length of the target volume, a cylindrical dose distribution results. We derive this method and present measured dose distributions of sample targets irradiated in phantom. The advantages of using cylindrical dynamic rotation *vs* spherical dynamic rotation for suitably shaped targets are then discussed.

Next, radiosurgical x-ray beam data is presented from a physical (rather than the clinical) point-of-view. In *Chapter 5* we present beam data necessary for treatment planning in radiosurgery: the percentage depth dose (PDD) curves, the beam profiles at various depths and the scatter correction factors. This data is measured and presented for three beam energies and the available range of radiosurgical field sizes. After the general discussion of radiosurgical beam parameters, a particular effect observed during the measurement of depth doses in the build-up region, a

shift in depth of dose maximum, d_{max}, with field diameter is examined in some detail as a function of field size and beam energy. Monte Carlo simulations are used to understand and account for the observed change in d_{max}.

An analytical representation based on a curve fitting process was developed to parametrize x-ray beam percentage depth doses as a function of depth in phantom, field diameter and beam energy. First, bi-exponential functions are fit to a family of measured depth dose data of varying field diameters and a constant beam energy. The fitting parameters are then plotted as a function of field size and fit to a polynomial. This results in a highly compact mathematical form of PDD data representation which can be implemented on any computer requiring fast and accurate PDD calculation. The parametrization technique and its evaluation are given in *Chapter 6*.

In *Chapter 7* we generalize the findings of *Chapter 5* where d_{max} of radiosurgical beams is discussed. We study the energy and field size dependence of the depth of dose maximum and present data for a wide range of field sizes from small size fields (1×1 cm^2) used in radiosurgery to the very large field sizes available from linacs (30×30 cm^2) and used in standard radiotherapy. For a given beam energy, at small fields d_{max} increases rapidly with increasing field size, peaks near 5×5cm^2 and decreases with increasing field size for large fields. The cause of the shift is examined with Monte Carlo simulations as well as though experimental investigation, by studying the relative amount, the nature and the origin of the head scatter component of the x-ray beams.

Finally, we close with a thesis summary and some suggestions for future work, presented in *Chapter 8*.

1.5 Summary

In this chapter, we define the term radiosurgery and give a brief history of this radiation treatment modality. Originally performed using orthovoltage x rays, the radiation sources for radiosurgery have since evolved to higher energy photon beams generated by linear accelerators or cobalt-60 sources and to heavy charged particle beams. All radiosurgical techniques require stereotactic frames for target localization, patient set-up and immobilization during the treatment. Physical aspects of radiosurgery, such as the stereotactic frames, treatment techniques with heavy charged particles, the gamma unit and linacs, and computerized treatment planning are described. An overview of clinical considerations and applications is also given, including a discussion of possible clinical complications resulting from a radiosurgical treatment. Finally, we outline the specific aspects of radiosurgery that are addressed in this thesis.

1.6 References

1. E.B. Podgorsak, *Physics for radiosurgery with linear accelerators*, Neurosurg. Clin. North Amer. **3**: 9-34, 1992.
2. L. Leksell, *The stereotaxis method and radiosurgery of the brain*, Acta Chir. Scan. **102**: 316-319, 1951.
3. L. Leksell, *Gezielte Hirnoperationen*, in: Handbuch der Neurochirurgie, H. Olivecrona and W. Tonnis (eds), Springer Verlag, New York, 1957, pp. 178-218.
4. B. Larsson, L. Leksell, B. Rexed, P. Sourander, W. Mair and B. Anderson, *The high energy proton beam as a neurosurgical tool*, Nature **182**: 1222-1223, 1958.
5. J.H. Lawrence, C.A. Tobias, J.L. Born, C. Wang and J.A. Linfoot, *Heavy-particle irradiation in neoplastic and neurologic disease*, J. Neurosurg. **19**: 717-722, 1962.
6. R.N. Kjellberg, A. Sintani, A.G. Frantz and B. Kliman, *Proton beam therapy in acromegaly*, N. Engl. J. Med. **278**: 689-695, 1968.
7. L. Leksell, *Cerebral radiosurgery I Gamma thalamotomy in two cases of intractable pain*, Acta Chir. Scan. **134**: 385-395, 1968.
8. O.O. Betti and V.E. Derchinsky, *Hyperselective encephalic irradiation with linear accelerator*, Acta Neurochir. **33**: 385-390, 1984.
9. F. Colombo, A. Benedetti, F. Pozza, R.C. Avanzo, C. Marchetti, C. Chierego and A. Zanardo, *External stereotactic irradiation by linear accelerator*, Neurosurg. **16**:154-160, 1985.
10. G.H. Hartmann, W. Schlegel, V. Sturm, B. Kober, O. Pastyr and W.J. Lorenz, *Cerebral radiation surgery using moving field*

irradiation at a linear accelerator facility, Int. J. Radiat. Oncol. Biol. Phys. **11**: 1185-1192, 1985.

11. P.V. Houdek, J.V. Fayos, J.M. Van Buren and M.S. Ginsberg, *Stereotaxic radiotherapy technique for small intracranial lesions*, Med. Phys. **12**: 469-472, 1985.
12. J.T. Lyman and J. Howard, *Dosimetry and instrumentation for helium and heavy ions*, Int. J. Radiat. Oncol. Biol. Phys. **3**: 81-85, 1977.
13. J.T. Lyman, L. Kanstein, F. Yeater, J.I. Fabrikant and K.A. Frankel, *A helium-ion beam for stereotactic radiosurgery of central nervous system disorders*, Med Phys. **13**: 695-699, 1986.
14. B.R. Griffin, S.H. Warcola, M.R. Mayberg, J. Eenmaa, J. Eskridge and H.R. Winn, *Stereotactic neutron radiosurgery for arteriovenous malformations of the brain,*. Med. Dosimetry **13**: 179-182, 1988.
15. B. Larsson, K. Liden and B. Sarby, *Irradiation of small structures through intact skull*, Acta Radiol. TPB **13**:513-534, 1974.
16. T.M. Peters, J.A. Clark, A. Olivier, A.P. Marchand, G. Mawko, M. Dieumegarde, L.V. Muresan and R. Ethier, *Integrated stereotaxic imaging with CT, MR imaging and Digital Subtraction Angiography*, Radiology **161**:821-826, 1986.
17. H. Dahlin and B. Sarby, *Destruction of small intracranial tumours with ^{60}Co gamma irradiation*, Acta Radiol. TPB **14**: 209-227, 1975.
18. L. Walton, C.K. Bomford and D. Ramsden, *The Sheffield stereotactic radiosurgery unit: physical characteristics and principles of operation*, Brit. J. Radiol. **60**: 897-906, 1987.

19. A. Wu, G. Lindner, A.H. Maitz, A.M. Kalend, L.D. Lundsford, J.C. Flickinger and W.D. Bloomer, *Physics of gamma knife approach on convergent beams in stereotactic radiosurgery*, Int. J. Radiat. Oncol. Biol. Phys. **18**: 941-950, 1990.

20. K.E. Sixel, *Physical parameters of narrow photon beams in radiosurgery*, M.Sc. thesis, McGill University, 1990.

21. G. Chierego, C. Marchetti, R.C. Avanzo, F. Pozza and F. Colombo, *Dosimetric considerations on multiple arc stereotaxic radiotherapy*, Radiotherapy and Oncology **12**: 141-152, 1988.

22. W. Lutz, K.R. Winston and N. Maleki, *A system for stereotactic radiosurgery with a linear accelerator*, Int. J. Radiat. Oncol. Biol. Phys. **14**: 373-381, 1988.

23. K.R. Winston and W. Lutz, *Linear accelerator as a neurosurgical tool for stereotactic radiosurgery*, Neurosurg. **22**: 454-464, 1988.

24. E.B. Podgorsak, A. Olivier, M. Pla, J. Hazel, A. de Lotbinière and B. Pike, *Physical aspects of dynamic stereotactic radiosurgery*, Appl. Neurophysiol. **50**: 63-68, 1987.

25. E.B. Podgorsak, A. Olivier, M. Pla, P.Y. Lefebvre and J. Hazel, *Dynamic stereotactic radiosurgery*, Int. J. Radiat. Oncol. Biol. Phys. **14**: 115-125, 1988.

26. P.H. McGinley, E.K. Butker, I.R. Crodker and J.C. Landry, *A patient rotator for stereotactic radiosurgery*, Phys. Med. Biol. **35**:649-657, 1990.

27. M.H. Phillips, K.A. Frankel, J.T. Lyman, J.I. Fabrikant and R.P Levy, *Comparison of different radiation types and irradiation*

geometries in stereotactic radiosurgery, Int. J. Radiat. Oncol. Biol. Phys. **18**: 211-220, 1990.

28. J.D. Graham, A.E. Nahum and M. Brada, *A comparison of techniques for stereotactic radiotherapy by linear accelerator based on 3-dimensional dose distributions*, Radio. Oncol. **22**: 29-53, 1991.

29. M.C. Schell, V. Smith, D.A. Larson, A. Wu and J.C. Flickinger, *Evaluation of radiosurgery techniques with cumulative dose volume histograms in linac-based stereotactic external beam irradiation*, Int. J. Radiat. Oncol. Biol. Phys. **20**: 1325-1330, 1991.

30. C.F. Serago, P.V. Houdek, B. Bauer-Kirpes, A.A. Lewin, A.A. Abitbol, S. Gonzales-Arias, V.A. Marcial-Vega and J.G. Schwade, *Stereotactic radiosurgery: Dose-volume analysis of linear accelerator techniques*, Med. Phys. **19**: 181-185, 1992.

31. G.T.Y. Chen, *Dose volume histograms in treatment planning*, Int. J. Radiat. Oncol. Biol. Phys. **14**:1319-1320, 1988.

32. J.C. Flickinger, *An integrated logistic formula for prediction of complications from radiosurgery*, Int. J. Radiat. Oncol. Biol. Phys. **17**: 879-885, 1989.

33. C. Pla, K.E. Sixel and E.B. Podgorsak, *Calculation of cylindrical isodose distributions in stereotactic radiosurgery*, (abstract) Med. Phys. **19**: 843, 1992.

34. C. Pla, K.E. Sixel and E.B. Podgorsak, *Cylindrical versus multiple isodose isodose distributions in stereotactic radiosurgery*, (abstract) Proceedings of the 39th meeting of the Canadian Organization of Medical Physicists (COMP) and the 19th meeting of the Canadian

Medical and Biological Engineering Society (CMBE), Ottawa, Ontario, May 12-15, pp. 260-261, 1993.

35. J.C. Flickinger, A. Maitz, A. Kalend, L.D. Lunsford and A. Wu, *Treatment volume shaping with selective beam blocking using the Leksell gamma unit*, Int. J. Radiat. Oncol. Biol. Phys. **19**: 783-789, 1990.

36. L. Steiner, *Treatment of arteriovenous malformations by radiosurgery*, in: Intracranial Arteriovenous Malformations, C.B. Wilson and B.M. Stein (eds), Williams and Wilkins, Baltimore, 1984, pp. 295-313.

37. M.R. McKenzie, L. Souhami, E.B. Podgorsak, A. Olivier, J.-L. Caron and J.-G. Villemure, *Photon radiosurgery: a clinical review*, Can. J. Neurol. Sci. **19**: 212-221, 1992.

38. L. Souhami and E.B. Podgorsak, *Radiosurgery: a review of clinical aspects*, in: Advances in Radiology and Oncology, T. Benulic, G. Sersa and V. Kovac (eds.) Radiologia Iugoslavica, Ljubljana, Slovenia, 1992, pp. 151-166.

39. M. Austin-Seymour, J. Munzenrider, R. Linggood, M. Goitein, L. Verhey, M. Urie, R. Gentry, S. Birnbaum, D. Ruotolo, C. Crowell, P. McManus and H.D. Suit, *Fractionated proton radiation therapy of cranial and intracranial tumours*, Am. J. Clin. Oncol. **13**: 327-330, 1990.

40. F. Pozza, F. Colombo, G. Chierego, R.C. Avanzo, C. Marchetti, A. Benedetti, L. Casentini and V.J. Pisciotta, *Low grade astrocytomas: treatment with unconventionally fractionated external beam stereotactic radiation therapy*, Radiol. **171**: 565-569, 1989.

41. J.G. Schwade, P.V. Houdek, H.J. Landy, J.L. Bujnoski, A.A. Lewin, A.A. Abitol, C.F. Serago and V.J. Pisciotta, *Small field stereotactic external beam radiation therapy of intracranial lesions: fractionated treatment with a fixed-halo immobilization*, Radiol. **176**: 563-565, 1990.

42. L. Souhami, A. Olivier, E.B. Podgorsak, J.-G. Villemure, M. Pla and A.F. Sadikot, *Fractionated dynamic stereotactic radiotherapy for intracranial tumours*, Cancer **68**: 2101-2108, 1991.

43. B.G. Clark, E.B. Podgorsak, L. Souhami, A. Olivier, K.E. Sixel and J.-L. Caron, *A halo-ring technique for fractionated stereotactic radiotherapy*, Brit. J. Radiol. **66**: 522-527, 1993.

44. E.B. Podgorsak, L. Souhami, J.-L. Caron, M. Pla, B. Clark, C. Pla and P. Cadman, *A technique for fractionated stereotactic radiotherapy in the treatment of intracranial tumours*, Int. J. Radiat. Oncol. Biol. Phys. (in press) 1993.

45. R.D. Brown, D.O. Wiebers, G. Forbes, W.M. O'Fallon, D.G. Piepgras, W.R. Marsh and R.J. Maciunas, *The natural history of unruptured intracranial arteriovenous malformations,* J. Neurosurg. **68**: 352-357, 1988.

46. L. Steiner, L. Leksell, T. Greits, D.M.C. Forster and E.-O. Backlund, *Stereotaxic radiosurgery for cerebral arteriovenous malformations. Report of a case*, Acta Chir. Scan. **138**: 459-464, 1972.

47. L. Steiner, *Stereotactic radiosurgery with the Cobalt-60 gamma unit in the surgical treatment of intracranial tumours and arteriovenous malformations*, in: Operative Neurosurgical Techniques -

Indications, Methods and Results, H.H. Schnidek, W.H. Sweet (eds.), W.B. Saunders, Philadelphia, 1988, pp. 515-529.

48. R.N. Kjellberg, K.R. Davis, S. Lyons, W. Butler and R.D. Adams, *Bragg peak proton beam therapy for arteriovenous malformations of the brain*, Clin. Neurosurg **31**: 248-290, 1983.

49. G. Norén, J. Arndt, T. Hindmarsh and A. Hirsch, *Stereotactic radiosurgical treatment of acoustic neurinomas*, in: Modern Stereotactic Neurosurgery, L.D. Lunsford (ed.), Martinus Nijhoff, Boston, 1988, pp. 481-489.

50. J.C. Flickinger, L.D. Lunsford, R.J. Coffey, M.E. Linskey, D.J. Bissonette, A.H. Maitz and D. Kondziolka, *Radiosurgery of acoustic neurinomas*, Cancer **67**: 345-353, 1991.

CHAPTER 2

EXPERIMENTAL APPARATUS AND TECHNIQUES: MEASUREMENTS

2.1 Introduction

The apparatus used to generate and measure the physical parameters of photon beams is discussed in this chapter. Two high energy linear accelerators (linacs), one producing a 10 MV x-ray beam (Clinac-18, Varian Associates, Palo Alto, California) and the other producing 6 MV and 18 MV x-ray beams (Clinac-2100 C, Varian Associates), were used as high energy x-ray beam sources. These accelerators also generate electron beams, which were used to study specific scattered electron effects in some experiments. To make the linacs suitable for dynamic radiosurgery, minor adaptations are needed. These adaptations relate to the beam collimation system and to the remote control of the couch rotation. Finally, a superficial x-ray unit (Dermopan, Siemens AG, Erlangen, Germany) was used to obtain a low energy x-ray beam. The superficial beam enabled comparisons with a scattered high energy photon or electron beam.

Beam characteristics were studied with a variety of detectors in tissue-equivalent phantoms. A 3-dimensional isodose plotter (RFA-7, Therados, Uppsala, Sweden) with p-type semiconductors and ionization chambers was used for beam measurements in water, while an end-window parallel-plate ionization chamber (Model 2532/3, Nuclear Enterprises, Beenham, England) was used for measurements in a polystyrene phantom. Radiotherapy radiographic film (XV-II ready pack film, Eastman Kodak, Rochester, New York) was used in the measurement of two dimensional dose distributions. Irradiations of these films in polystyrene phantoms were subsequently analysed with a 2-dimensional radiographic film densitometer (RFA-7, Therados).

The basic features of our linear accelerators are given first, and then the adaptations needed for radiosurgery are described. The characteristics of the detectors are discussed and the techniques used for radiographic film dosimetry are explained. Finally, the phantoms used in conjunction with each of the detectors are described.

2.2 Radiation sources

2.2.1 *LINEAR ACCELERATORS*

A single energy 10 MV linear accelerator and a dual energy 6 MV and 18 MV linac were used as radiation sources in our experiments. The 10 MV linac is installed in the Radiation Oncology department of the Montreal General Hospital and has been in clinical use for conventional radiotherapy for the past 15 years. In 1986, minor adaptations have extended its use to radiosurgery. The linac is isocentrically mounted, with a source-axis distance (SAD) of 100 cm and the isocenter 130 cm above the floor. Used in either electron or photon mode, it can produce electron beam energies of discrete values between 6 MeV and 18 MeV, or a 10 MV x-ray beam with a spectrum of photon energies ranging from 0 MeV to a maximum of 10 MeV.

The dual energy linac, Clinac-2100 C, is located at the Sir Mortimer B. Davis Jewish General Hospital in Montreal. Installed in 1990, it is used exclusively for standard radiotherapy, and not for clinical radiosurgery. However, the collimation system used to generate radiosurgical beams on

the 10 MV linac can also be installed on the dual energy machine which enabled us to study the effects of x-ray energy on the properties of radiosurgical beams. This linac produces electron beams with five energies in the range from 6 MeV to 20 MeV and two x-ray beams with photon spectra ranging from 0 MeV to 6 MeV in one and 0 MeV to 18 MeV in the other. Although the dual energy machine is more modern than the older Clinac-18 the basis of operation for the two linacs is the same and the general discussion presented below applies to both machines.

Figure 2.1 shows a schematic diagram of a typical linac (1). Operating in the S-band at 2856 MHz, the machine uses an rf driver as the source of radiofrequency (rf) and a klystron operating in the megawatt range as the rf amplifier. A rectangular waveguide conducts the microwave power pulses from the klystron to the accelerating structure. The electron gun acts as the source of electrons to be accelerated. The accelerating structure itself is a disk loaded standing wave accelerator, containing 21 accelerating cavities. Operating at a vacuum pressure of about 10^{-7} torr, the accelerating waveguide is sealed from the outside environment with a 0.25 mm thick beryllium window.

A detailed diagram of the linac head (2) is given in Fig. 2.2. After leaving the accelerating waveguide, the electrons enter the beam transport section where they are bent through 270° by a quadrupole bending magnet, in which a ±10% beam energy spread is brought to a single focal point. When operating in the photon mode, the electron beam hits a copper target, its thickness depending on the x-ray beam energy required. In the target, the kinetic energy of the electrons is transformed into a bremsstrahlung x-ray spectrum. The target is placed into the bending magnet focal spot

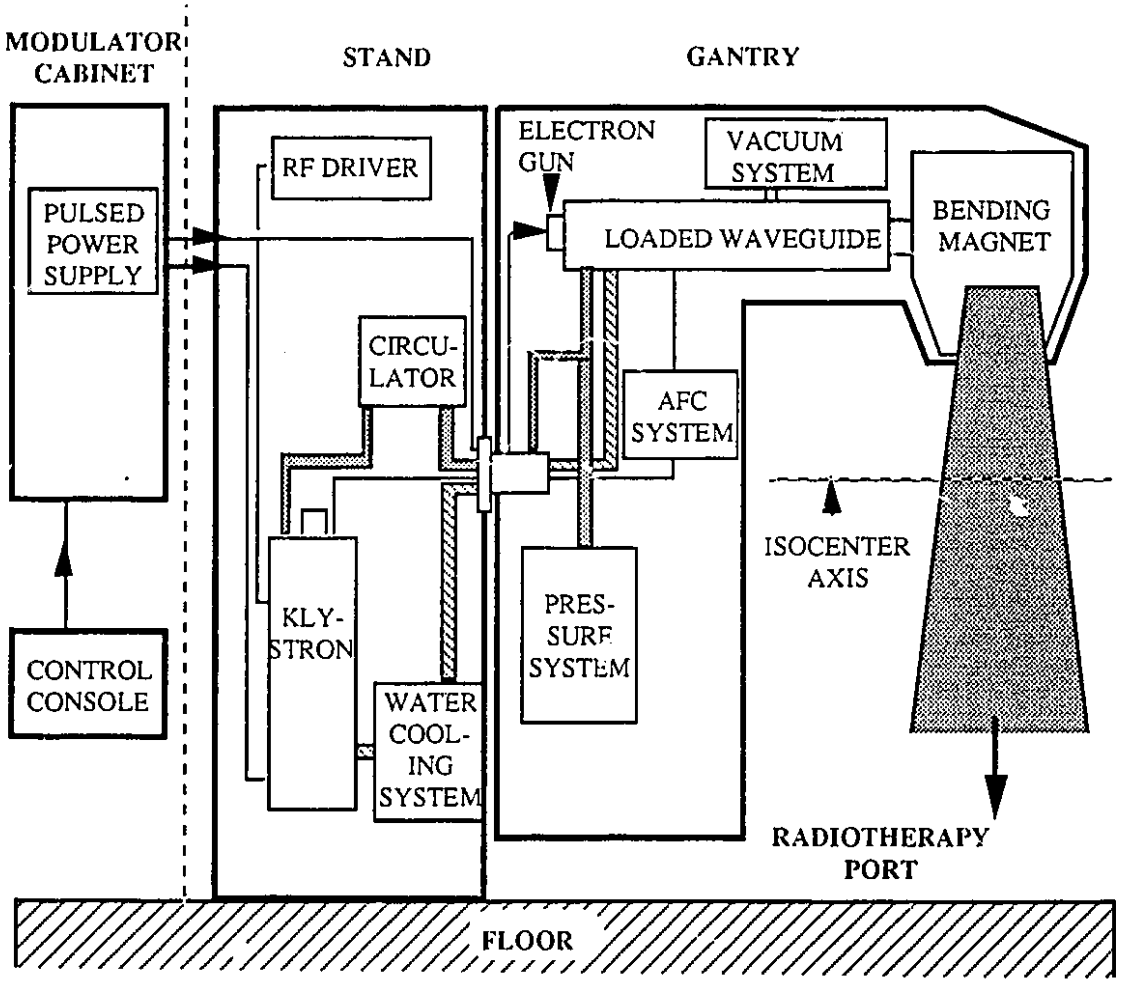

Figure 2.1 Schematic diagram of a typical isocentric linear accelerator showing the basic components.

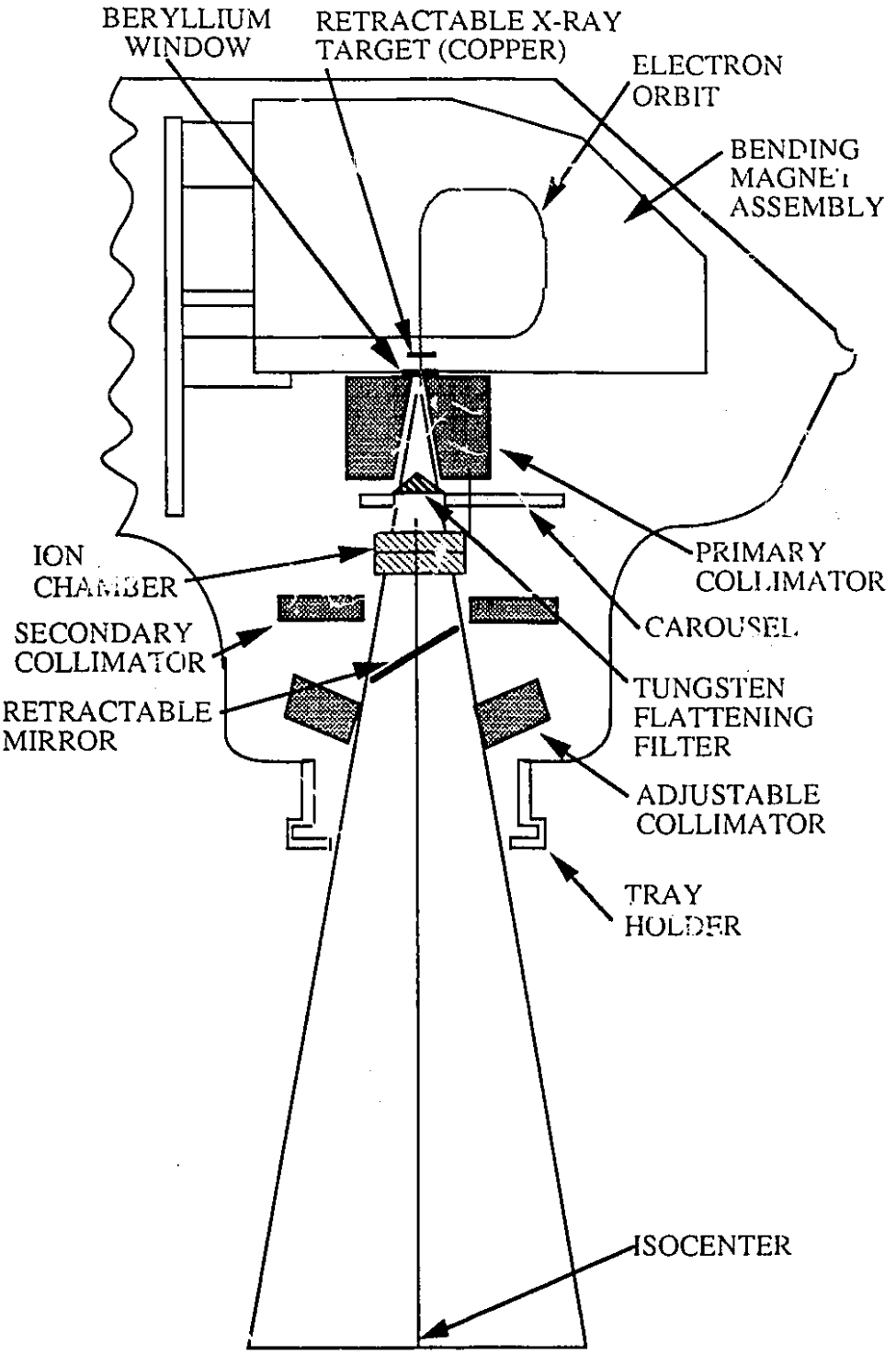

Figure 2.2 Detailed schematic diagram of the linac head when operating in the photon mode.

inside the evacuated beam transport system and the photons exit through the beryllium window. In the electron mode, the target is moved out of the electron beam, allowing the monoenergetic electrons to pass straight through the beryllium window.

A primary collimator in the proximity of the vacuum window defines the maximum attainable circular field size. Upon leaving the target, the photon beam is sharply peaked in the forward direction and is therefore passed through a tungsten flattening filter in order to produce a uniform radiation field over the maximum field size defined by the primary collimator. The flattening filter is mounted on a rotating carousel for easy interchange between photon and electron radiation modes. In the electron mode the filter is replaced by a scattering foil which spreads the narrow pencil beam over a larger field size, forming the clinically useful electron beam.

The flattened photon beam (or scattered electron beam) then passes through a dual transmission ionization chamber. The charges collected on the measuring electrodes of the two chambers are amplified and measured in arbitrary units, usually referred to as monitor units (MU). The sensitivity of the primary ionization chamber is adjusted so as to correspond to dose (cGy) in water at the depth of dose maximum when irradiated with a 10x10 cm^2 field at a distance of 100 cm from the x-ray target. The radiation beam is switched off when a preset number of monitor units is attained. The two ionization chambers are independent to provide a redundancy check for improved safety.

A fixed secondary tungsten collimator limits the maximum square field size to 35x35 cm^2. The desired square or rectangular photon treatment

field size is then defined by adjustable collimators, consisting of four tungsten blocks. To provide sharp edges of treatment fields, the movements of the tungsten blocks are confined to arcs, so that their faces present a flat edge to the beam diverging from the target. These adjustable collimators are fixed to a collimator head which can rotate about the vertical beam axis, allowing arbitrary angulation of fields. The position of the radiation field may be checked by a light beam, which coincides with the radiation field and is reflected into the beam path through a mirror. This mirror is removed when the radiation beam is on. Accessories to modify x-ray fields slide into slots of a tray holder which is attached to the treatment head, 65 cm below the target.

The high energy linacs have a variable dose rate with a maximum at ~500 MU per minute. They can also deliver radiation while rotating through a predefined arc, in either a clockwise or counter-clockwise direction. Precisely controlled dose rates from 0.01 MU to 9.0 MU per degree of gantry arc are then possible. The gantry has three speeds of rotation in the range from 0.1 rpm to 0.4 rpm. Once the number of monitor units per degree and the degrees of gantry rotation are set, the speed of rotation and pulse repetition frequency are then automatically fixed to achieve the desired dose rate.

The treatment couch has motor driven vertical, lateral and longitudinal motions, allowing for motorized placement of the target to the isocenter. The couch can also rotate about a vertical axis which is perpendicular to and intercepts the gantry axis of rotation and passes through the isocenter.

Three laser localization devices are used to precisely indicate the location of the isocenter, one is mounted on the ceiling and the other two are on the side walls of the treatment room. The ceiling laser shows the couch vertical axis with a dot 1 mm in diameter, while the two lateral lasers designate the height of the isocenter with crosses of line widths of ~1 mm.

The physical considerations of the gantry and treatment couch show that there are three degrees of freedom for treatment set-up, all related to the isocenter as a common reference point. These degrees of freedom are shown schematically in Fig. 2.3. If one considers a coordinate system fixed in space, with its origin at the isocenter, all other frames of reference are rotations and translations of this system. The gantry and couch rotations, θ and ϕ, respectively, have already been discussed in *Chapter 1* where in Fig. 1.3 we defined the angular convention used in our center. The collimator itself, lying in the plane perpendicular to the beam axis, can also rotate clockwise or counter-clockwise about its axis, through an angle defined as ψ.

2.2.2 *LINAC ADAPTATIONS FOR RADIOSURGERY*

Adaptations must be made to standard linacs before they can be used for radiosurgery. Some centers purchase commercially available radiosurgery kits containing the linac adaptations required. In our case all necessary additions and alterations to the 10 MV linac were constructed and implemented by the Department of Medical Physics at the Montreal General Hospital.

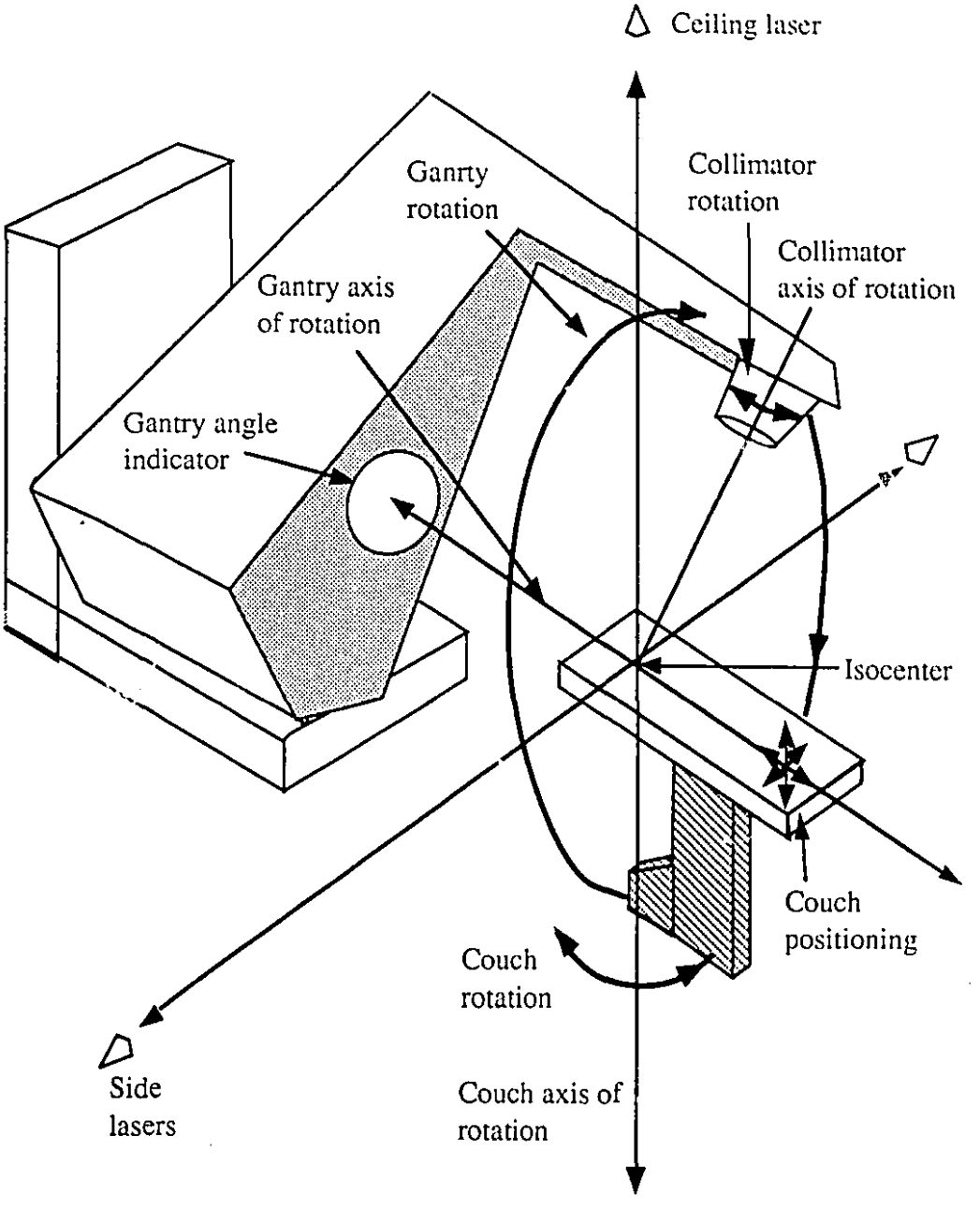

Figure 2.3 Degrees of freedom for treatment set-up on a linear accelerator. The gantry rotates about a horizontal axis of rotation, the couch about a vertical axis and the collimator rotates about the beam axis. All axes of rotation intersect at the isocenter which is indicated by means of of two side lasers and one ceiling laser.

Additional collimation is needed for use in radiosurgery to achieve the small, well defined circular treatment fields. A typical collimator used in our center and its placement into the radiation beam are shown schematically in Fig. 2.4. The collimator consists of two lead cylinders, each 5 cm high and 5 cm in diameter, lying on top of each other and straddling a 0.65 cm thick Lucite plate. This enables placement of the collimator assembly into the tray holder of the linac in the path of the photon field. The linac adjustable collimator jaws are fixed to give a field size of 4×4 cm^2 at the isocenter. Small cylindrical apertures were drilled into each half of the lead collimator, such that the geometrical beam divergence determines the diameter of the hole in the top and bottom halves of the collimator, as shown in Fig. 2.4. The nominal field diameters at the isocenter of the radiosurgical collimators in our set range from 0.5 cm to 3.5 cm in steps of 2.5 mm.

Remotely controlled couch motorization has been installed on the 10 MV linac by the Department of Medical Physics to enable simultaneous couch and gantry rotation during the radiosurgical treatment. The couch rotation is monitored by means of an angular position readout on the machine console. The couch rotation is run by the gantry rotation control circuitry and its speed is fixed to be one half the gantry's speed. This addition is specific to the radiosurgery technique which was developed at McGill University and is referred to as the dynamic rotation.

A bracket is attached to the head of the treatment couch to fasten the stereotactic frame to the couch and to immobilize the patient during treatment. During the treatment, i.e., while the couch is rotating, a brake which immobilizes lateral and longitudinal couch motions is enabled to

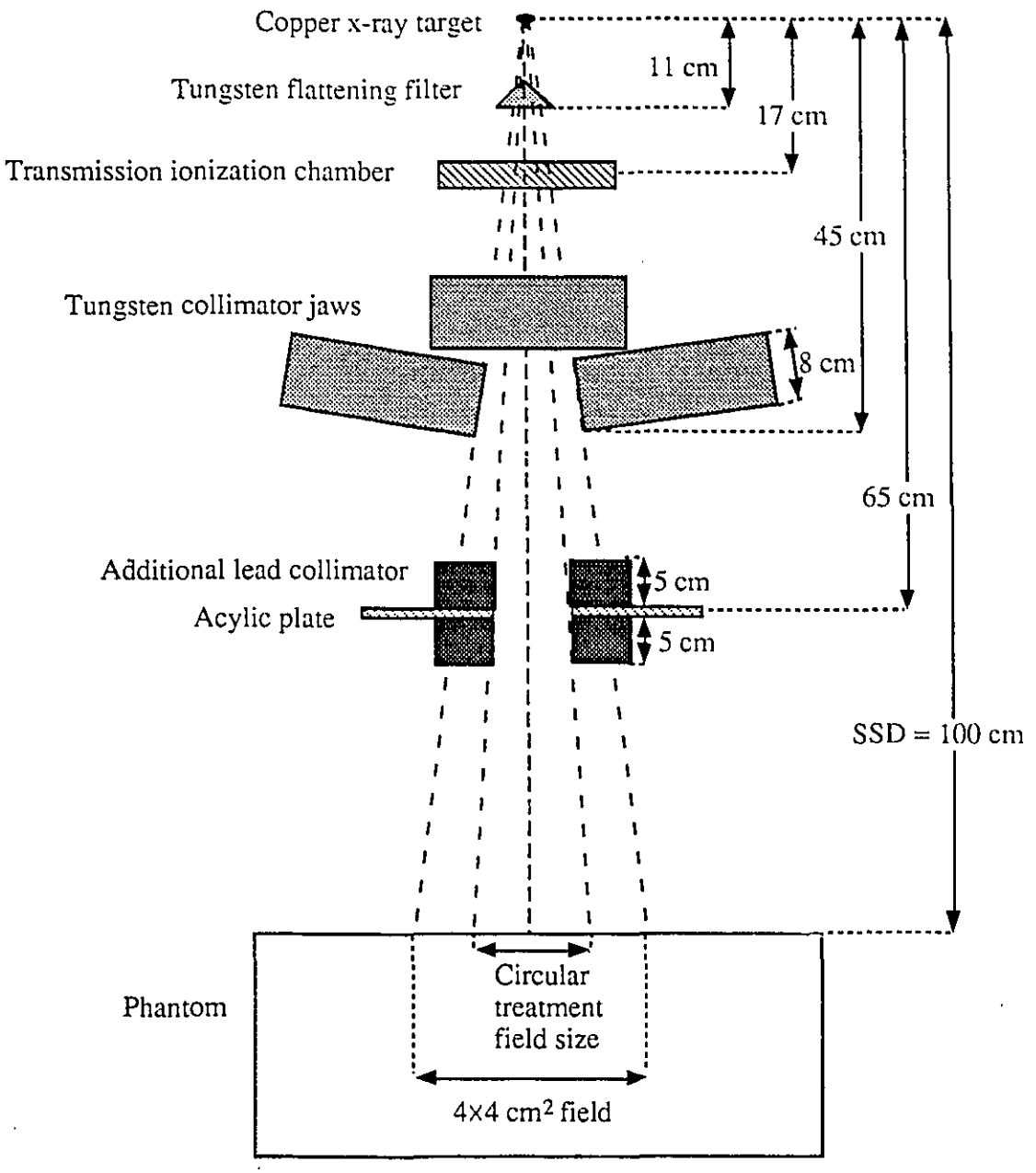

Figure 2.4 Geometry of the set-up used to obtain the radiosurgical beams. The beam is traced from the copper target, through the flattening filter and transmission chamber, and collimated by the machine collimator jaws, set to a field size of 4x4 cm^2 at isocenter. It is then further defined by additional lead collimators placed in the tray holder of the gantry. These radiosurgical collimators produce circular field sizes ranging in diameter from 0.5 cm to 3.5 cm at the isocenter.

ensure that shifting of the target volume from the isocenter cannot occur. The height of the couch as well as the couch angle are continuously monitored during the radiosurgical procedure. A change of couch height by more than 1 mm or an excessive discrepancy between the couch angle ϕ and the gantry angle θ (i.e., if $2\phi-\theta<>3°$) shuts the radiation off.

2.2.3 *LOW ENERGY X-RAY MACHINES*

In some of the experiments reported in *Chapter 7*, a low energy x-ray beam was studied to allow comparison with a scattered high energy photon or electron beam. The source of the low energy beam was a contact therapy tube, operating in the superficial energy range. The unit is installed at the Sir Mortimer B. Davis Jewish General Hospital and is used clinically primarily in the treatment of rectal carcinomas through the endocavity rectal irradiation technique. Therapeutic x-ray units operate in a manner similar to diagnostic x-ray machines. At the cathode, electrons are emitted by a tungsten filament and then accelerated through a potential difference towards a tungsten anode. At the anode, the electrons are stopped in the tungsten, emitting x-rays consisting of bremsstrahlung and characteristic radiation resulting from the electron braking process. These x-rays are then collimated to a well defined beam. At this point the x-ray beam is filtered with copper or aluminum to obtain the desired beam energy. For low energy x-rays, the beam energy is characterized by the accelerating potential and by the beam half value layer (HVL).

The superficial unit used in our experiments is operated at 50 kVp with a tube current of 25 mA. The x-ray tube is water cooled, has an outside diameter of 8 cm, and an x-ray port which is perpendicular to the tube housing axis. The tube is equipped with a beryllium window and a grounded ring anode. A proctoscopic cone made of stainless steel defines the field sizes at 22 cm from the target. They range from 2 cm to 3 cm in diameter, depending on the cone chosen. Aluminum filters are used to obtain the desired depth dose characteristics, hardening the beam by attenuating low energy x-rays.

2.3 Measuring devices and detectors

2.3.1 *RADIATION FIELD ANALYSER (RFA)*

Beam parameters were measured with a variety of detectors and techniques which are described in this chapter. Ionization chambers, semiconductors and radiographic film were used as radiation detectors, all in conjunction with a radiation field analyser, or independently with an electrometer.

A radiation field analyser was used as a 3-dimensional isodose plotter in the measurement of beam data or as a 2-dimensional radiographic film densitometer to measure two-dimensional dose distributions. The analyser is controlled through a computer system based on an 80186 16-bit processor with a 20 megabyte hard disk. A software program MSDISK allows the transfer of beam data from a hard disk to a 5

1/4 inch floppy disk. Data was analysed on an IBM compatible micro-computer based on a MS DOS operating system.

When used as a three dimensional isodose plotter, the RFA plotter consists of a Lucite water tank with dimensions of 63x60x61 cm^3. A remotely controlled drive unit positions the radiation detector within a scanning volume of 50x50x50 cm^3. Diodes or ionization chambers are available as detectors, and an electrometer measures the signal received from them. For both measuring modalities two detectors are needed, one, serving as a reference, is stationary in the radiation beam and the other is moveable in the beam to measure ionization as a function of the chamber position in the beam. The signals from the two chambers pass through a differential amplifier and the result is digitized and stored. Using the ratio of signals between the reference and the detector minimizes the effects of fluctuations in the radiation beam intensity during the measurement. The positioning accuracy of the moveable detector is 0.5 mm, with a reproducibility of ±0.1 mm.

2.3.2 *FILM DOSIMETRY*

Film commonly used in diagnostic radiology imaging is also suitable as a relative dosimetry technique. Exposure to radiation produces a latent image in the film and blackening occurs during the subsequent development and fixation of the radiographic film, a process described in detail in the literature (3). When film is used as a dosimeter, the charateristic curve of the particular film is used to asses film response to

radiation dose. The characteristic curve gives the relationship between optical film density and the dose, as optical density is proportional to the mass of silver present in the film, which in turn is proportional to the dose. A measured optical density is thus related to a corresponding dose.

Film blackening depends on many parameters: film type, developer temperature, fixation procedure, etc. In dosimetry great care must be taken to keep these parameters constant, so that any change in optical density is due only to a change in dose. Some degree of film blackening will occur even with no irradiation. This is referred to as the film fog, and must be subtracted from all measured optical densities to establish a true zero point on the characteristic curve. At high radiation doses, above 100 cGy, the characteristic curve begins to saturate, until at doses near 300 cGy the changes in optical density with dose are too slight to detect easily. Thus, care must be taken to irradiate the films to doses well below saturation.

The radiographic film used in our experiments was of the type used for portal imaging of radiotherapeutic procedures (Kodak XV II). Beam data acquired with the radiographic film was analysed with the commercially available RFA plotter used as a 2-dimensional film scanner. In the RFA densitometer a transparent Lucite plate which holds the film is placed above the water tank. The optical system is driven by two independent motors, moving both the detector and light source simultaneously within a 50×50 cm^2 scanning area. The light source is a tungsten filament incandescent lamp and the detector consists of a silicon photodiode with an active area of 1.6 mm^2, sensitive to light with a wavelength ranging from 400 nm to 1150 nm and a spectral response peak at 925 nm when the Lucite window is in place. Optical lenses are used to

focus the light spot. The spatial resolving capability of the densitometer is about 0.8 mm.

2.3.3 *IONIZATION CHAMBERS AND SEMICONDUCTORS*

Detector size and its corresponding spatial resolution is a very important factor, given the small field dimensions of the beams used in radiosurgery. The cross-section of the detector's sensitive volume must be considerably smaller than the beam diameter and completely contained within the beam, as any charge or current measured due to the creation of ions upon irradiation must be related to a known mass in order to determine the dose. This criterion puts a substantial restriction on suitability of detectors, as the fields to be measured have diameters on the order of a few cm. Therefore, only small volume ionization chambers and semiconductors were used in our measurements of radiosurgical beam data.

The diode detectors were p-type silicon semiconductors, requiring about 3 eV to produce an electron-hole pair, with the resulting current proportional to the dose received. They operate in the photovoltaic mode, so that no potential difference across the device is required. The outer dimensions of the cylindrical detector are 7.0 mm for the diameter and 25 mm for the height. The outer material is an epoxy resin, coated with a thin layer of water resistant paint. The silicon crystal itself has a sensitive diameter of 2.5 mm and a thickness of 60 μm. The measuring volume lies 0.55 mm below the detector's surface.

The diode proved to be the most suitable detector for beam measurements in air because of its small volume-of-interest. In order to ensure electronic equilibrium the high energy of the linac beam requires that a build-up cap covers the detector when beam parameters are measured in air (4). If made of a tissue equivalent material, the caps would require thicknesses on the order of a few cm for the high energy beams, making the detector plus cap diameter larger than the diameter of most radiosurgical beams. The use of brass as a build-up material allowed the caps to range in thicknesses from 2 mm to 3.5 mm in the energy range from 6 MV to 18 MV. The semiconductor detector and build-up cap were thus smaller than 15 mm in diameter, enabling them to be completely contained within all but the smallest field size studied. Since only doses relative to a standard 10×10 cm^2 field were measured in air, the lack of tissue equivalence of brass was not considered.

In an ionization chamber, the measured signal is related to the ions produced and collected during irradiation. Both thimble and parallel-plate ionization chambers were used in our experiments. Practical thimble ionization chambers contain a charged electrode in the chamber's central air cavity. The wall of the chamber is made of an air-equivalent material, with an inner coating of conducting material. This geometry results in a cylindrical electric field. A parallel plate chamber, on the other hand, contains two charged plates separated by some distance thus creating an electric field with parallel geometry. Guard rings ensure a uniform field in the volume-of-interest. The principles of operation are of course the same for both the thimble and parallel plate chambers. A known mass of air is irradiated, the ions produced by radiation are collected, and the charge

measured is related to dose in the irradiated medium through a chamber calibration factor which is obtained from the National Standards Laboratory in Ottawa.

The ionization chambers used with the RFA isodose plotter are thimble ionization chambers with outer dimensions of 7.0 mm for the diameter and 25 mm for the height. The air cavity itself has a diameter of 4.0 mm and a length of 10 mm and contains a central electrode 9 mm in length. The thimble is made of Lucite with an inner graphite wall. A typical polarizing potential voltage of 250 V is applied to the chamber.

An end-window parallel plate ionization chamber was used for percentage depth dose measurements in the dose build-up region. The chamber has an electrode separation of 1.0 mm, a sensitive diameter of 3 mm and a diameter including the guard ring of 5.2 mm. Its polyethylene wall has a thickness of 2.5 mg/cm^2. The chamber is used with a polarizing voltage of 300 V. The charge collected was read with an electrometer (model 616, Keithley Instruments Inc., Cleveland, Ohio) with a calibration factor traceable to the National Standards Laboratory in Ottawa.

2.4 Phantom materials

Phantoms simulating soft tissue were used in conjunction with the dosimeters described above. The RFA unit, with its semiconductors and thimble ionization chambers, allows 3-dimensional scan measurements in water. Sheets of polystyrene, ranging in thickness from 0.6 mm to 3.2 mm, were used with both the parallel plate chamber and film. For some

experiments, dose was measured in lead using lead sheets with thicknesses of 0.47 mm.

When measuring the dose distributions resulting from radiosurgical treatment simulations or some other combination of radiation beams, a spherical phantom was used in conjunction with radiographic film as a detector. The phantom consisted of 54 sheets of polystyrene, each 0.32 cm thick with variable radius, so that when the circular sheets were stacked together, they resulted in a sphere with a radius of 8.64 cm approximating the dimensions of a human head. Sheets of film could be placed between any two layers of the phantom, and the phantom could have arbitrary orientation, allowing the measurement of dose in any plane at any orientation for a given radiosurgical technique.

2.5 Summary

In this chapter we discuss the basic experimental apparatus and techniques used to generate and measure dose distributions. Linacs, which provide the source of x rays for radiotherapy are described in general, and then the modifications needed for radiosurgery are presented. These modifications consist mainly of extra collimation to achieve the desired fields and of remote couch rotation control. A further radiotherapy machine, a superficial x-ray unit used to compare the characteristics of a low energy x-ray beam to that of a high energy scattered beam is also described.

The radiation detectors are discussed with respect to their ability to adequately measure properties of the narrow radiosurgical radiation beams. Given that even small detectors have diameters of the same order of magnitude as the photon beams to be measured, the question of spatial resolution must be addressed. Radiographic film, which collects a two dimensional dose distribution, is an appropriate detector for treatment simulations, so the particular film dosimetry technique used is explained. The characteristic curves describing the density *vs* dose relationship of the film can be used to convert an optical density measurement to dose. Finally, the phantoms used to simulate tissue are described.

2.6 References

1. C.J. Karzmark and R.J. Morton, *A primer on theory and operation of linear accelerators in radiation therapy*, U.S. Department of Health and Human Services, Food and Drug Administration, Bureau of Radiological Health, Rockville, Maryland, 1981.
2. Customer course documentation on Clinac-18 maintenance, Varian Associates, Palo Alto, California.
3. T.S. Curry, J.E. Dowdey and R.C. Murry, *Christensen's introduction to the physics of diagnostic radiology*, 3rd edition, Chap. 10, Lea & Febiger, Philadelphia, 1984.
4. H.E. Johns and J.R. Cunningham, *The physics of radiology*, 4th edition, Charles C. Thomas, Springfield, Illinois, 1983, p. 239.

CHAPTER 3

EXPERIMENTAL APPARATUS AND TECHNIQUES: MONTE CARLO CALCULATIONS

3.1 Introduction to Monte Carlo calculations

Monte Carlo simulations are a means of describing, by use of a mathematical model, situations that are of a probabilistic or deterministic nature. Using machine generated random numbers, the probability distributions governing the physical process of a particular problem are sampled, thereby simulating the trajectories of individual particles. The complete trajectory of each particle is referred to as a history. By simulating a large number of histories and by keeping track of the physical properties of interest, information can be obtained about average values of macroscopic quantities and their associated distributions.

In radiotherapy physics and radiation dosimetry, electron transport must be taken into account when modelling high energy photon and/or electron beams. As electron transport is inherently a random process, this can only be done with complete generality by using a coupled electron-photon Monte Carlo code. This fact, together with the rapid increase in speed and decrease in cost of computer data processing, plus the availability of general purpose Monte Carlo software packages, has led to a dramatic increase in the use of Monte Carlo calculations in the field of medical physics over the past decade.

Monte Carlo techniques are especially useful in situations where analytical solutions are not possible, because of complexities of the electron and photon transport. They allow us to obtain information about measurable quantities, such as energy deposition per unit mass, etc. Moreover, one can use Monte Carlo techniques to answer questions which cannot be addressed by experimental investigations. For example, in radiation dosimetry these calculations can be used to differentiate between

primary and scattered dose deposition, to count the number of interactions a given particle undergoes, or to determine the origin and direction of a secondary particle. Thus Monte Carlo techniques act as a tool to improve our understanding of a particular measurement or result by allowing us to examine individually the composite parts of a measurement. Monte Carlo calculations can also serve as a means of testing the viability of new theories or techniques prior to their physical implementation.

Probabilistic transport codes were first developed to study neutron diffusion in fissionable materials for nuclear reaction applications in Los Alamos, California. This problem is relatively simple, because the number of interactions the neutrons undergo is low enough to allow an explicit simulation of each event (1). The situation is more complex for electrons, which undergo a large number of interactions. Currently, there are two codes in widespread use for electron transport: the ETRAN (*electron transport*) code developed by the National Bureau of Standards, USA in 1973 (2), and the EGS (*electron-gamma-shower*) code developed at the Stanford Linear Accelerator Center (SLAC) in California in 1978 (3). The fourth version of the EGS code (EGS4) is now available and was used in the Monte Carlo calculations presented in this thesis.

Generally the Monte Carlo codes have four basic components (1) as follows: (i) the cross-section data for all processes considered in the simulation; (ii) the algorithms for particle transport; (iii) the specifications for the problem at hand, such as the geometry or the quantities of interest to be counted; and (iv) the analysis of the information obtained from the simulation. The physics of the situation is essentially determined by the first two components, while the latter two are more user-specific.

3.2 The EGS4 code

3.2.1 *CAPABILITIES AND FEATURES*

The EGS4 code can simulate the radiation transport of electrons, positrons or photons in any element, compound or mixture. The data used by EGS4 is generated from cross-section tables for all elements with atomic numbers ranging from 1 through 100, taken from the work by Berger and Seltzer (4) which has since been adopted by the ICRU in their Report # 37 (5). The dynamic range of charged particles is from 10 keV to several 1000 GeV, while that of photons is from 1 keV to several 1000 GeV. Below the cut-off values, particle transport does not take place and the energy is assumed to be deposited locally. The high maximum energies reflect the fact that the EGS4 code was first developed for high energy physics, as opposed to medical physics applications.

As the electron travels through matter, it can lose energy through collisional or through radiative processes. In collisional loses, the electron interacts with atoms, leaving them in excited or ionized states. The ejected electrons will deposit their energy locally, or, if given enough kinetic energy, will travel though the medium as delta rays. This process dominates at low energies.

At higher energies, radiative losses predominate, resulting in the production of bremsstrahlung photons. These photons mainly interact with the medium in one of three ways (photoeffect, Compton effect, pair production), depending on their energy and the type of medium. At high photon energies, pair production is the most probable effect, while at intermediate energies Compton scattering predominates. These two

processes return energy to the medium in the form of scattered electrons or electron-positron pairs. These secondary electrons then also undergo bremsstrahlung or collisions as they move through the medium. This multiplicative character is known as an electromagnetic cascade shower (3). Very low energy photons mainly interact with the medium via the photoeffect. This, plus multiple Coulomb scattering of electrons, perturbs the shower somewhat, giving it a lateral spread. When the electron energy falls below a critical energy in the medium (where collisional and radiative losses occur with equal probabilities), radiative losses can no longer compete with collisional losses and the electron kinetic energy is dissipated in the medium. At large shower depths, low energy photons predominate.

Thus, through the course of a shower various physical processes occur, all of which are taken into account by the EGS4 code. Photons undergo pair production, Compton scattering, photoeffect and coherent (Rayleigh) scattering, while electrons can experience bremsstrahlung production, positron annihilation in flight or at rest, Molière multiple scattering, Møller (e^-e^-) and Bhabha (e^-e^+) scattering, as well as a continuous energy loss between successive discrete interactions.

3.2.2 *PROGRAM STRUCTURE AND SUBROUTINES*

The EGS4 Monte Carlo code consists of four basic components: (i) the *PEGS4* preprocessing code which outputs cross section data for materials specified by the user in a form suitable for direct use by EGS4; (ii) EGS4 itself, the package of subroutines and block data which is accessed by a user-written interface; (iii) a user-written subroutine *HOWFAR* that

specifies the geometry of the problem; and (iv) a user-written subroutine *AUSGAB* that allows the user to score and output information.

A schematic diagram of the EGS4 structure is given in Fig. 3.1 (3). The figure is divided into two sections, one representing the user-written code and the other representing the EGS4 package of subroutines. Both sections are distinct from one another. This gives the user flexibility in formulating a particular situation without requiring an in-depth knowledge of the transport code details.

The user-written *MAIN* program contains all the initialization operations and the calls to the subroutines *HATCH* and *SHOWER*. First, the number and types of media are fixed and then *HATCH* is called to establish the media data. *HATCH* reads the cross-section data from a *PEGS* output file, which must be generated prior to the simulation. Incident particle parameters are then determined. The user must specify particle type (electron, positron or photon), its total energy, its minimum and maximum energies, its initial coordinates and initial direction cosines, and the number of histories to run. For each particle with its initial parameters the subroutine *SHOWER* is called. Here, the actual particle transport begins. *SHOWER* then calls the subroutines governing the transport, for either an electron, positron, or a photon. The possible discrete interactions are listed in the flow chart of Fig. 3.1. *UPHI* is a subroutine that determines the particle's direction cosines following an interaction.

The *MAIN* program must also contain a code section to output, and possibly analyse, the results that were collected during the simulation. To obtain a statistical analysis of the computed results, a given number of histories can be run in a user-specified number of batches. Each batch is a

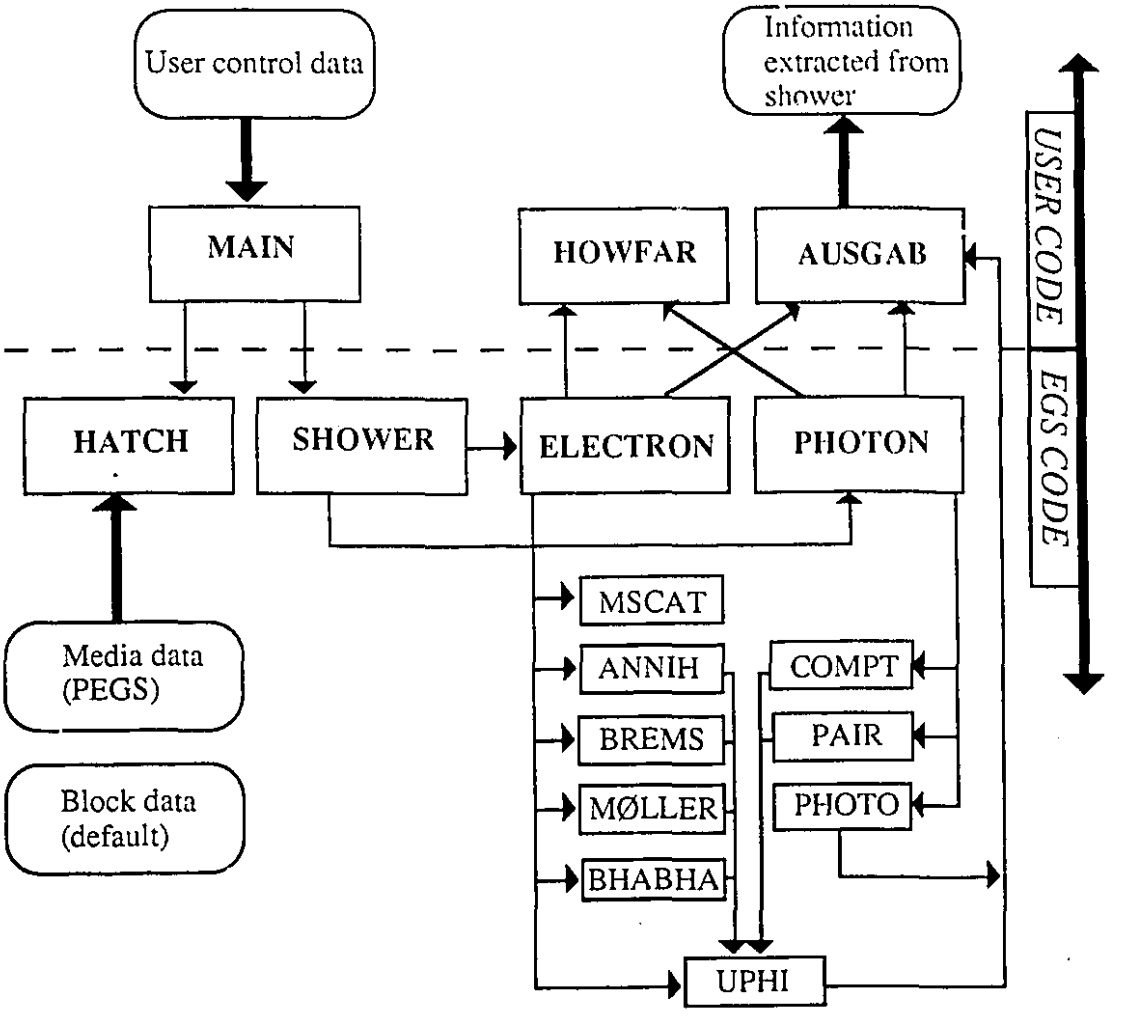

Figure 3.1 Flow chart of the EGS4 Monte Carlo code.

complete simulation of the specified number of histories. The results of each batch can be stored separately and then averaged, giving a measure of error to the computed results.

The user-written subroutine *HOWFAR* defines the geometry of the problem and divides it into regions. Each region has a definable size, density and composition. The user also defines a discard region, i.e., a region that lies beyond the geometry of interest for a particular simulation. By default, this subroutine is interrogated by *ELECTRON* and *PHOTON*, the subroutines determining electron and photon transport, respectively, after each particle step. The particle step size, i.e., the distance between discrete interactions is found, and the distance to the nearest region boundary along the current direction is calculated. These values are compared, and if the distance to a boundary is smaller than the step size, the particle crosses over into the new region. A particle is tracked until it enters a discard region or until its energy falls below the specified cut-off energy. Once the latter occurs, the particle's remaining energy is deposited locally.

The statement *AUSGAB(IARG)* is used to call the user-written subroutine *AUSGAB*, where the argument corresponds to a particular condition. EGS4 allows for 25 conditions to output data, for example when a particle's energy falls below the cut-off, before or after a given interaction has occured, after a particle has been transported a given distance, or when a particle travels in a specified direction. Once these conditions are established and this subroutine is called, various particle parameters can be scored, as desired by the user: the energy deposited, the number of particles reflected or transmitted through a certain region, the direction of particles leaving a given region, etc. The information to be obtained from

the particle's history must be asked for and stored in the subroutine *AUSGAB*.

3.2.3 *VARIANCE REDUCTION TECHNIQUES*

Variance reduction techniques are those which make a calculation more efficient, i.e., they reduce the time needed to calculate a particular result with a given statistical uncertainty (6). Variance and computing time are directly related: if the variance is too large, more histories must be run to reduce the errors, making the simulation more time consuming. Many techniques, either electron- or photon-specific, exist to increase the efficiency of a code. Described here are two examples of electron-specific variance reduction techniques which were implemented in the EGS4 code for the Monte Carlo calculations presented in this thesis (6,7).

As an electron travels through a given geometrical region it undergoes many thousand interactions and takes a correspondingly large number of steps. At each step, the *HOWFAR* subroutine is called. Thus, through the course of a particle's history, it becomes very time consuming to check if a boundary has been crossed after each step. One alternative, used in EGS4 (6), is to determine the distance to the geometrical boundary once, and then to decrement this variable by the length of each transport step. If, after a step has been taken, the distance variable is greater than zero, the particle cannot cross a boundary and the geometry subroutines are not called. Otherwise, the particle may cross into a new region in which case the geometry subroutines must be interrogated. For most

electron steps the first condition holds true, and unnecessary time consuming subroutine calls are avoided.

Another electron-specific variance reduction technique used by EGS4 is the *PRESTA* transport algorithm. Developed by Bielajew and Rogers in 1986 (7), *PRESTA* is an acronym that stands for *p*arameter *r*educed *e*lectron-step *t*ransport *a*lgorithm. All electron transport codes depend on step size. Reducing the electron step size ensures accurate results, while increasing computing time. A balance must be found between a small enough step size and the time needed to obtain acceptable results. Optimal step sizes are not easy to determine, requiring a detailed knowledge of the transport parameters. *PRESTA* can be implemented to overcome this problem, automatically selecting the step size suitable for a given location. Far away from boundaries, *PRESTA* allows large electron steps, while small steps are chosen close to boundaries or interfaces between media. This eliminates the problem of selecting the electron step size for the user, while ensuring that reliable results are obtained. Furthermore, computation time is saved, as large step sizes can be used where appropriate.

3.3. Hardware and compiler

The Monte Carlo calculations were performed on an AT 486 microcomputer with a clock speed of 33 MHz and 4 MBytes of RAM (Random Access Memory) (Virage Tech, Montréal, Québec). The computer runs under the MS-DOS version 5.0 operating system and has 200 MB of disk storage space. An increase in memory and disk capacities would

increase the computation speed, but it was found that the given physical situations addressed in this thesis could be simulated in a reasonable amount of time with the available hardware.

The EGS4 code is written in Mortran3, a Fortran pre-compiler that converts the EGS4 Mortran3 source code into Fortran 77 code. The Mortran language was developed specifically for use with the EGS code, and found to be compact and easily readable by EGS programmers (3). The EGS4 code has a large source code (300 kBytes) and large memory requirements (4 MBytes is about the minimum memory needed to simulate real, physical situations), thus the Fortran compiler must run under extended memory, allowing programs to exceed the 640 kByte memory limit of MS-DOS (8). The F77L/EM-32 version 5.1 Fortran compiler (Lahey Computer Systems Inc, Incline Village, Nevada) meets the requirements set by EGS4 and was used through the course of this work.

3.4 Summary

In this chapter we introduce an experimental investigation technique used throughout the course of this thesis: Monte Carlo calculations. Over the past decade, Monte Carlo techniques have experienced a widespread use in the field of medical physics, as a result of the decrease in computing time and costs as well as the availability of the EGS4 Monte Carlo code. EGS4 is a multi-purpose electron-photon transport code that is easily applied to medical physics situations. We describe the basic structure of the code: the provided subroutines which govern the particle transport and the user-written subroutines which allow the

specification of a given problem. Variance reduction techniques are easily implemented in EGS4, increasing computation speed without degrading the accuracy of the results. Two of these techniques, including *PRESTA*, which were used in the simulations, are described. Finally, the hardware and compiler used in the calculations are discussed.

3.5 References

1. D.W.O. Rogers and A.F. Bielajew, *Monte Carlo techniques of electron and photon transport for radiation dosimetry*, in: The dosimetry of ionizing radiation, vol. III, K.R. Kase, B.E. Bjärngard and F.H. Attix (eds.), Academic Press, San Diego, California, 1990, pp. 427-540.
2. M.J. Berger and S.M. Seltzer, *ETRAN, Monte Carlo code system for electron and photon transport through extended media*, Documentation for RSIC Computer dose package CCC-107, Oak Ridge Nat. Lab., Oak Ridge, Tennessee, 1973.
3. W.R. Nelson, H. Hirayama and D.W.O. Rogers, *The EGS4 code system*, SLAC report 265, Stanford Linear Accelerator Center, Stanford, California, 1985.
4. M.J. Berger and S.M. Seltzer, *Stopping powers and ranges of electrons and positrons*, NBS Report NBSIR 82-2550-A, 1983.
5. ICRU Report #37, *Stopping powers for electrons and positrons*, ICRU, Washington DC, 1984.
6. A.F. Bielajew and D.W.O. Rogers, *Variance reduction techniques*, in: Monte Carlo transport of electrons and photons, T.M. Jenkins, W.R. Nelson and A. Rindi (eds.), Plenum Publishing Co., New York, 1987, pp. 407-419.
7. A.F. Bielajew and D.W.O. Rogers, *PRESTA: The parameter reduced electron-step transport algorithm for electron Monte Carlo transport*, Nuc. Instr. Meth. Phys. Res. **B18**: 165-181, 1987.
8. S. Walker, A.F. Bielajew, M.E. Hale and D. Jette, *Installation of EGS4 Monte Carlo dose on an 80386-based microcomputer*, Med. Phys. **19**: 305-306, 1992.

CHAPTER 4

CYLINDRICAL DOSE DISTRIBUTIONS IN PSEUDODYNAMIC ROTATION RADIOSURGERY: AN EXPERIMENTAL STUDY

4.1 Introduction

Currently, most of the radiosurgical techniques which were described in *Chapter 1* use circular fields to treat, with a single isocenter, target volumes which are assumed to be spherical. For a 100% dose at the center of the target, the resulting 80% and 90% isodose surfaces are invariably spherical and cover the preselected target volume with the appropriate choice of the collimator diameter. The lower level isodose surfaces become progressively more anisotropic, reflecting the dose delivery pattern of the particular radiosurgical technique.

Studies have shown that spherical intracranial lesions are rare, and that most lesions are irregularly shaped (1). The irregular intracranial lesions can be approximated better by ellipsoidal, cylindrical, or even more complex volumes. Because the radiosurgically treated lesions are small, it could be argued that a simple spherical approximation of an irregular lesion is acceptable, although a high dose of radiation then reaches some healthy tissue encompassed by the spherical isodose surface. To solve this problem, the most recent interest in radiosurgery has been to devise a means for shaping isodose contours to conform to the shape of the actual target volume. Of course, the most important isodose surface that must be shaped is the one which is used for the prescription of the dose to the target. Usually this is a reasonably high level isodose surface to keep the dose within the target as uniform as possible.

Several methods for the shaping of isodose surfaces have been suggested, yet so far only two have been implemented clinically, one using multiple isocenters (2,3), and the other the preplanned closing of selected collimators of the gamma unit (4).

With the multiple isocenter technique, rather than approximating the irregular target with a relatively large sphere, the target is covered by several small spheres, each with its own isocenter within a certain region of the target. In principle one can expect a reasonable conformity of the irradiated volume with the irregular target volume when the dose distributions obtained from the treatment of each single isocenter with a circular beam are superimposed. However, multiple isocenters make treatment planning complicated, increase considerably the total treatment time, and produce a large dose inhomogeneity within the target volume because the dose is usually prescribed to the resulting 50% isodose surface. Similarly, the preplanned closing of selected collimators of the gamma unit cannot shape the high level isodose surfaces, which remain essentially spherical because the individual beams produced by the gamma unit are circular. Only isodose surfaces below 50% can be shaped with this technique, again resulting in large target dose inhomogeneities.

Other methods for isodose surface shaping in radiosurgery have been proposed but are not used clinically yet. One of these methods is based on the use of several circular collimators each with a different diameter in a given arc (5), another on the use of elliptical fields produced by special radiosurgical collimators (6), and, yet others, on the use of dynamic field shaping (1) or adjustable collimation (7) during the linac gantry rotation.

To irradiate target shapes which can be approximated better by cylinders than by spheres, we studied a radiosurgical technique which combines the technique of dynamic rotation on an isocentric linac with two additional degrees of freedom: the collimator rotation and the variable length of a rectangular field (8,9,10).

The technique reported here for the irradiation of cylindrical targets, is pseudodynamic; it uses a series of stationary rectangular beams, each given for a precalculated couch, gantry and collimator angle as well as rectangular field size. The technique allows us to cover cylindrical targets of arbitrary dimensions and orientations within the brain with the high level (80% and 90%) isodose surfaces, and satisfies the key requirements for radiosurgery achieving a sharp dose fall-off outside the cylindrical target and producing a uniform dose inside the target.

4.2 Cylindrical dynamic rotation

4.2.1 *PRINCIPLES OF THE TECHNIQUE*

The cylindrical dynamic rotation differs from the spherical dynamic rotation used clinically at McGill University through the use of rectangular fields and the addition of two further degrees of freedom: collimator rotation and the adjustment of the longitudinal opening of a rectangular field during the irradiation of the target. In the spherical dynamic rotation radiosurgery, which uses circular fields, there is a simple 2:1 correlation between the angle of gantry rotation θ and the angle of couch rotation ϕ. In the cylindrical dynamic rotation the collimator rotation and rectangular field size adjustment are added to the gantry and couch rotation with the 2:1 correlation between θ and ϕ. These angles, θ and ϕ were previously defined in Fig. 1.3.

A standard linac collimator defines a two dimensional field with longitudinal (length) and lateral (width) collimator openings. Depending

on the relative target, couch and gantry positions, the collimator can be rotated such that its length is aligned with the longitudinal axis of a cylindrical or ellipsoidal target, and the size of its opening can be adjusted to cover the cross-section of the cylindrical target. The lateral opening (width) of the collimator can simply be fixed to correspond to the width of the target once the longitudinal axes have been aligned. A cylindrical volume will thus be irradiated during the dynamic rotation of the gantry and the couch about the target. The task in the cylindrical dynamic rotation is to find the appropriate collimator angle and the longitudinal field size in relation to the gantry and couch angles obtained in the dynamic rotation that result in a superposition of rectangular fields at a pre-determined cylindrical target.

4.2.2 *COORDINATE SYSTEMS*

To find the relationship between collimator, couch and gantry rotation, and field size, we introduce four coordinate systems, shown in Fig. 4.1(a). The XYZ system defines the coordinate frame fixed in the treatment room, with the position of the gantry and couch centers of rotation (linac isocenter) defining the origin of this system. The gantry rotates in the YZ plane about the X axis. The angle of the gantry position θ is defined to be at $\theta=180°$ when the gantry is in a vertical, upright position with the beam pointing down. An increase in gantry angle is obtained through a clockwise rotation.

The couch rotates by an angle ϕ in the XY plane about the Z axis. The angle $\phi=0°$ corresponds to the couch positioned along the X axis, with a

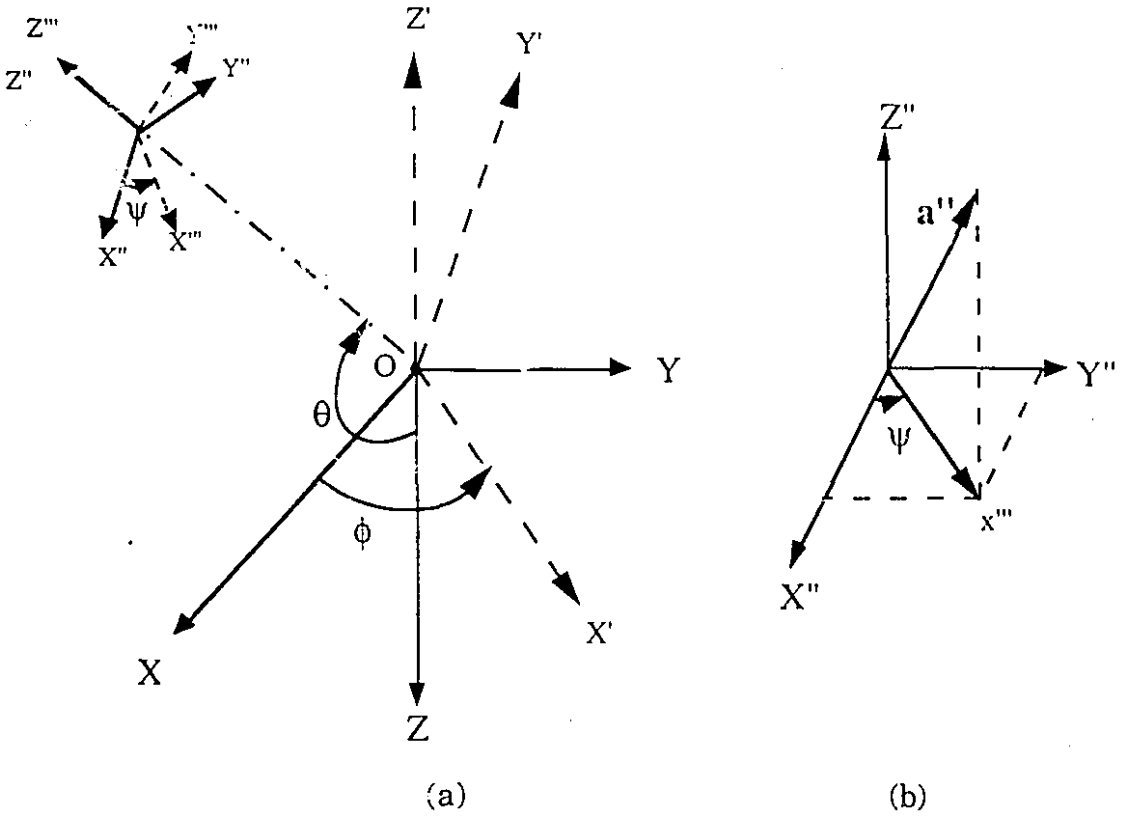

Figure 4.1 Degrees of rotational freedom and definition of coordinate systems. Part (a) shows the XYZ coordinate frame fixed in the treatment room with the origin O at the linac isocenter. The X'Y'Z' is the coordinate frame affixed to the couch and rotating with the couch through an angle ϕ in the XY plane about the Z axis. The X"Y"Z" frame, affixed to the linac gantry head, is rotated through an angle θ in the YZ plane about the X axis. The X'''Y'''Z''' is the coordinate frame affixed to the collimator. Angle ψ gives the collimator rotation in the X"Y" plane about the Z axis, which coincides with the central axis of the radiation beam. Part (b) shows the conversion to spherical coordinates within the gantry head coordinate system, with **a"** as the radial vector.

positive increase in angle given by a counter-clockwise rotation (top view). A primed coordinate frame (X'Y'Z') is defined to remain fixed with respect to the couch. The Z' axis coincides with the Z axis, except that the two directions are opposed. Note that the primed frame is simply a counter-clockwise rotation of the unprimed frame through an angle ϕ.

A frame of reference with a coordinate system X"Y"Z" is affixed to the gantry head. This frame is simply a clockwise rotation of XYZ through the angle θ about the X axis. A further degree of freedom in the gantry head is introduced by the rotation of the collimator itself. This collimator, lying in the X"Y" plane, can rotate clockwise or counter-clockwise by an angle defined as ψ. A coordinate system X'''Y'''Z''', affixed to the collimator, is defined as a counter-clockwise rotation of the double primed frame through the angle ψ.

We thus have four coordinate systems which are all related to each other through a suitable transformation. The transformation parameters, the angles defining the rotations, are analogous to the Euler angles used in classical mechanics (11), except that we choose our definition for angles θ and ϕ to conform with angles previously defined for the spherical dynamic rotation on our linac. This avoids confusion when implementing the calculations on the treatment machine.

In Fig. 4.1(a), we note that the double and triple primed coordinate systems have their origins translated from the machine isocenter by a fixed vector. This translation vector is not taken into account by the transformations below as the gantry and collimator readout indicators define distances at the isocenter. Our interest is not the actual size of the collimator opening, rather, it is the field size at the isocenter as given by the

appropriate collimator setting. Thus in the calculations below we consider all coordinate frames to have the same origin.

4.2.3 *TRANSFORMATIONS*

To determine the angle of collimator rotation ψ and the length of the longitudinal collimator opening needed to treat a given cylindrical target at a given gantry and couch position, we now find the transformations that take a vector **a'** in the couch coordinate frame (X'Y'Z') to the corresponding vector **a'''** in the fixed collimator frame (X'''Y'''Z'''). The vector **a'** with components (x',y',z') then represents the longitudinal axis of the target. The x''' component corresponds to the longitudinal collimator setting necessary to treat a target of this length. The angle ψ through which the collimator must rotate such that this longitudinal opening aligns itself with the target must also be calculated.

We first derive the transformations taking a vector **a'** in the couch coordinate frame X'Y'Z' to the vector **a'''** in the collimator coordinate frame X'''Y'''Z'''. Referring to Fig. 4.1 for definitions of all angles and axes, we consider the appropriate transformations. The coordinates of the X'''Y'''Z''' frame can be expressed in terms of the coordinates of a vector in the frame stationary with the couch by the use of the following product of matrices:

$$\vec{a}''' = \begin{pmatrix} \cos\psi & \sin\psi & 0 \\ -\sin\psi & \cos\psi & 0 \\ 0 & 0 & 1 \end{pmatrix} \begin{pmatrix} 1 & 0 & 0 \\ 0 & \cos\theta & -\sin\theta \\ 0 & \sin\theta & \cos\theta \end{pmatrix} \begin{pmatrix} \cos\phi & -\sin\phi & 0 \\ \sin\phi & \cos\phi & 0 \\ 0 & 0 & -1 \end{pmatrix} \vec{a}' \,. \qquad (4.1)$$

Explicitly, the longitudinal opening of the collimator x''' as a function of the couch position, gantry position and longitudinal target axis, is given by:

$$x''' = (\cos\psi\cos\phi + \sin\psi\cos\theta\sin\phi)\,x' + (-\cos\psi\sin\phi + \sin\psi\cos\theta\cos\phi)\,y' - (\sin\psi\sin\theta)\,z' \quad (4.2)$$

To find the angle of the collimator rotation ψ, which aligns the field with the target, we examine the longitudinal target vector in the coordinate system of the gantry head, the double primed frame, as given by the vector **a''**. Angle ψ corresponds to the angle that the projection of the vector **a''** makes in the X''Y'' plane. To express x'' and y'' in terms of known quantities, i.e., in terms of the target coordinates in the couch frame, we use the following transformation which takes a vector **a'** with components (x',y',z') in the couch coordinate frame to the corresponding vector **a''** with components (x'',y'',z'') in the gantry coordinate frame :

$$\vec{a}'' = \begin{pmatrix} 1 & 0 & 0 \\ 0 & \cos\theta & -\sin\theta \\ 0 & \sin\theta & \cos\theta \end{pmatrix} \begin{pmatrix} \cos\phi & -\sin\phi & 0 \\ \sin\phi & \cos\phi & 0 \\ 0 & 0 & -1 \end{pmatrix} \vec{a}' \quad . \quad (4.3)$$

The angle of collimator rotation ψ can now be expressed as:

$$\psi = \arctan\left(\frac{(x'\sin\phi + y'\cos\phi)\cos\theta - z'\sin\theta}{x'\cos\phi - y'\sin\phi}\right) \quad . \quad (4.4)$$

For a given couch and gantry setting, we can calculate the collimator longitudinal opening x''' and collimator angle ψ with Equations 4.2 and 4.4, respectively. Note that the length of the vector **a''** projected in the X''Y''

plane is equal to the length of x''', as expected. Thus, given a vector **a'** in the couch coordinate system, which describes the longitudinal orientation and length of a cylindrical target for a fixed couch and gantry setting, the longitudinal collimator opening and the necessary collimator rotation can be calculated such that the length of this opening is always aligned with the target.

Once the collimator has been rotated such that a vector describing its longitudinal opening lies in a plane perpendicular to the target longitudinal vector, the diameter of the target, as seen by the collimator, will remain constant. Thus, as the couch and gantry follow their paths in dynamic rotation, with a 1:2 relationship between the two angles of rotation, the collimator longitudinal opening and rotation will also follow a route determined by the equations derived above. The lateral axis of the collimator (field width), on the other hand, will remain fixed, depending only on the diameter of the target within the couch coordinate system.

Theoretically, the equations governing the four motions involved in cylindrical dynamic rotation allow for continuous movement and a truly dynamic situation. However, unlike the simple 2:1 relationship of gantry and couch angles in the spherical dynamic rotation, the equations for collimator field size adjustment and rotation are considerably more complex, making continuous and simultaneous motion difficult to implement. To circumvent these difficulties, in our experiments we delivered the dose not in a continuous irradiation but with several single stationary beams at specified intervals. The route of the gantry and couch, as derived from dynamic rotation was divided into segments of equal arc, and the corresponding collimator rotation and opening were calculated at each position. Presently, the implementation of the method is thus pseudo-

dynamic, and uses a large number of stationary beams, typically 31 beams with gantry angular increments of 10° and couch angular increments of 5°.

4.3 Materials and methods

The experiments with the cylindrical pseudodynamic rotation were done with the Clinac-18 linear accelerator used for routine radiotherapy and for clinical spherical dynamic rotation radiosurgery with circular beams in our department. The linac is in an excellent mechanical condition with the gantry and couch rotation axes intersecting in a sphere with a diameter on the order of 1 mm. The central axis of the radiation beam as defined by the linac rectangular collimators increases the isocenter sphere to a diameter of 2 mm, which is still within acceptable norms for clinical radiosurgery.

Dose distributions were measured with radiographic film (Kodak XV II), which was placed between the two halves of the polystyrene spherical phantom. The center of the cylindrical target coincided with the center of the spherical phantom which was placed into the linac isocenter. The sphere was fixed to the couch and oriented such that the plane of the film coincided with the desired plane of observation. The planes of observation were the three orthogonal planes through the target volume. The degree of film blackening resulting from an experimental treatment was then related to the dose using the appropriate characteristic curve which gives the relationship between the optical density and dose. Dose distribution data, acquired with the radiographic film, were analysed with a

commercially available radiation field analyser. This equipment is described in greater detail in *Chapter 2*.

Beam data needed in treatment planning consist of the tissue maximum ratios (TMR), off-axis ratios (OAR) and the relative dose factors (RDF) for stationary beams of a given field size. These were measured with standard small size detectors, such as the end-window parallel plate ionization chamber.

For a given cylindrical target irradiation the number of monitor units per each stationary beam was calculated as follows. The total desired dose was divided by the number of stationary beams used to treat the target, typically 31. This dose was then divided by the RDF for the particular collimator setting, by the TMR as measured for that beam at a depth of 9 cm which is the depth from the phantom surface to the isocenter, by the machine calibration factor which converts dose in cGy to machine Monitor Units, by the prescribed isodose line and finally multiplied by 100 to ensure proper units. The resulting Monitor Units were then specific to each field size and ensured an equal contribution of each beam to the total target dose.

A typical treatment calculation for various irradiation parameters is shown in Table 4.1. The target is assumed a cylinder of length 2.0 cm and diameter 0.8 cm, oriented along the X' axis in the couch frame, the dose of 2500 cGy is prescribed to the 90% isodose surface. The penumbra caused by the use of machine collimator jaws results in a 90% beam profile width that is approximately 2/3 of the nominal field size opening. Thus to irradiate a target of 2 cm length and 0.8 cm diameter, the nominal field size settings used in the beam parameter calculations were 3.0 cm and 1.2 cm respectively. The 90% isodose surface will then have the appropriate dimensions to cover the cylindrical target.

Table 4.1 An example of a treatment plan indicating the gantry θ, couch ϕ and collimator ψ angular settings, the longitudinal x''' and lateral y''' collimator openings, the relative dose factors RDF, the tissue maximum ratios TMR and the number of Monitor Units MU for the 31 stationary beams used in cylindrical pseudodynamic rotation. Target length 2.0 cm, target diameter 0.8 cm, target oriented along the X' axis in the couch plane. Total dose of 2500 cGy prescribed to the 90% isodose surface. Nominal collimator openings 3.0 cm length, 1.2 cm width. Machine calibration factor 1.05 cGy/MU.

Gantry angle, θ (deg.)	Couch angle,ϕ (deg.)	Coll. angle, ψ (deg.)	Coll. length, x''' (cm)	Coll. width, y''' (cm)	RDF per beam	TMR per beam	MU per beam
30	75	73	2.6	1.2	0.793	0.812	133
40	70	65	2.4	1.2	0.787	0.811	134
50	65	54	2.2	1.2	0.780	0.810	135
60	60	41	2.0	1.2	0.774	0.810	136
70	55	26	1.9	1.2	0.771	0.809	137
80	50	12	2.0	1.2	0.773	0.810	136
90	45	0	2.1	1.2	0.778	0.810	135
100	40	-8	2.3	1.2	0.785	0.811	134
110	35	-13	2.5	1.2	0.790	0.812	133
120	30	-16	2.7	1.2	0.795	0.812	132
130	25	-17	2.8	1.2	0.798	0.813	132
140	20	-16	2.9	1.2	0.800	0.813	131
150	15	-13	3.0	1.2	0.800	0.813	131
160	10	-9	3.0	1.2	0.801	0.813	131
170	5	-5	3.0	1.2	0.801	0.813	131
180	0	0	3.0	1.2	0.801	0.813	131
190	-5	5	3.0	1.2	0.801	0.813	131
200	-10	9	3.0	1.2	0.801	0.813	131
210	-15	13	3.0	1.2	0.800	0.813	131
220	-20	16	2.9	1.2	0.800	0.813	131
230	-25	17	2.8	1.2	0.798	0.813	132
240	-30	16	2.7	1.2	0.795	0.812	132
250	-35	13	2.5	1.2	0.790	0.812	133
260	-40	8	2.3	1.2	0.785	0.811	134
270	-45	0	2.1	1.2	0.778	0.810	135
280	-50	-12	2.0	1.2	0.773	0.810	136
290	-55	-26	1.9	1.2	0.771	0.809	137
300	-60	-41	2.0	1.2	0.774	0.810	136
310	-65	-54	2.2	1.2	0.780	0.810	135
320	-70	-65	2.4	1.2	0.787	0.811	134
330	-75	-73	2.6	1.2	0.793	0.812	133

4.4 Results and discussion

4.4.1 *SAMPLE TARGET IRRADIATIONS*

To show that the method discussed above indeed produces cylindrical isodose distributions, we irradiated two sample targets in the spherical phantom. Both targets were cylinders of length 2 cm and width 0.8 cm, centered in the spherical phantom. The first cylinder had a simple longitudinal orientation along the X' axis of the couch coordinate frame, while the second had an arbitrary orientation of its longitudinal axis.

A schematic representation of the two cylindrical targets is shown in Fig. 4.2. Part (a) shows the orientation of the first target in the couch plane, along the couch X' axis. Part (b) represents the second target, a cylinder rotated by 45° in the X'Y' plane and by 45° to the Z' axis. Finally, part (c) shows three orthogonal planes in which the dose distributions were measured for both targets. For the target lying along the X' axis, plane 1 corresponds to the transverse plane, plane 2 is the sagittal plane and plane 3 is the coronal plane. For the second target, the 3 planes of observation do not have such anatomical counterparts.

For the first target, the irradiated films and isodose distributions, obtained with the cylindrical pseudodynamic rotation, are shown in Fig. 4.3 for the transverse, coronal and sagittal planes. The left side shows the exposed films, the right side the corresponding isodose distributions (90%, 50%, and 10% isodose surfaces) measured with the 2-D densitometer. The 90% isodose surface, which would be used for the dose prescription, is clearly of a cylindrical shape and even the lower level isodose surfaces, such as the 50% isodose surface, are cylindrical. The 10% isodose surface,

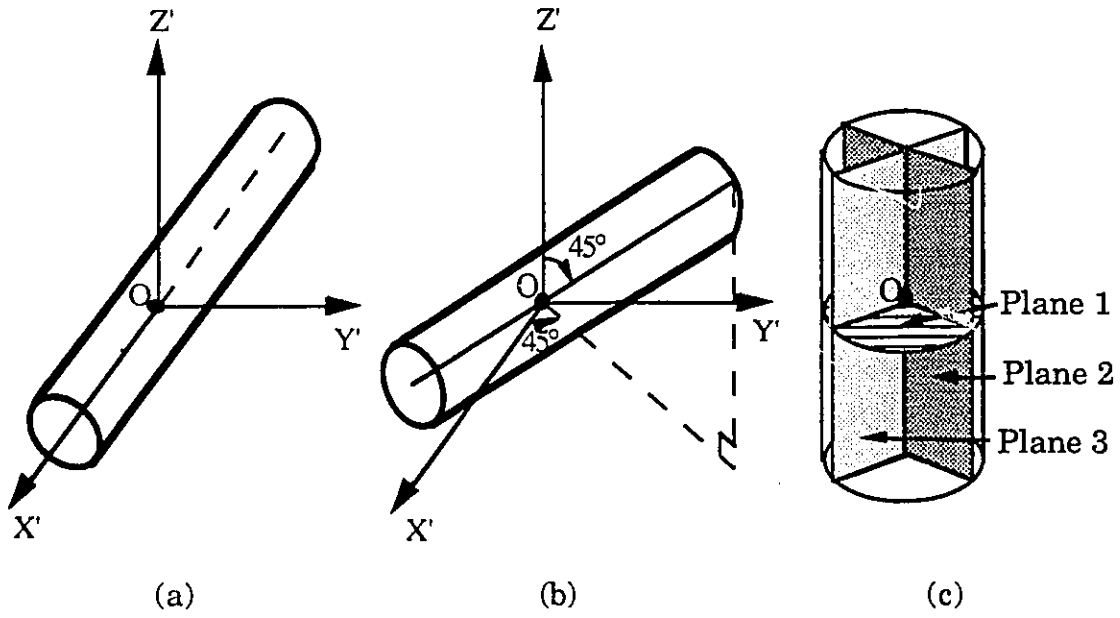

Figure 4.2 A schematic representation of two cylindrical targets placed at the center of the spherical head phantom with a diameter of 18 cm. Part (a) shows the orientation of the first target in the couch plane, along the couch X' axis. Part (b) represents the second target, a cylinder rotated by 45° in the X'Y' plane and by 45° to the Z' axis. Part (c) shows the three orthogonal planes of observation through the cylinder. For the first target these planes correspond to the transverse, sagittal and coronal planes, respectively. The isodose distributions were measured in the three orthogonal planes. The linac isocenter is represented by O.

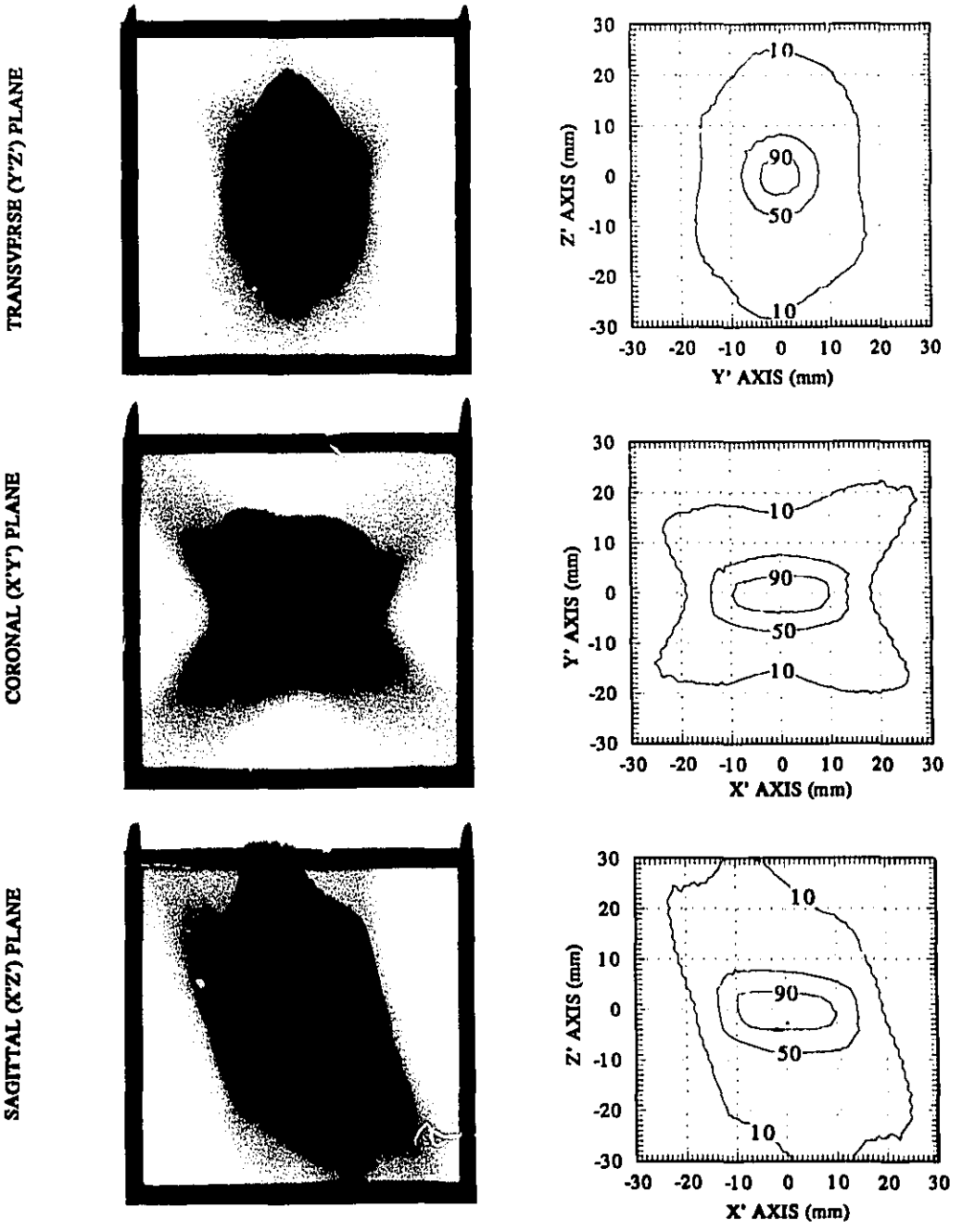

Figure 4.3 Results of film irradiations with cylindrical pseudodynamic rotation for a 2 cm long and 0.8 cm diameter cylinder with the longitudinal axis along X'. The irradiated films in the three orthogonal planes are shown on the left side, the corresponding isodose distributions on the right.

on the other hand, shows the behavior typical for the low level distributions obtained with dynamic rotation. The 90% isodose surfaces in the sagittal and coronal planes show cylindrical longitudinal cross sections (rectangular shape) of width 0.8 cm and length 2 cm, while the transverse plane shows a circular lateral cross section with a diameter of 0.8 cm, indicating that the cylindrical target has been irradiated as intended.

The second target which has essentially an arbitrary orientation within the sphere, represents a cylinder rotated by 45° in the X'Y' plane and by 45° to the Z' axis. In Fig. 4.4 we show the resulting irradiated films on the left and the isodose distributions (90%, 50%, and 10% isodose surfaces) on the right measured in the three orthogonal planes shown in Fig. 4.2(c). The longitudinal rectangular cross sections through planes 2 and 3 show the 90% isodose surfaces of length 2 cm and width 0.8 cm, while plane 1 gives the circular lateral cross section with a 90% isodose surface of 0.8 cm diameter, resulting in the desired dose distribution. The 50% isodose surfaces are also cylindrical, but the lower level isodose surfaces are progressively more anisotropic, as shown by the 10% isodose surface.

Figures 4.3 and 4.4 show a sharp and almost constant dose fall-off of 5 mm from the 90% to the 50% isodose surfaces, indicating that the 2 cm high and 0.8 cm diameter cylindrical target in the spherical head phantom was irradiated according to the norms prescribed for radiosurgery.

4.3.2 *CYLINDRICAL VS SPHERICAL DYNAMIC ROTATION*

To show the actual dose savings resulting from the cylindrical pseudodynamic rotation as compared to spherical dynamic rotation, we

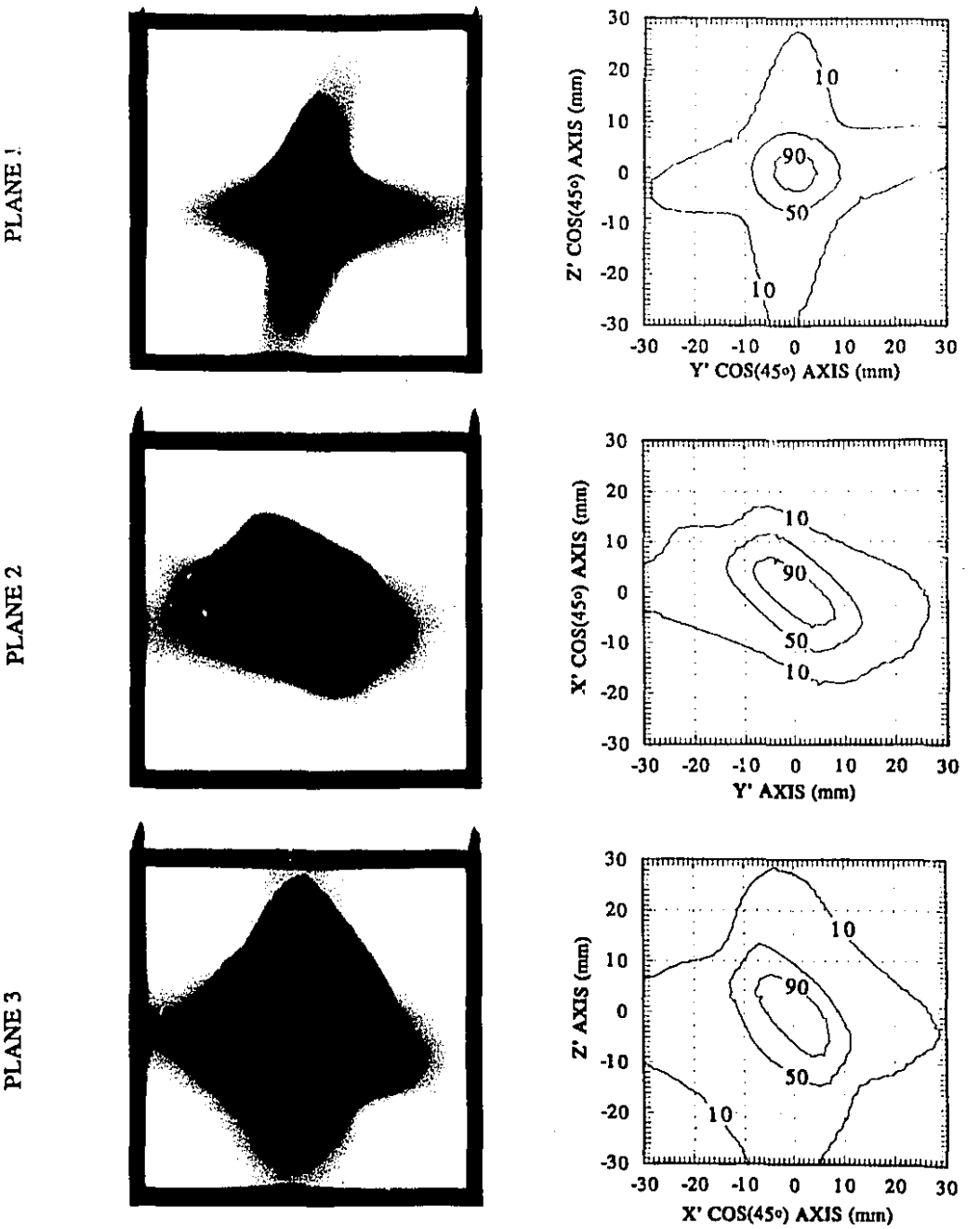

Figure 4.4 Results of film irradiations with cylindrical pseudodynamic rotation for a 2 cm long and 0.8 cm diameter cylinder with the longitudinal axis parallel to (1.5,1.5,2.1) (as shown in Fig. 4.2(b)). The irradiated films in the three orthogonal planes are shown on the left side, the corresponding isodose distributions on the right side.

also irradiated the target of Fig. 4.3 with a 2 cm diameter circular collimator and compare the resulting dose distribution with that obtained for the cylindrical irradiation of the same target. The isodose distributions are shown in Fig. 4.5 for both the spherical (dashed lines) and cylindrical (solid lines) method. As seen in the coronal and sagittal planes, the 90% isodose surfaces for both methods appropriately cover the same target length of 2 cm. However, the width of the 90% isodose surface is, of course, considerably larger for the spherical compared to the cylindrical irradiation. This effect is also seen clearly in the transverse plane which shows circular 90% isodose surfaces for the spherical and cylindrical irradiations with diameters of 2 cm and 0.8 cm, respectively.

The volume of the cylindrical target is ~1 cm^3, while the volume of the corresponding sphere is ~4 cm^3. Thus, when a cylindrical target with a height 2 cm and diameter 0.8 cm is irradiated with the spherical dynamic rotation, 3 cm^3 of healthy tissue in addition to the 1 cm^3 of targeted tissue is encompassed by the resulting 90% isodose surface.

In general, because the area of the circular beam is larger than that of the rectangular one, the volume enclosed by the 90% isodose surface for the spherical dynamic rotation is considerably larger than that enclosed by the same percentage isodose surface for the cylindrical pseudodynamic rotation, i.e., for cylindrical targets a substantially larger amount of healthy tissue will be treated with the spherical dynamic rotation than with the cylindrical pseudodynamic rotation.

An additional advantage of the cylindrical pseudodynamic rotation is the sharper dose fall-off outside the target. As shown in Fig. 4.5 for a 2 cm long and 0.8 cm diameter cylindrical target, the dose fall-off characteristics

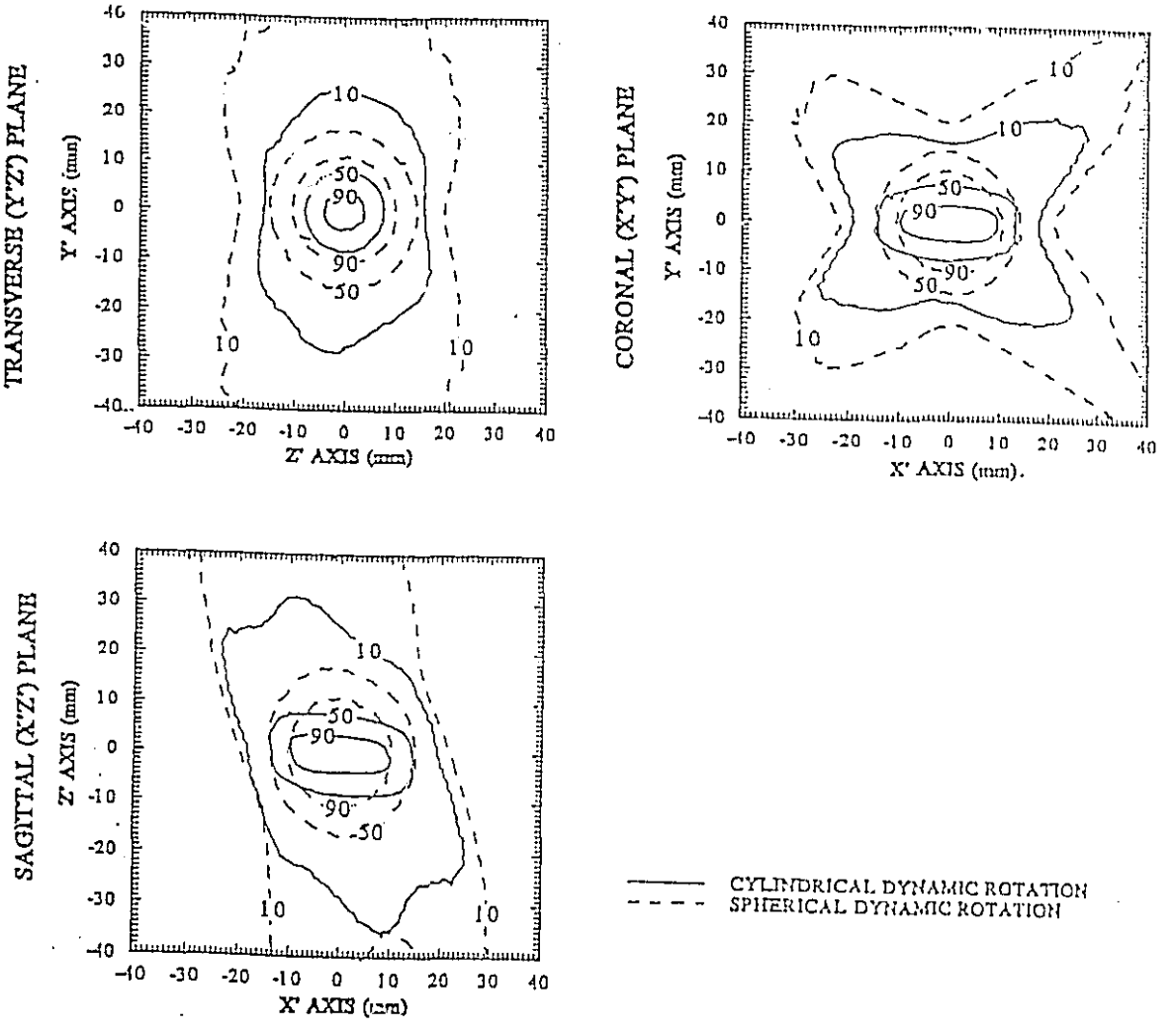

Figure 4.5 Comparison of isodose distributions for the spherical (dashed lines) and cylindrical (solid lines) dynamic rotations. The 20 mm diameter collimator was used with spherical dynamic rotation, while the cylindrical dynamic rotation irradiated a 2 cm long and 0.8 cm diameter cylinder oriented along the X' axis. The 90%, 50% and 10% isodose lines,measured in the three orthogonal planes, are shown. The isodoses for the cylindrical dynamic rotation were also shown in Fig. 4.3.

outside the 90% isodose surface are actually improved in the cylindrical pseudo-dynamic rotation when compared to the spherical dynamic rotation. For example, the 10% isodose surface obtained for the two cylindrical irradiations contains a considerably smaller volume of tissue than does the 10% surface obtained for the spherical irradiation.

In Fig. 4.6 we plot the maximum and minimum distances for the dose to decrease from 90% to 50%, 20% and 10% for isodose distributions corresponding to the three sample irradiations presented: the cylindrical isodose distribution oriented along the X' axis of Fig. 4.3, the cylindrical isodose distribution with arbitrary longitudinal axis orientation of Fig. 4.4, and the spherical isodose distribution of Fig. 4.5. The sharpest dose fall-offs are essentially identical for the three irradiations, the shallowest fall-offs, on the other hand, are worse for the spherical irradiation compared to the two cylindrical irradiations. Since the dose fall-offs for spherical dynamic rotation were shown acceptable for radiosurgery before (12), we conclude that the dose fall-offs resulting from cylindrical pseudodynamic rotation are also adequate for use in clinical radiosurgery.

4.5 Conclusions

The radiosurgical method of cylindrical pseudodynamic rotation is based on the concept of the spherical dynamic rotation but uses two more degrees of freedom: variable rectangular field size and collimator rotation, and delivers the dose through a succession of stationary beams. With the appropriate choice of treatment parameters, the method results in cylindrical isodose distributions, which can cover cylindrical targets of

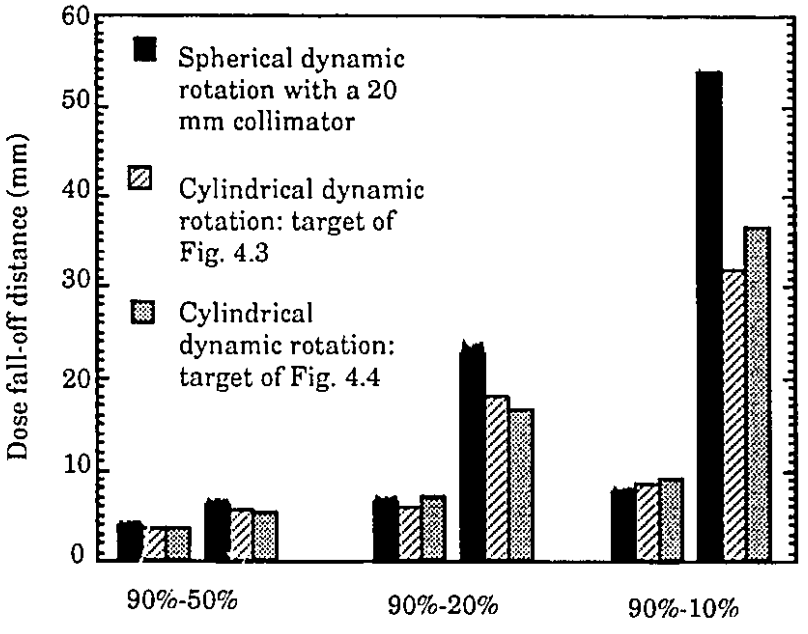

Figure 4.6 Minimum and maximum distances for the dose to decrease from 90% to 50%, 20%, and 10% for two examples of isodose surfaces in the cylindrical dynamic rotation, described in Figures 4.3 and 4.4, and one example of isodose surfaces in the spherical dynamic rotation, described in Fig. 4.5.

arbitrary orientation within the patient's head. Transformation matrices relating vectors in the coordinate system of the couch to that of the collimator are used to develop equations for the calculation of collimator opening and rotation as a function of gantry and couch angles, as well as the orientation and length of the target longitudinal axis orientation in the couch coordinate frame.

In situations where a clinical target is better approximated by a cylinder than a sphere, cylindrical pseudodynamic rotation will result in considerable dose savings to healthy tissue immediately surrounding the target. The dose fall-offs obtained with the cylindrical pseudodynamic rotation from the target defining isodose surface (90%) to lower isodose surfaces are actually sharper than those obtained in spherical dynamic rotation. Furthermore, as we are able to shape the high level isodose surfaces, dose inhomogeneities within the target volume are minimized. Therefore, the method of the cylindrical pseudodynamic rotation could be developed into a viable technique for the treatment of elongated radiosurgical targets. Furthermore, the pseudodynamic method described here could be extended with the use of miniature multileaf collimators to treat target volumes of even more irregular shapes. These miniature collimators resemble the multileaf collimators used in large field radiotherapy, but have leaf widths on the order of 1 mm, making them useful for field sizes up to 4x4 cm^2.

4.6 References

1. D.D. Leavitt, F.A. Gibbs, M.P. Heilbrun, J.H. Moeller and G.A. Takach, *Dynamic field shaping to optimize stereotactic radiosurgery*, Int. J. Radiat. Oncol. Biol. Phys. **21**: 1247-1255, 1991.
2. N. Maleki, W. Lutz and K. DeWyngaert, *Parameter specification for two-isocenter-technique in radiosurgery* (abstract), Med. Phys. **16**: 461, 1989.
3. J.C. Flickinger, L.D. Lunsford, A. Wu, A.H. Maitz, A.M. Kalend, *Treatment planning for gamma knife radiosurgery with multiple isocenters*, Int. J. Radiat. Oncol. Biol. Phys. **18**: 1495-1501, 1990.
4. J.C. Flickinger, A. Maitz, A. Kalend, L.D. Lunsford and A. Wu, *Treatment volume shaping with selective beam blocking using the Leksell gamma unit*, Int. J. Radiat. Oncol. Biol. Phys. **19**: 783-789, 1990.
5. G. Luxton and G. Jozsef, *Dosimetric considerations in linac radiosurgery treatment planning of off-center and elongated targets* (abstract), Int. J. Radiat. Oncol. Biol. Phys. **19** Suppl. 1: 262, 1990.
6. C. Serago, A. Lewin, P. Houdek, A. Abitol, S. Gonzales-Arias, V. Pisciotti and J. Schwade, *Improved linac dose distributions for radiosurgery with irregularly shaped fields*, Int. J. Radiat. Oncol. Biol. Phys. **21**: 1321-1325, 1991.
7. P.H. McGinley, E.K. Butker, I.R. Crocker and R. Aiken, *An adjustable collimator for stereotactic radiosurgery*, Phys. Med. Biol. **37**: 413-419, 1992.
8. K.E. Sixel, *Physical parameters of narrow photon beams in radiosurgery*, M.Sc. Thesis, McGill University, Montréal, 1990.

9. K.E. Sixel and E.B. Podgorsak, *Cylindrical dose distributions in dynamic rotation radiosurgery*, (abstract) Med. Phys. **18**:621, 1991.

10. K.E. Sixel, E.B. Podgorsak and L. Souhami, *Cylindrical dose distributions in pseudodynamic rotation radiosurgery: an experimental study*, Med. Phys. **20**: 163-170, 1993.

11. H. Goldstein, *Classical Mechanics*, 2nd edition, Addison-Wesley Publishing Co. Inc. Reading Massachusetts, 1980, pp. 132-148.

12. E.B. Podgorsak, G.B. Pike, A. Olivier, M. Pla and L. Souhami, *Radiosurgery with high energy photon beams: a comparison among techniques*, Int. J. Radiat. Oncol. Biol. Phys. **16**: 857-865, 1989.

CHAPTER 5

PHYSICAL PARAMETERS OF RADIOSURGICAL X-RAY BEAMS

5.1 Introduction

The development of linear accelerator-based radiosurgical techniques over the past few years has stimulated much physics oriented research in the dosimetry of narrow megavoltage x-ray beams (1-4). The small diameters of radiosurgical beams place restrictions on the size of detectors used for measurement of beam parameters. The detectors used in the measurement of conventional radiotherapy beams are generally too large to measure accurately the radiosurgical beam data. Also, the narrow radiosurgical beams are affected by the problem of electronic equilibrium, which plays a role at media interfaces and near the beam edge (5). For high energy beams, the recoil electrons have a substantial lateral range in tissue, thereby increasing the penumbra beyond the geometrical beam spread, implying that for small field sizes the entire beam profile may be characterized by the penumbra region.

The parameters needed for radiosurgical treatment planning consist of percentage depth dose curves, beam profiles and various scatter factors. In this Chapter, the data resulting from the measurement of these parameters at beam energies of 6 MV, 10 MV and 18 MV, and field diameters in the range from 10 mm to 30 mm are presented. Analysis of the data shows a relationship between the depth of dose maximum, d_{max}, and field size for different beam energies (6,7,8). Frequently, lesions treated with radiosurgery are within a few cm of the patient's skin (i.e., at depths smaller or comparable to d_{max}) and the treatment planning software must account for doses at these shallow depths. Subsequently, the dependence of d_{max} on field size and beam energy is discussed in greater detail.

5.2 Beam data

5.2.1 *BEAM PROFILES*

A beam profile gives the distribution of dose along the cross-section of a radiation beam at a particular depth in a phantom. The doses are normalized to the dose on the central beam axis and are usually given as a percentage of this maximum dose. These percentages are referred to as off-axis ratios (OAR) and are plotted as a function of distance from the central axis. Measurements were made to determine the beam width as a function of depth in phantom, beam diameter and beam energy. This data is then used in the calculation of dose distributions for radiosurgery.

Since the radiosurgical beams are of very small cross-sections, the techniques used in the measurement of beam parameters for standard radiotherapy beams are not necessarily adequate for the parameter measurements of radiosurgical beams. This is a particularly important consideration in the measurement of beam profiles, given their steep dose gradients. In has been shown that the small sensitive volume of the RFA semiconductor detector discussed in *Chapter 2* gives these detectors a spatial resolution appropriate for beam profile measurements (6).

Figure 5.1 shows typical examples of off-axis ratio measurements for three beam energies, three depths in phantom and two beam diameters. The profiles of the 10 mm and 30 mm diameter beams at depths of 25 mm, 105 mm and 185 mm in a water phantom are plotted in part (a) for the 6 MV beam, in part (b) for the 10 MV beam and in part (c) for the 18 MV x-ray beam. These measurements were made with a stationary x-ray beam in a water phantom at a source-surface distance (SSD) of 100 cm. The

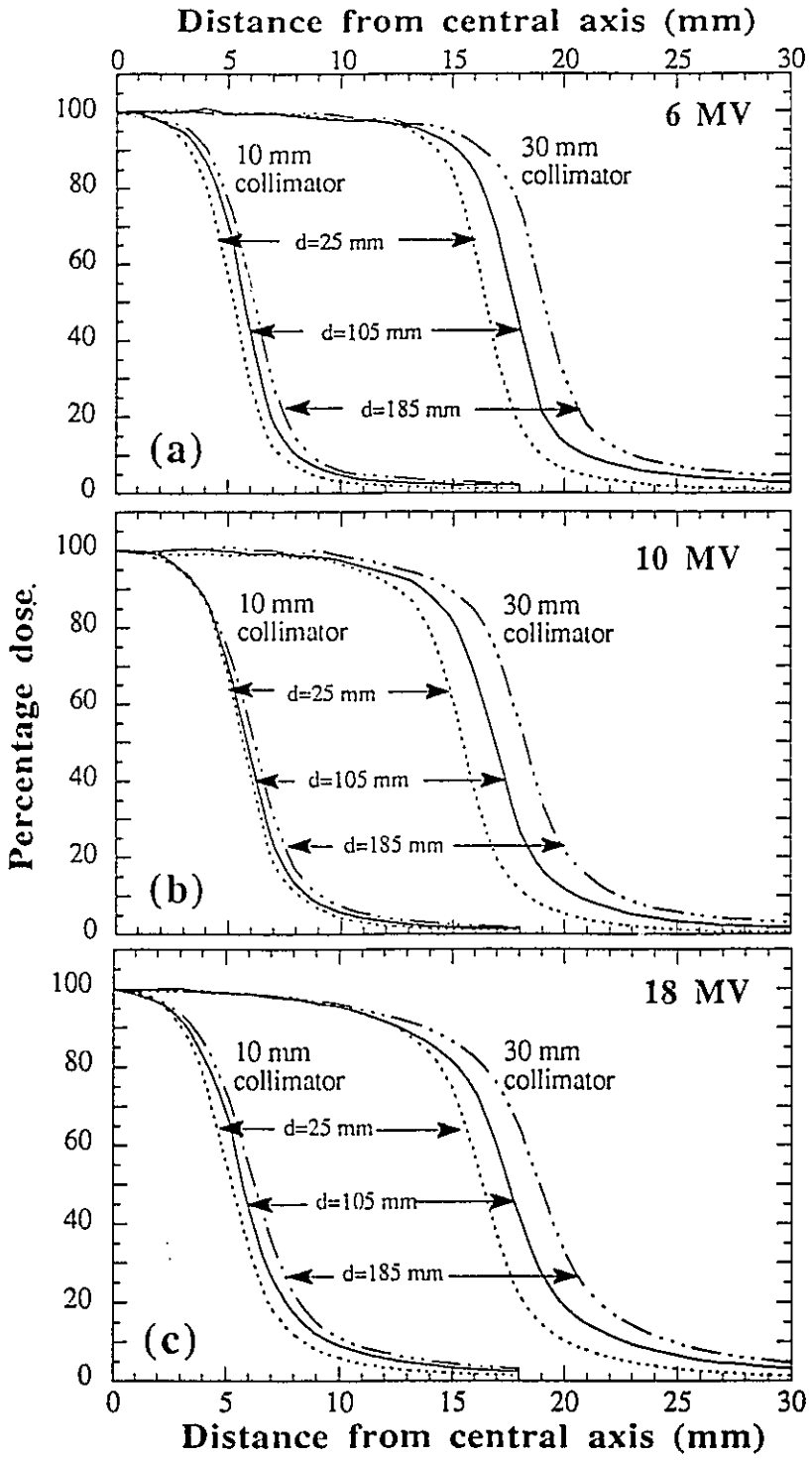

Figure 5.1 Beam profiles of the 10 mm and 30 mm diameter collimators at 25 mm, 105 mm and 185 mm depths for (a) 6 MV, (b) 10 MV and (c) 18 MV x-ray beams. The profiles were measured with an SSD of 100 cm.

collimators were chosen as typical examples, with the profiles of intermediate field sizes falling between the values plotted.

For a given beam energy, the physical collimator size and the geometrical beam divergence (the beam is considered to originate from a point source), are the main factors governing the shape of the beam profiles. The fall-offs from 90% to 10% of the central axis dose for a particular collimator and beam energy are found to be essentially parallel for the three depths plotted. Furthermore, the fall-off slopes are similar for the two different collimators. Thus for small beam diameters the proportion of side scatter does not seem to change with increasing field size or increasing depth.

Comparing beam profiles as a function of energy shows that a given profile (for a particular beam diameter and depth) changes slightly with beam energy. As energy increases, the amount of lateral scatter also increases. For example, the radial distance from the central axis of the 10% value of the 10 mm collimator profile at a depth of 185 mm is 8.7 mm for the 6 MV beam, 9.1 mm for the 10 MV beam and 10.4 mm for the 18 MV beam. These differences are small, and do not affect radiosurgical dose distributions, which are almost identical for 6 MV and 10 MV beams. However, lateral scatter and consequently beam penumbra sharpness, among other considerations, can be used to limit the maximum beam energy which is appropriate for radiosurgery.

Most radiosurgical techniques, including the dynamic rotation used at McGill university, are isocentric requiring beam data given for a constant source-axis distance (SAD) of 100 cm rather than a constant SSD. In practice, beam data is usually measured with an SSD set-up as this is the more simple physical situation. The treatment planning program used

to calculate dose distributions must then convert the measured SSD data to SAD data. In Fig. 5.2 we present beam profiles measured with an SAD set-up for comparison to the SSD profiles of Fig. 5.1. Shown are the profiles of two 10 MV beams with field diameters of 10 mm and 30 mm measured with the RFA semiconductor at an SAD of 100 cm and depths of 25 mm, 105 mm and 185 mm. The SAD data clearly indicate that lateral scatter is independent of depth in phantom since there is very little difference between the profiles of a given collimator measured at the various depths.

5.2.2 *PERCENTAGE DEPTH DOSES*

In radiotherapy, the dose deposited by a radiation beam as it penetrates through a medium is described by a percentage depth dose curve (PDD). This curve is measured on the beam central axis and gives the relative dose deposited by the beam as a function of depth in the medium. The dose is normalized to its maximum value occuring at the depth of dose maximum and given as a percentage. Percentage depth doses beyond d_{max} were measured with the semiconductor detector and the RFA water phantom system described in *Chapter 2* at an SSD of 100 cm, to a depth of 20 cm. This depth is deemed sufficient, as radiosurgery is performed on the brain with a maximum separation of less than 20 cm.

The build-up region of a photon beam is defined as the region extending from the surface of the medium to d_{max}. The dose gradients are generally very steep here, as the depth of dose maximum is reached in a few cm, depending on beam energy. The end-window parallel plate chamber with its thin chamber wall and small plate separation was most

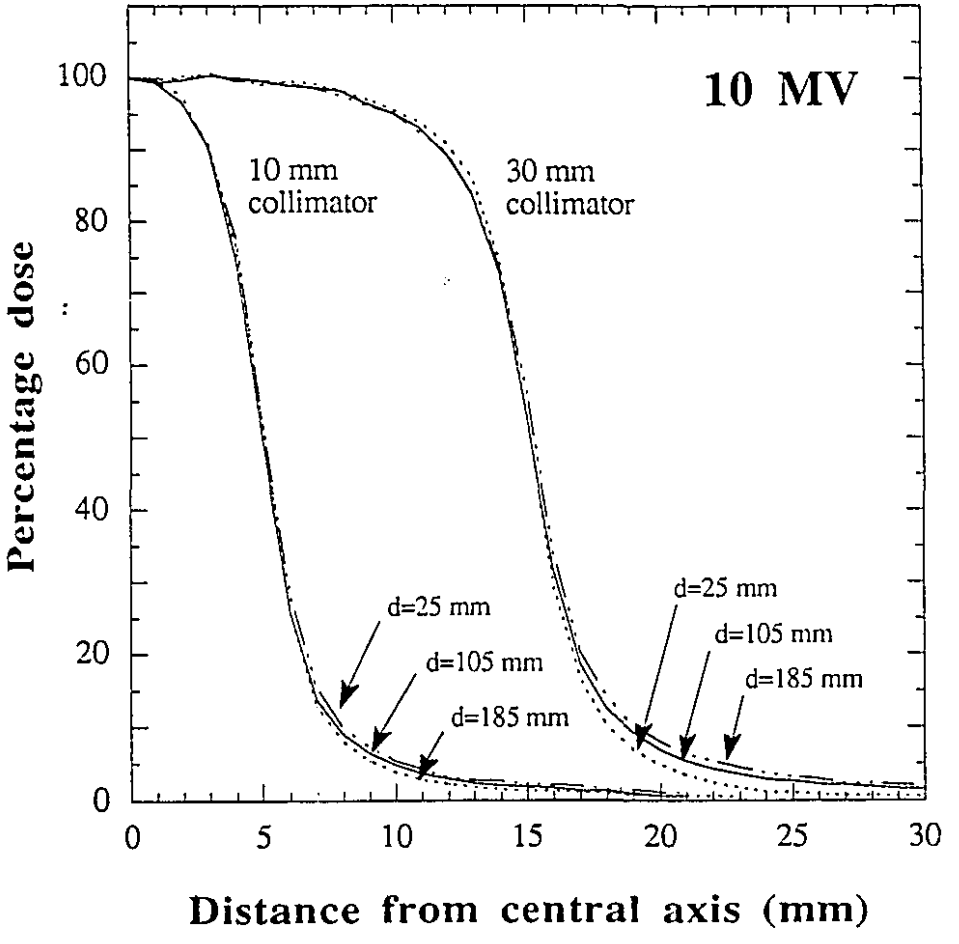

Figure 5.2 10 MV beam profiles of the 10 mm and 30 mm diameter collimators measured with an SAD of 100 cm at depths of 25 mm, 105 mm and 185 mm.

suitable for build-up region measurements and was used for this purpose in conjunction with a polystyrene phantom.

In Fig. 5.3 the percentage depth doses for the 10 mm and the 30 mm diameter collimators are plotted in part (a) for the 6 MV beam, in part (b) for the 10 MV beam, and in part (c) for the 18 MV beam. For a given beam energy, the 10 mm PDD curve falls off at a steeper rate than the 30 mm PDD curve. This is due to an increase in phantom scatter caused by the greater volume of medium irradiated by the larger field size (9). We also note that for a given beam energy, the depth of maximum dose is smaller for the small field size than for the larger field size. We will return to this point in *Section 5.3* below. The surface dose, on the other hand, does not seem to change with field size, amounting to 7% for the 6 MV beam, 8% for the 10 MV beam and 14% for the 18 MV beam, regardless of field diameter.

Figure 5.3 also shows that the beams become more penetrating with increasing energy, as d_{max} is near 15 mm at 6 MV, near 20 mm at 10 MV and near 30 mm at 18 MV. Thus the build-up region of higher energy beams is a much greater fraction of the PDD curve used in radiosurgery. Furthermore, the dose fall-off from d_{max} is most gradual for the 18 MV beam and most rapid for the 6 MV beam. These characteristics must be considered when choosing beam energy for clinical radiosurgery.

5.2.3 *COLLIMATOR AND TOTAL SCATTER CORRECTION FACTORS*

In general, the dose measured at any depth in phantom along the central axis of a radiation beam consists of both primary and secondary

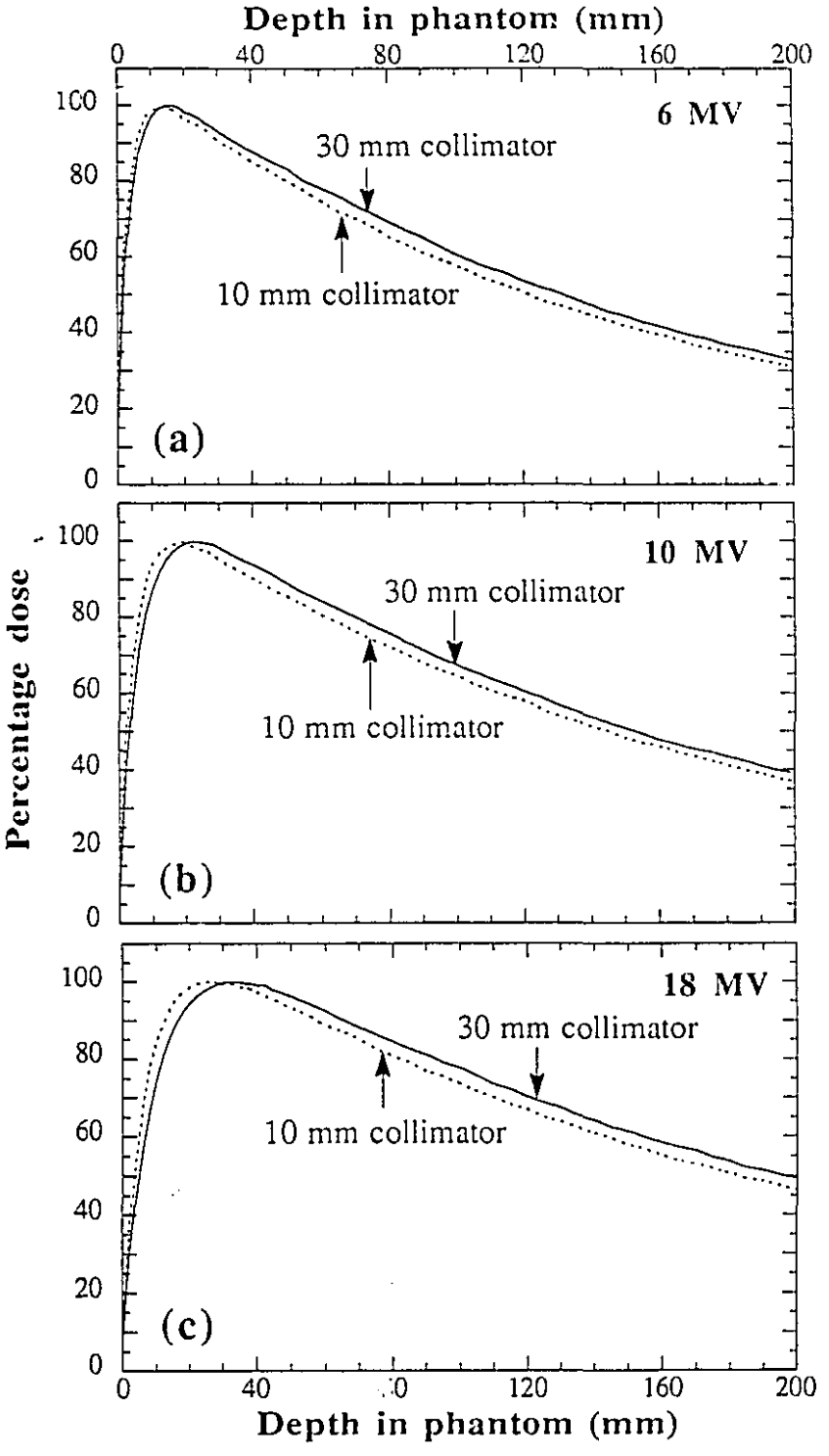

Figure 5.3 Percentage depth doses of the 10 mm and 30 mm diameter collimators for (a) 6 MV, (b) 10 MV and (c) 18 MV x-ray beams.

dose. The primary dose is determined by the photon fluence of the primary beam, which can be considered as originating from a point source, and is field size independent. The scattered dose, on the other hand, is proportional to the field size and thus to the volume of irradiated medium. For a fixed beam energy, a change in measured beam parameters is a result of a change in the scatter dose.

The collimator correction factor (S_c) is defined as the ratio of the dose in air at a distance of SSD plus d_{max} for a given field size to the dose in air at the same distance for a 10×10 cm^2 reference field (10). It describes the machine head scatter dependence on field size. It was measured in air with the semiconductor detector and brass build-up caps of appropriate thicknesses. The total scatter correction factor (S_t) is defined as the ratio of the dose measured in phantom at d_{max} for a given field size to the dose in phantom at d_{max} for a 10×10 cm^2 reference field. The total scatter correction factor thus accounts for two scatter components: the scatter originating in the machine head as well as the scatter originating in the phantom. Clearly, it is not possible to differentiate between the two scatter sources by simple measurements in phantom. However, the phantom scatter can be calculated from the ratio of the measured quantities S_c to S_t for a given field size.

Collimator and total scatter correction factors are tabulated for the three energies and five radiosurgical beam diameters in Table 5.1. For a given photon energy, the S_c factors are constant in the field diameter range from 15 mm to 30 mm. A smaller field size could not completely cover the detector and brass build-up cap and the value for the 10 mm diameter collimator was thus extrapolated from the measurements at larger field sizes. On the other hand, the S_t factors show a considerable field size

Table 5.1 Collimator scatter correction factors (S_c) and total scatter correction factors (S_t) for radiosurgical beams of various diameters and x-ray beam energies, normalized to 1.0 for the standard 10x10 cm^2 field.

Field size (mm)	Collimator scatter correction factor			Total scatter correction factor		
	6 MV	10 MV	18 MV	6 MV	10 MV	18 MV
10	0.95	0.94	0.93	0.85	0.73	0.70
15	0.95	0.94	0.93	0.89	0.81	0.79
20	0.95	0.94	0.93	0.91	0.86	0.85
25	0.95	0.94	0.93	0.92	0.90	0.87
30	0.95	0.94	0.93	0.93	0.91	0.90
100x100*	1.00	1.00	1.00	1.00	1.00	1.00

* 100x100 mm^2 standard radiotherapy field

dependence, increasing with increasing field size. Consequently, the phantom scatter correction factor also increases with increasing field size.

Table 5.1 also shows the energy dependence of S_c and S_t for a fixed field size. Both factors decrease with increasing beam energy. Since the scatter factors are ratios compared to a standard field size, the larger deviation from 1.0 at higher energies indicates that scatter plays a greater role in determining beam parameters as the energy of the photon beam increases.

5.3 Build-up region of radiosurgical beams

5.3.1 *DEPTH OF DOSE MAXIMUM AS A FUNCTION OF FIELD SIZE AND BEAM ENERGY*

It is seen in Fig. 5.3 that the dose distribution in the build-up region of radiosurgical beams changes with beam diameter and energy. This is further emphasized in Fig. 5.4 where the percentage depth doses of the build-up regions of the 10 mm and 30 mm diameter collimators are replotted from the phantom surface to a depth of 50 mm for the 6 MV beam in part (a), the 10 MV beam in part (b) and the 18 MV beam in part (c). Clearly, d_{max} increases with field diameter in the range from 10 mm to 30 mm. This is in contrast to the behaviour of standard radiotherapy beams for which d_{max} decreases with increasing field size (11).

The depths of dose maxima for our radiosurgical beams increase with increasing beam energy and field size and are plotted in Fig. 5.5 as a function of field diameter for the three photon beam energies. In the beam

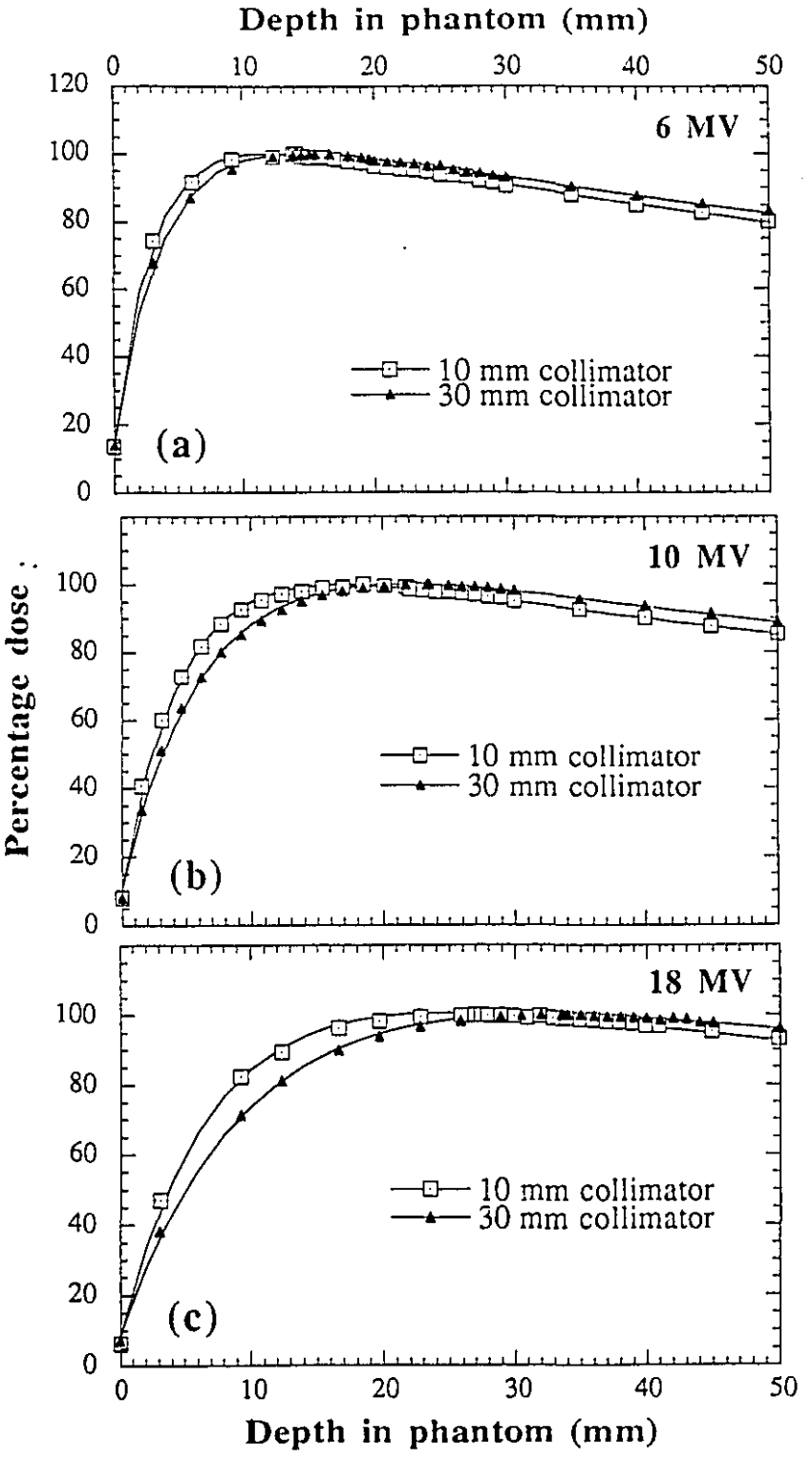

Figure 5.4 Build-up region percentage depth doses of 10 mm and 30 mm diameter circular fields for (a) 6 MV, (b) 10 MV and (c) 18 MV x-ray beams.

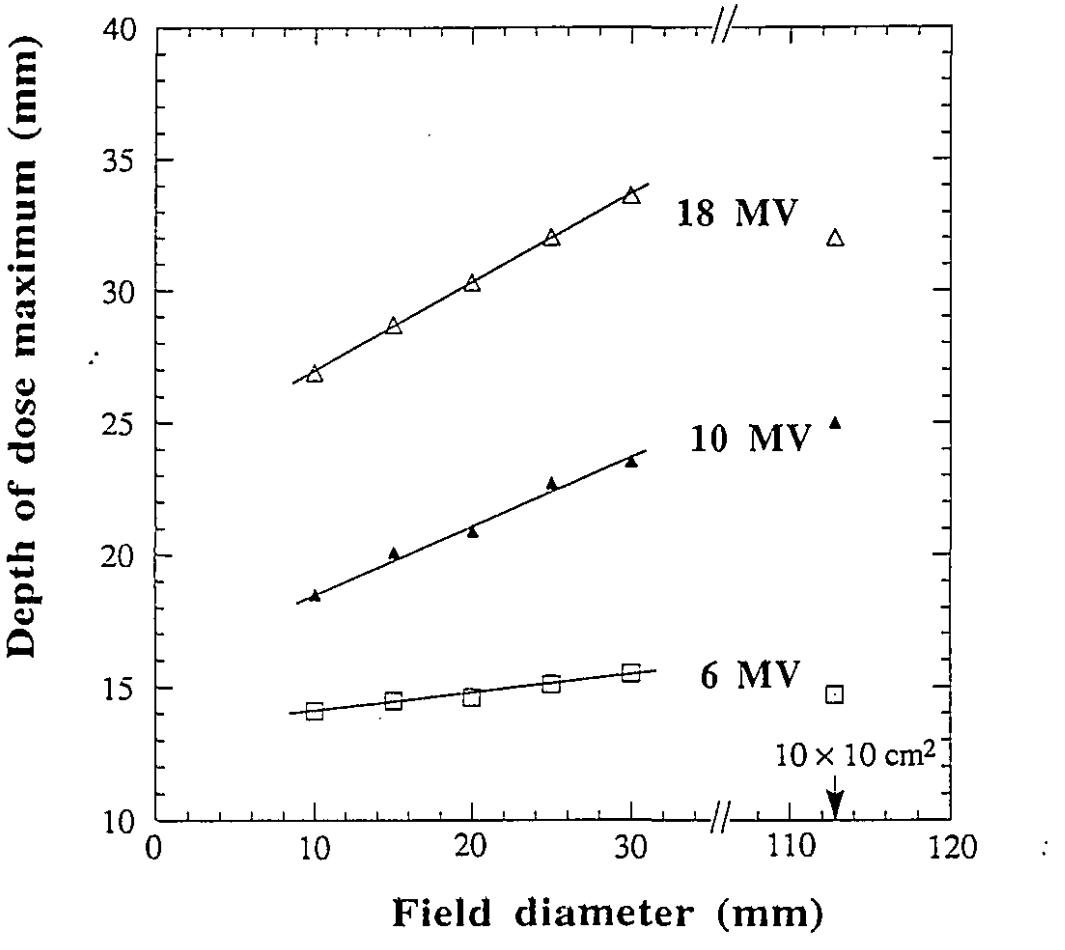

Figure 5.5 Depth of dose maximum *vs* field diameter for the 6 MV, 10 MV and 18 MV x-ray beams. Data for the 10x10 cm^2 fields are also shown.

diameter range from 10 mm to 30 mm, d_{max} varies by only 1.5 mm for the 6 MV beam, but by as much as 6 mm and 7 mm for the 10 MV and 18 MV beams, respectively. The data for standard 10x10 cm^2 fields are shown for comparison.

In Table 5.1, the total scatter and collimator scatter correction factors are given. For a given photon beam energy, S_c is found to be constant within experimental errors in the field diameter range measured (15 mm to 30 mm). However, the total scatter correction factor is found to increase with increasing field size. Thus, while the collimator scatter remains constant, the phantom scatter increases with increasing field size. This data indicates that the changes in d_{max} are a result of events occuring in the phantom and not because of a change in scatter conditions in the linac head.

5.3.2 *MONTE CARLO SIMULATIONS OF THE BUILD-UP REGION*

Monte Carlo simulation was used to study the dose deposition patterns in the phantom as a function of depth and field size. The Monte Carlo data were calculated with the EGS4 code using a uscr-written interface and the *PRESTA* algorithm as described in *Chapter 3*. Incident particles were sampled from a 10 MV photon beam spectrum available in the literature (12). Originating from a point source, the particles were transported through a semi-infinite water phantom. Cut-off energies were chosen to be 0.521 MeV for electrons (total energy) and 0.001 MeV for photons. Primary and scattered doses were scored along the beam central

axis as a function of depth for different field sizes. Primary dose was defined as any energy deposited by an electron or positron generated in a first photon interaction while scattered dose was the energy deposited by electrons generated by the second or subsequent photon scatter events. The size of the scoring voxels depended on the field size at isocenter and varied in cross-sectional area from 5×5 mm^2 to 10×10 mm^2. For all field sizes, the depth of the voxels was 2 mm. To obtain statistical uncertainties within 2%, 1×10^6 to 2×10^6 histories were run in 10 batches. The number of histories was varied to maintain an approximately constant initial photon flux.

Figure 5.6 shows the comparison between Monte Carlo calculation and measurement in the build-up region of the 10 MV beam. Parts (a) and (b) are for collimator diameters of 10 mm and 30 mm, respectively. The data points (open circles) taken from Fig. 5.4(b) represent the total measured dose normalized to 100 at d_{max}. The solid circles, shown with corresponding error bars, represent the Monte Carlo calculation of total dose on the central axis. The graphs indicate that there is good agreement between measurement and simulation. Most measured data points fall within the error bars of the total dose of the Monte Carlo simulation, serving as a benchmark for the reliability of the calculated dose values. The agreement between Monte Carlo data and measured data further supports the conclusion drawn from the collimator scatter factors, namely, that the shift in d_{max} is independent of the scatter from the machine head. The Monte Carlo simulation began on the phantom surface and did not consider scatter originating outside the phantom surface.

The total dose of Fig. 5.6 is divided into two components and plotted in Fig. 5.7 for the 10 mm collimator in part (a) and the 30 mm collimator in part (b). One component of the total dose represents the primary dose

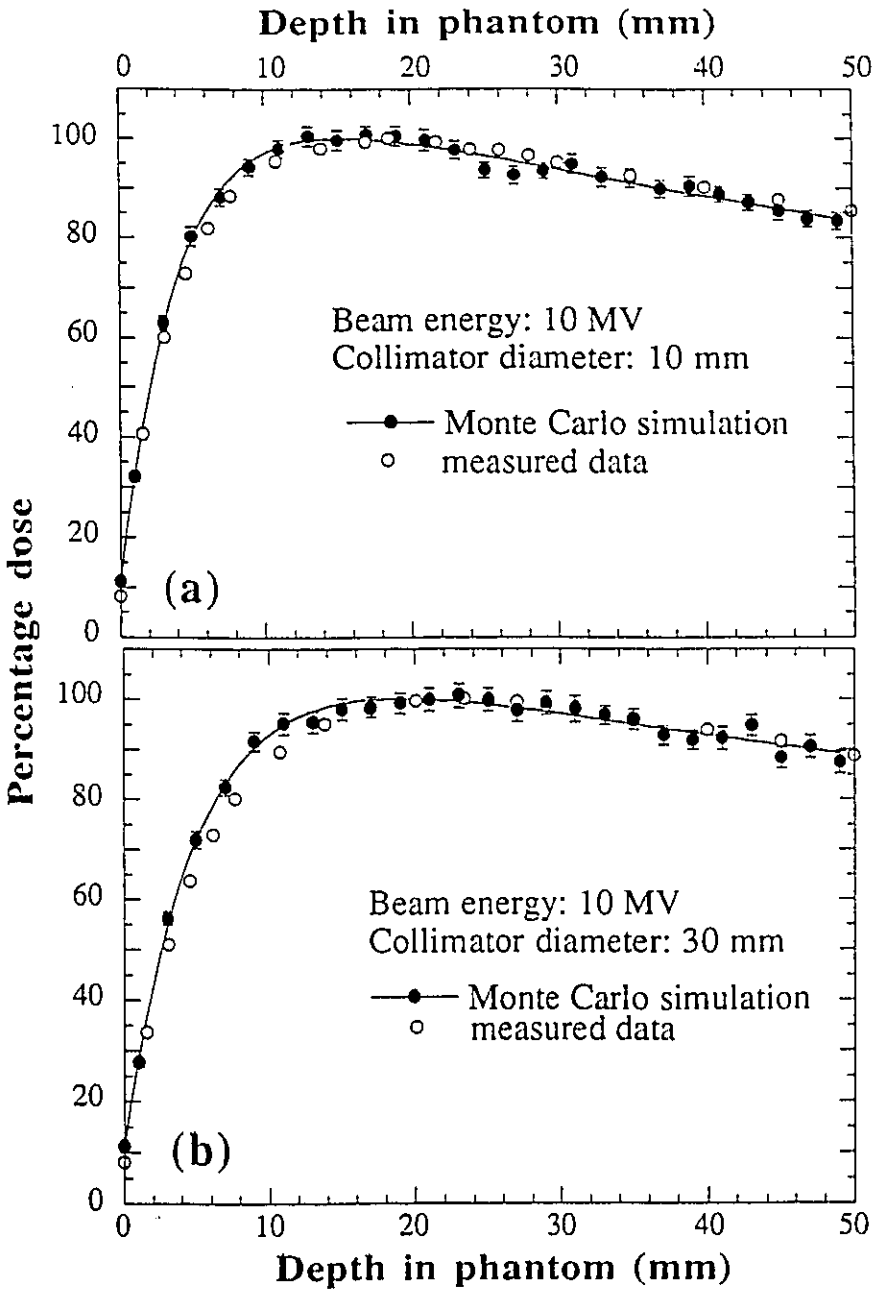

Figure 5.6 Monte Carlo simulations compared to measurements of percentage depth doses in the build-up region of two 10 MV radiosurgical beams: (a) 10 mm diameter and (b) 30 mm diameter. The measured data is represented by open circles, while the solid circles indicate the calculated points. A fitted curve is drawn through the simulated data points.

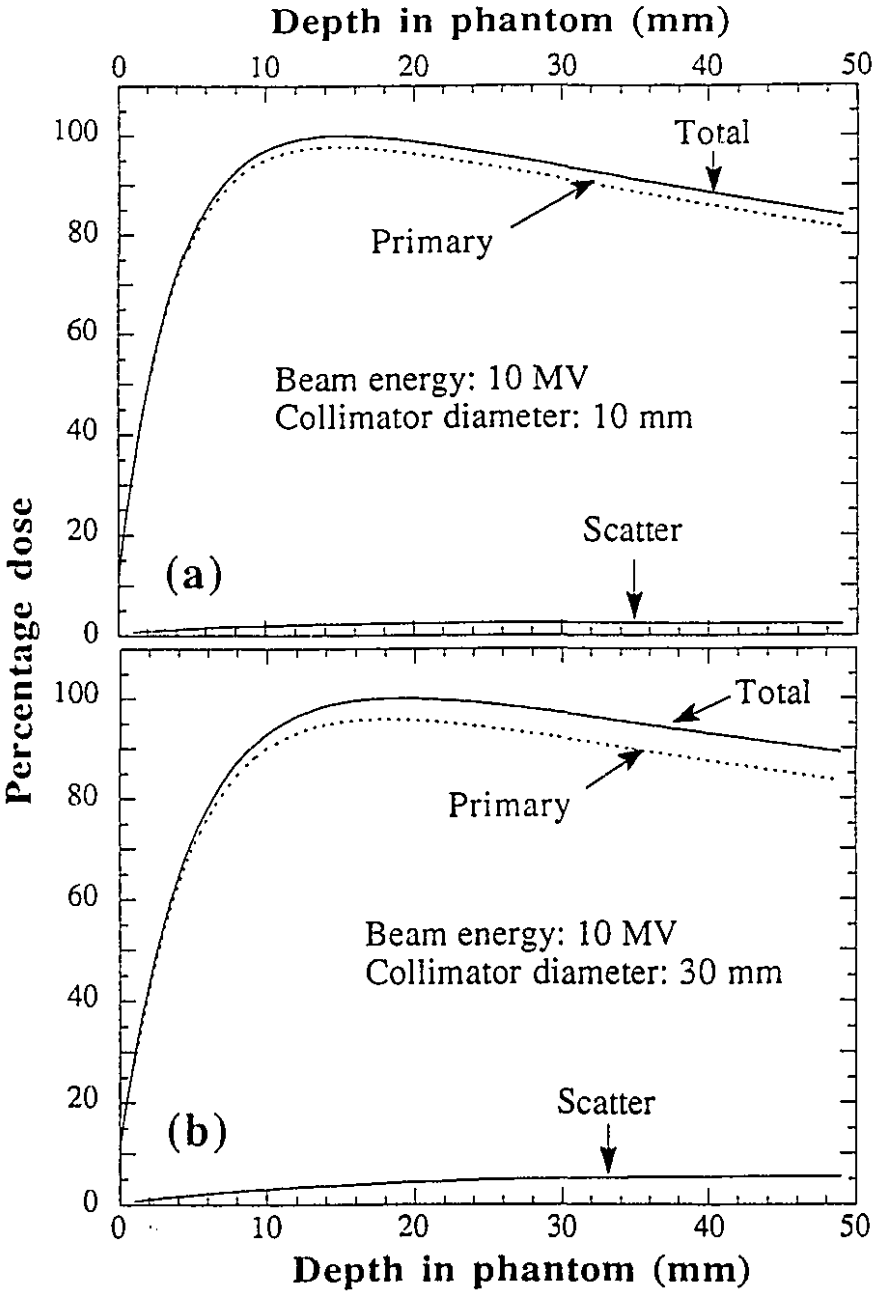

Figure 5.7 Monte Carlo calculation of percentage depth doses in the build-up region of two 10 MV radiosurgical beams: (a) 10 mm diameter and (b) 30 mm diameter. Shown are the fitted curves to calculated total dose, primary dose and scattered dose.

contribution and the other the scattered dose, both plotted as a percentage of the total dose at the depth of dose maximum. The error on the primary and scattered data points, though calculated, is not shown for the sake of clarity. However, these errors are comparable to the errors on the total dose, which were seen to be within acceptable levels. The calculated total, primary, and scattered doses are represented in Fig. 5.7 by fitted curves.

The primary and scatter dose data of Fig. 5.7(a) and (b) are replotted in Fig. 5.8. The scattered doses for both field sizes are similar at the phantom surface and in the build-up region, but with increasing depth the scatter component of the larger field (30 mm diameter) increases considerably faster than that of the smaller field (10 mm diameter). For both field sizes, the relative primary dose shows an essentially equal contribution to total dose in the region beyond d_{max}. In the build-up region, the primary beam of the smaller field reaches its maximum at shallower depths and represents a greater proportion of the total dose than does the primary beam of the larger field. Thus, in the build-up region, the main characteristics of the percent depth dose curve are established by the primary dose deposition. Beyond d_{max}, on the other hand, the increase in depth doses with field diameter is caused by increased phantom scatter, as the primary components of the radiosurgical beams are essentially independent of field size at these depths.

5.3.3 *ANALYSIS AND DISCUSSION*

For the incident photon energies in question, Compton scattering is by far the most probable form of interaction with the medium. The most

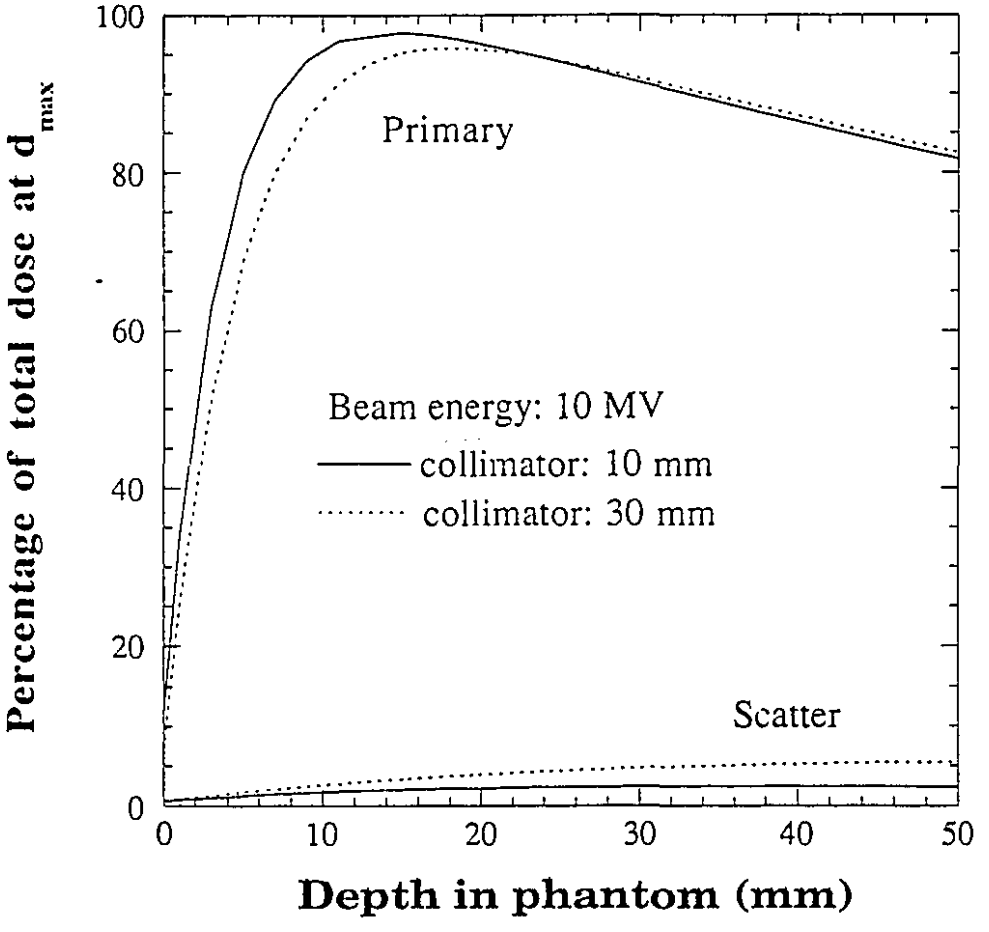

Figure 5.8 Primary and scattered Monte Carlo calculated doses of Fig. 5.7(a) and (b). The solid and dotted curves are for the 10 mm and 30 mm collimator diameters, respectively.

probable recoil electron angle for the given 10 MV photon spectrum is 8° with a weighted average energy of 2.4 MeV, corresponding to a range in tissue of about 12 mm (6). The few electrons that get scattered at larger angles have a lower energy and thereby a shorter range (~ 2 mm at 50°). Thus, for small field sizes the Compton electrons generated in the field periphery will contribute to the central axis dose at some depth greater than their depth of origin. As the field size increases, the additional electrons originating further laterally from the central axis will deposit dose deeper on the central axis, thereby increasing the depth of maximum dose. However, as the field size is further increased this effect quickly saturates, as the electrons originating in the periphery of large fields no longer have enough energy to reach the central axis. The depths of dose maxima for radiosurgical photon beams are thus expected to increase with field size and then remain constant once the largest value contributed from side scattered electrons is attained. A further discussion of the effect is given in *Chapter 7*.

5.4 Summary and conclusions

In this chapter, we examine the physical parameters of narrow radiation beams used in radiosurgery. The beam data needed for radiosurgical treatment planning consists of beam profiles (off-axis ratios), percentage depth doses and total scatter correction factors. This data is presented as a function of field diameter and beam energy. Beam profiles do not exhibit a significant energy dependence, although of course they change with field size and with depth in phantom due to the geometric

beam divergence. Percentage depth dose curves become more penetrating with increasing beam energy and increasing field size. Total scatter correction factors also increase with increasing field size. The change in depth dose values as well as in total scatter data is attributed to an increase in phantom scatter as a greater volume of material is irradiated with a larger beam diameter. This scatter increase is amplified at higher beam energies.

A closer examination of the percentage depth dose curves shows that the characteristics of narrow radiation beams differ from those of larger beams used in standard radiotherapy. In particular, the depth of dose maximum, d_{max}, of radiosurgical photon beams increases with increasing field size in contrast to the case of the relatively large fields used in standard radiotherapy where d_{max} decreases with increasing field size. Collimator scatter factors are found to be independent of field size, implying that the shift in d_{max} is not due to a change in machine head scatter. Agreement between Monte Carlo calculations, which do not account for collimator scatter, and measured data further supports this conclusion. The Monte Carlo simulations indicate that the primary dose deposition, i.e., the dose deposited by Compton electrons generated in a first photon interaction, is the greatest factor affecting the depth of dose maximum. The doses in the build-up region and the actual depths of dose maxima of radiosurgical beams are important not only in the calculation of dose distributions for small shallow intracranial lesions treated with radiosurgery, but also in increasing our understanding of radiosurgical beams in general.

5.5 References

1. P.V. Houdek, J.M. Van Buren and J.V. Fayos, *Dosimetry of small radiation field for 10 MV x-rays*, Med. Phys. **10**: 333-336, 1983.
2. G. Arcovito, A. Piermattei, G. D'Abramo and F.A. Bassi, *Dose measurements and calculations of small radiation fields for 9-MV x rays*, Med. Phys. **12**: 779-784, 1985.
3. R.K. Rice, J.L. Hansen, G.K. Svensson and R.L. Siddon, *Measurements of dose distributions in small beams of 6 MV x-rays*, Phys. Med. Biol. **32**: 1087-1099, 1987.
4. B.E. Bjärngard, J.-S. Tsai and R.K. Rice, *Doses on the central axis of narrow 6-MV x-ray beams*, Med. Phys. **17**: 794-799, 1990.
5. J. Dutreix, A. Dutreix and M. Tubiana, *Electronic equilibrium and transition stages*, Phys. Med. Biol. **10**: 177-190, 1965.
6. K.E. Sixel, *Physical parameters of narrow photon beams in radiosurgery*, M. Sc. Thesis, McGill University, Montréal, 1990.
7. K.E. Sixel and E.B. Podgorsak, *Build-up region of high energy photon beams in radiosurgery*, (abstract) Med. Phys. **19**: 843, 1992.
8. K.E. Sixel and E.B. Podgorsak, *Build-up region of high energy x-ray beams in radiosurgery*, Med. Phys. **20**: 761-764, 1993.
9. H.E. Johns and J.R. Cunningham, The physics of radiology, 4th edition, Charles C. Thomas, Springfield, Illinois, 1983, pp. 346-356.
10. F. M. Khan, W. Sewchand, J. Lee and J. F. Williamson, *Revision of tissue-maximum-ratio and scatter-maximum-ratio concepts for cobalt-60 and higher energy x-ray beams*, Med. Phys. **7**: 230-237, 1980.

11. P.J. Biggs and C.C. Ling, *Electrons as the cause of the observed d_{max} shift with field size in high energy photon beams*. Med. Phys. **6**: 291-295, 1979.

12. R. Mohan, C. Chui and L. Lidofsky, *Energy and angular distributions of photons from medical linear accelerators*, Med. Phys. **12**: 592-597, 1985.

CHAPTER 6

AN ANALYTICAL REPRESENTATION OF RADIOSURGICAL DEPTH DOSE DATA

6.1 Introduction

In radiosurgery certain beam parameters show trends different from those observed with the large field sizes used in standard radiotherapy (1,2). For example, in *Chapter 5* we discuss in some detail how, for a given photon beam energy, the depth of dose maximum, d_{max}, increases with increasing field diameter in the range from 10 mm to 30 mm. Furthermore, this increase is found to be proportional to the photon beam energy.

In the radiosurgical treatment planning software the percentage depth doses (PDD) are usually stored in look-up tables, which are relatively simple if one assumes the same depth of dose maximum for all beam diameters. However, if one also wishes to account for the shifts in depths of dose maxima, then the look-up tables become more elaborate and cumbersome, and it is quite possible that a simple analytical parametrization of depth dose data would prove more practical for use in the radiosurgical treatment planning software. Many algorithms currently used for dose calculations require fixed d_{max} values (3-5). In the proposed analytical representation of depth doses, this limitation would be overcome.

In this chapter, we discuss a simple method for the parametrization of depth dose data in the build-up region, through the depth of dose maximum to large depths in phantom for 6 MV, 10 MV and 18 MV radiosurgical x-ray beams (6,7). The method allows us to represent percentage depth dose data as a function of depth, field diameter and beam energy.

6.2 Materials and methods

The photon beam percentage depth doses were measured in water at a source-surface distance (SSD) of 100 cm using apparatus described in *Chapter 2*: the 3-D plotter with the p-type semi-conductor detector and, in the build-up region, the end-window parallel plate ionization chamber. The radiosurgical field sizes ranged from 10 mm to 30 mm in diameter, used with 6 MV, 10 MV and 18 MV x-ray beams.

Nonlinear curve fitting was performed with a commercially available graphics software package on a Macintosh computer (KaleidaGraph, Abelbeck Software). The general curve-fitting program, based on a Marquardt algorithm (8), is both powerful and efficient, able to fit any arbitrary single variable function containing up to nine fitted parameters.

6.3 The analytical representation

6.3.1 *BI-EXPONENTIAL FITTING TO MEASURED DATA*

The analytical description of all measured radiosurgical beam percentage depth doses (PDD) is based on a bi-exponential function:

$$PDD(d,\phi) = A_1 \exp(-\beta_1 d) - A_2 \exp(-\beta_2 d) , \qquad (6.1)$$

where d is the depth in phantom on the central beam axis, ϕ is the field diameter at the phantom surface, and A_1, A_2, β_1 and β_2 are the fitted parameters which depend on ϕ.

The form of this equation is analogous to that used by Johns *et al* (9), and Brahme and Svensson (10). The first term of Eq. 6.1 represents the primary component of the beam, while the second term represents the scattered component. In this context, β_1 corresponds to the primary beam attenuation coefficient and β_2 to the scattered beam attenuation coefficient. The amplitudes A_1 and A_2 have dimensions of relative dose and are related to the energy fluence of the primary and scattered particles, respectively. However, this approach should not be taken too rigorously, as the separation of a measured PDD curve into primary and scattered dose is not straightforward. Though we are considering only small field sizes, the total dose at a given depth in phantom consists of both scattered and primary components. As field size is increased, the scatter proportion of total dose at a given depth also increases, and the bi-exponential representation no longer holds.

An example of Eq. 6.1 used in fitting the experimental radiosurgical depth doses is shown in Fig. 6.1 for various beam energies and field diameters. Parts (a) and (b) are for a 6 MV x-ray beam and a field diameter of 10 mm, parts (c) and (d) are for a 10 MV x-ray beam and a field diameter of 20 mm, and parts (e) and (f) are for an 18 MV x-ray beam and a field diameter of 30 mm. Parts (b), (d) and (f) in Fig. 6.1 represent the build-up regions of parts (a), (c) and (e), respectively. Experimental data are shown as points, the two exponentials used in Eq. 6.1 are given separately by solid curves, and Eq. 6.1 is represented by the dashed curve. As shown in Fig. 6.1 with appropriate curve-fitting parameters the agreement between Eq. 6.1 and experimental data is excellent, confirming the validity of the analytical depth dose description of radiosurgical beams with simple bi-exponential functions. The regions of depth dose maxima are quite broad,

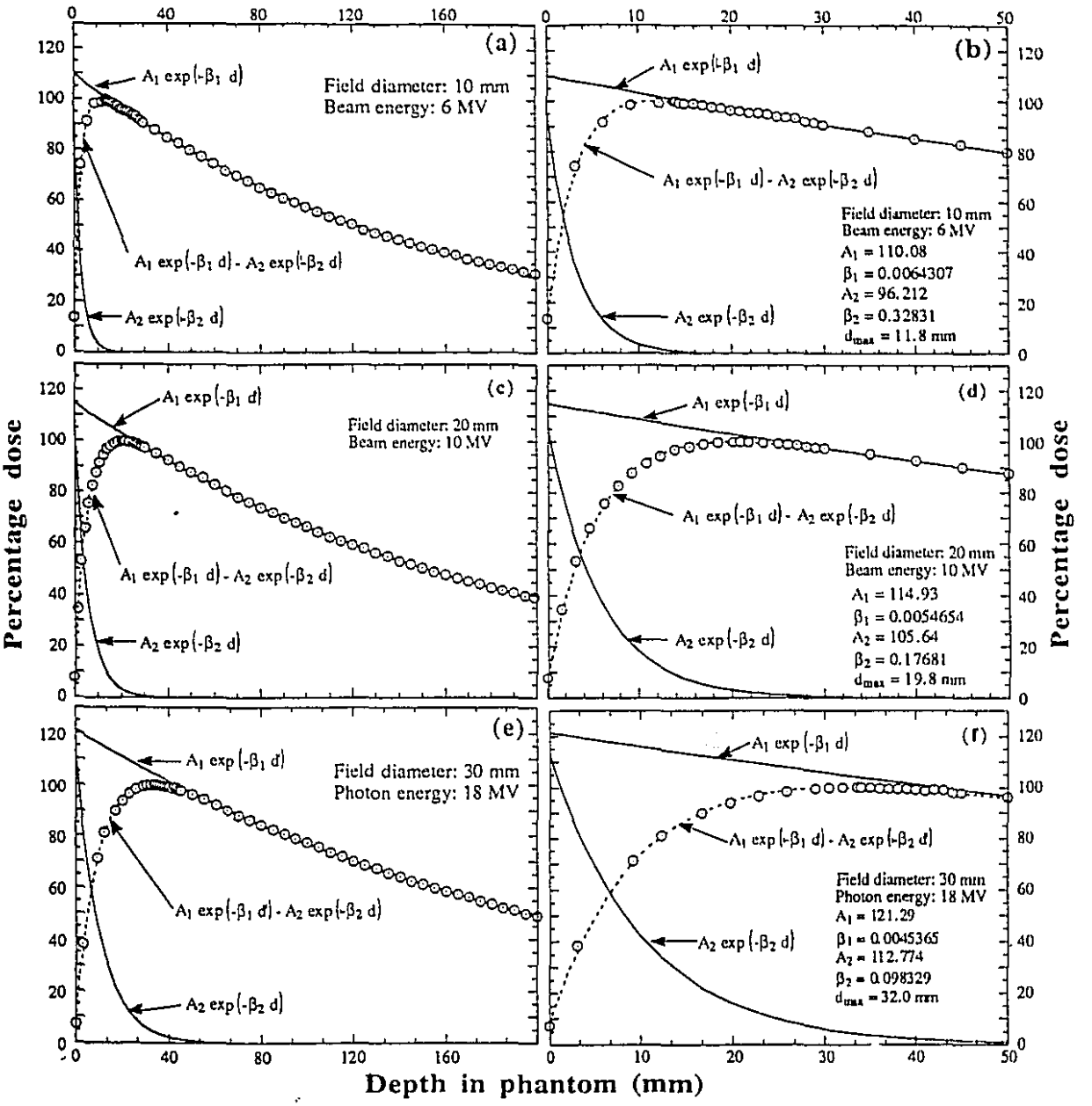

Figure 6.1 Radiosurgical percentage depth doses: parts (a) and (b) 10 mm field diameter, 6 MV x-ray beam; parts (c) and (d) 20 mm field diameter, 10 MV x-ray beam; and parts (e) and (f) 30 mm field diameter, 18 MV x-ray beam. Experimental data are shown as data points, the two exponentials from Eq. 6.1 as solid curves and Eq. 6.1 with appropriate parameters as the dashed curve. The respective fitting parameters of Eq. 6.1 are listed in parts (b), (d) and (f).

yet d_{max} can be determined uniquely by finding the maxima of Eq. 6.1 mathematically using the appropriate parameters. For the three beams of Fig. 6.1 the calculated dose maxima are 11.8 mm, 19.8 mm and 32.0 mm, respectively.

Bi-exponential functions were fit to measured PDD data for other available radiosurgical field sizes for each beam energy and the results were similar to those shown in Fig. 6.1. We found that the quality of the fit was independent of beam energy or field diameter, and that the radiosurgical beams could be represented accurately in the build-up and fall-off regions, as well as in regions around d_{max}. Furthermore, the increase in depth of dose maximum with increasing field size, as observed experimentally for radiosurgical fields, was reproduced analytically.

The quality achieved at this step of the curve-fitting procedure has a strong influence on the final results of the PDD data parametrization. To assure a valid approximation for a given PDD distribution, one should use a sufficiently large number of experimental points (50 or more) measured over a depth of at least 200 mm. Moreover, as many as one third of the data points involved in the curve-fitting procedure should cover the build-up region and the region close to d_{max}.

It was noted above, that the scatter proportion of total dose affects the adequacy of the parametrization technique. We attempted to apply the same equation to standard radiotherapy fields. However, we found that two exponentials were inadequate to represent the large field PDD data accurately, with the greatest deviations between measurement and calculation occuring at large depths where phantom scatter plays an increasingly important role. A minimum of three exponentials was

required to result in a valid approximation for field sizes with a large scatter component of the PDD data.

6.3.2 *POLYNOMIAL FITTING TO BI-EXPONENTIAL PARAMETERS*

In the second stage of the fitting procedure, the calculated parameters A_i and β_i were subjected to polynomial curve fitting as a function of field diameter ϕ for the 6 MV, 10 MV, and 18 MV x-ray beams. The results for a polynomial of degree 2 are shown in Fig. 6.2 with parts (a), (b), (c) and (d) giving the polynomial fits for the parameters A_1, β_1, A_2, and β_2, respectively. For each parameter, the curves change monotonically with field size and are energy dependent. The second order polynomials were of the following form:

$$A_1(\phi) = \sum_{i=0}^{2} A_{1i}\,\phi^i \;; \qquad A_2(\phi) = \sum_{i=0}^{2} A_{2i}\,\phi^i \;;$$
$$\beta_1(\phi) = \sum_{i=0}^{2} \beta_{1i}\,\phi^i \;; \qquad \beta_2(\phi) = \sum_{i=0}^{2} \beta_{2i}\,\phi^i \;; \tag{6.2}$$

The fitting parameters of Fig. 6.2 which are appropriate for the linac energies and radiosurgical field sizes available at McGill University are given in Table 6.1.

The quality of the polynomial fits depends on two factors. First, a large number of A_i and β_i points must be available for fitting, i.e., to ensure the quality of the polynomial approximation, a large number of measured data sets corresponding to many radiosurgical field diameters is needed. The second factor is the order of the polynomial (n) used in the curve-fitting

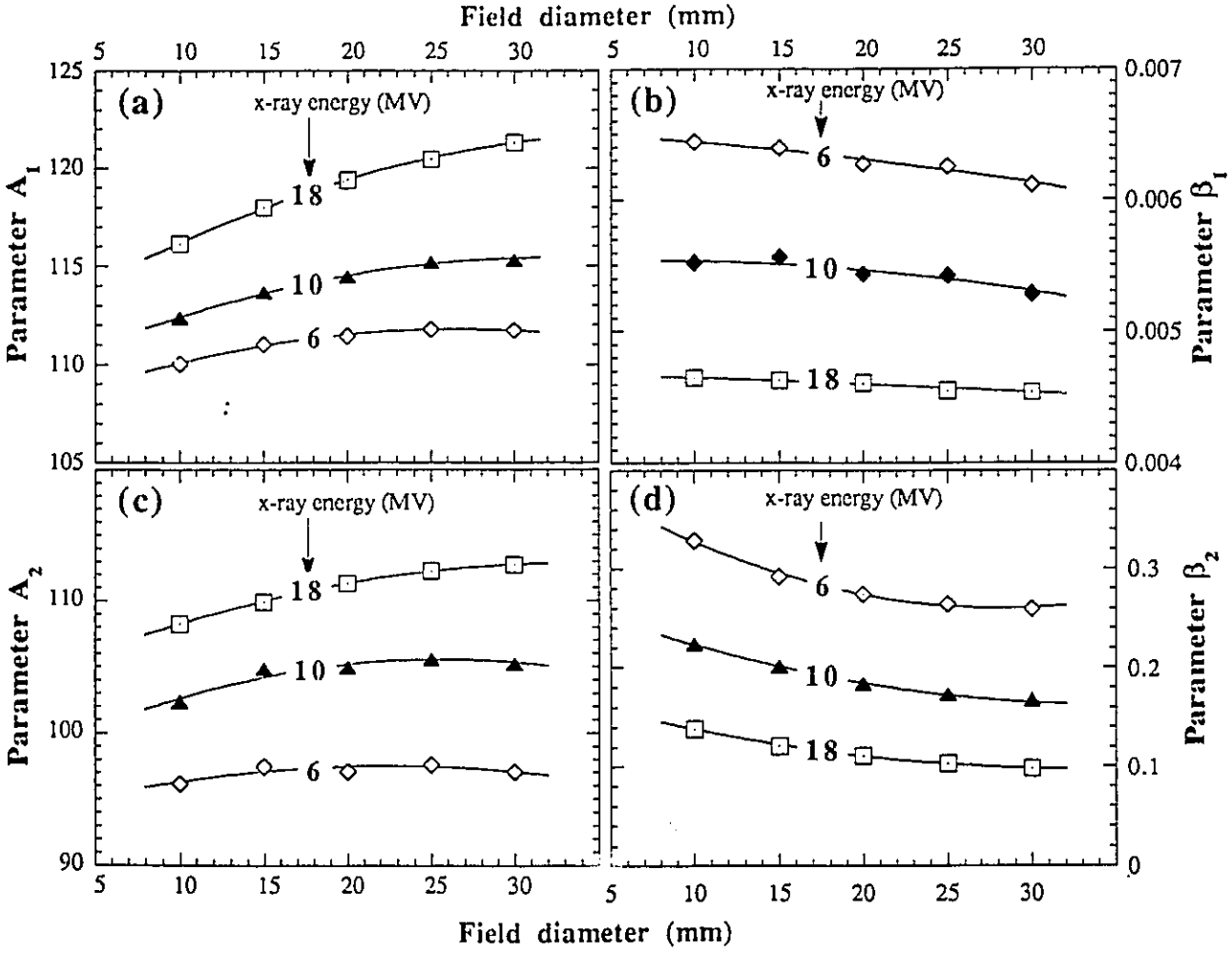

Figure 6.2 The results of the 2nd degree polynomial curve fitting of the bi-exponential parameters as a function of the field diameter for the 6 MV, 10 MV and 18 MV x-ray beams. Parts (a), (b), (c) and (d) correspond to fits of A_1, β_1, A_2 and β_2, respectively.

Table 6.1 Table of coefficients used with the polynomials of Eq. 6.2, describing the dependence of the fitted bi-exponential parameters A_i and β_i on the field diameter ϕ for the 6 MV, 10 MV and 18 MV x-ray beams.

Parameters		Beam energy		
		6 MV	10 MV	18 MV
A_1	A_{10}	107.39	109.07	111.64
	A_{11}	0.330	0.393	0.520
	A_{12}	-6.19×10^{-3}	-6.04×10^{-3}	-6.60×10^{-3}
β_1	β_{10}	6.53×10^{-3}	5.52x10-3	4.69×10^{-3}
	β_{11}	-6.86×10^{-6}	5.86×10^{-6}	-3.27×10^{-6}
	β_{12}	-2.22×10^{-7}	-4.36×10^{-7}	-5.91×10^{-8}
A_2	A_{20}	93.52	97.54	103.51
	A_{21}	0.358	0.626	0.553
	A_{22}	-7.97×10^{-2}	-1.22×10^{-2}	-8.14×10^{-3}
β_2	β_{20}	0.4106	0.281	0.180
	β_{21}	1.14×10^{-2}	-6.80×10^{-3}	-4.95×10^{-3}
	β_{22}	2.02×10^{-4}	9.77×10^{-5}	7.43×10^{-5}

of A_i and β_i as a function of field diameter. If n is too large, the calculated lines are very convoluted instead of following the data points in a monotonic fashion and thus, for intermediate collimator sizes, the calculated A_i and β_i could be largely under- or over-estimated.

To decide on the suitable order of the polynomial for an accurate PDD representation, the depth of dose maximum was calculated with polynomials of n=1 and n=2, and compared to d_{max} values obtained for no polynomial fitting, i.e., calculated directly from measured data fit to the bi-exponential equation. In the analytical PDD representation d_{max} is easily calculated, once the parameters A_i and β_i have been found, by finding the maximum of Eq. 6.1.

Figure 6.3 shows the behaviour of d_{max} as a function of field diameter for the 6 MV, 10 MV and 18 MV radiosurgical x-ray beams. The data points correspond to values of d_{max} calculated from Eq. 6.1 with no polynomial fitting, the dashed curves represent d_{max} calculated with A_i and β_i fit to a linear curve (n=1), and the solid curves represent d_{max} calculated with A_i and β_i fit to a 2nd order polynomial (n=2). Clearly, the polynomial fitting of order n=2 reproduces well the d_{max} for all radiosurgical field sizes and beam energies, while a linear fit to the bi-exponential parameters results in an inadequate reproduction of measured d_{max}. Thus, we choose n=2 as the lowest order polynomial that can be used to represent correctly the bi-exponential parameters A_i and β_i.

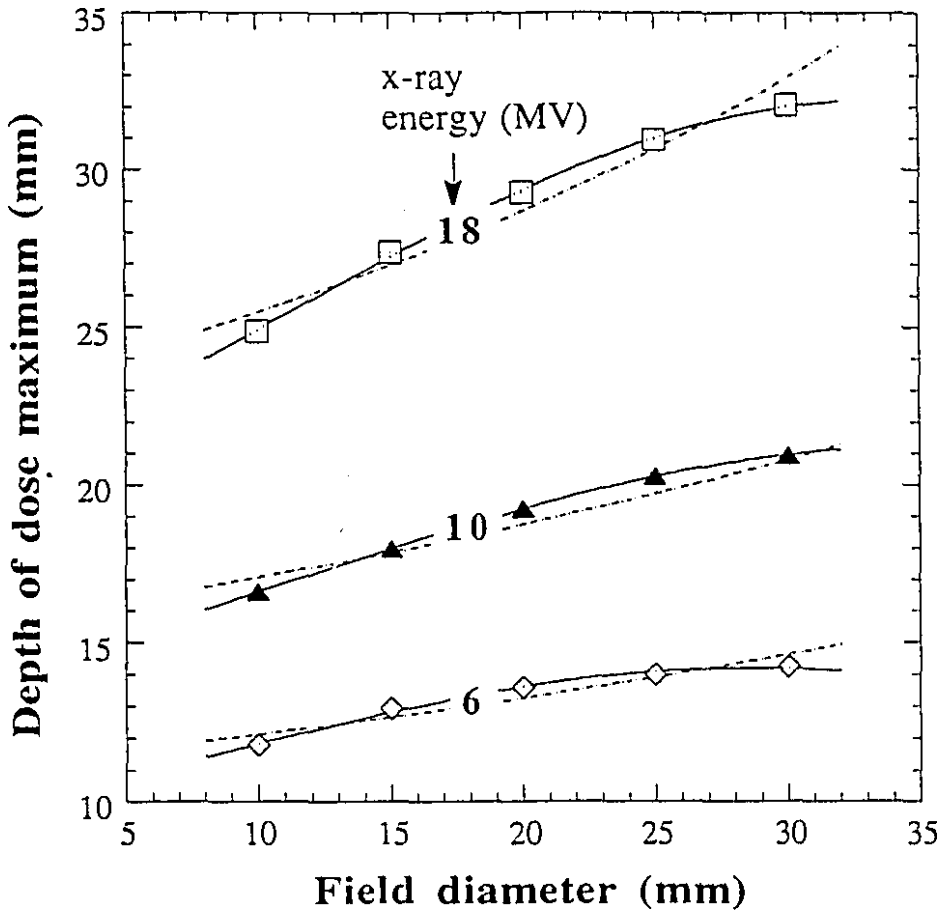

Figure 6.3 Depth of dose maximum, d_{max}, as a function of field diameter for 6 MV, 10 MV, and 18 MV x-ray beams. The data points represent d_{max} calculated directly from the the bi-exponential with no polynomial fitting, the dashed curves represent d_{max} calculated from Eq. 6.1 with A_i and β_i fit to a linear curve (n=1), and the solid line represents d_{max} calculated with A_i and β_i fit to a 2nd order polynomial (n=2).

6.3.3 *EVALUATION OF THE BI-EXPONENTIAL REPRESENTATION*

To evaluate the quality of the analytical representation, we have generated PDD data according to the described parametrization process. For a given beam energy, we choose the appropriate equation for $A_i(\phi)$ and $\beta_i(\phi)$ with n=2 to find the bi-exponential parameters for the given field size. These parameters are then used with Eq. 6.1 and the PDD values are calculated at the desired depth. Table 6.2 lists the PDD data calculated in this manner for 6 MV, 10 MV and 18 MV x-ray beams for three field diameters: 10 mm, 20 mm, and 30 mm. Also listed in Table 6.2 are the measured PDDs at the corresponding depths and the percentage difference between the measured and calculated values. The agreement between calculated and measured data is generally better than 3%. In some cases, the errors in the build-up region and at the phantom surface were slightly higher. These differences can be attributed to experimental uncertainties, as the conversion of ionization to dose at the phantom surface is not trivial.

The comparison between measured and calculated data can be summarized as follows: 63.5% of the total number of calculated data points matched corresponding measured data points within an error range of ±0.5%, 86.5% within ±1.0%, 94.1% within ±1.5% and 96.5% within ±3.0%.

6.4 Summary and conclusions

In this chapter, we describe a compact, analytical representation consisting of a set of mathematical equations, which was developed to

Table 6.2 Measured (m) and calculated (c) percentage depth doses at selected depths for 10 mm, 20 mm, and 30 mm field diameters and 6 MV, 10 MV, and 18 MV x-ray beams. The polynomial degree chosen for the bi-exponential parameters A_1, β_1, A_2, and β_2 was n=2. Also tabulated are the percentage differences (Δ%) between the measured and calculated values.

Beam energy (MV)	Depth in water (mm)	Percentage depth doses measured: m calculated: c percentage difference: Δ%								
		Field diameter: 10 mm			Field diameter: 20 mm			Field diameter: 30 mm		
		m	c	Δ%	m	c	Δ%	m	c	Δ%
6	0.0	13.86	13.77	0.9	14.34	14.02	1.5	14.66	14.63	0.2
	5.0	87.93	86.83	1.2	83.37	81.93	1.7	81.84	80.59	1.5
	10.0	99.58	99.15	0.4	98.43	97.70	0.7	97.86	97.14	0.7
	30.0	90.73	90.73	0.0	92.32	92.26	0.1	92.97	92.91	0.1
	50.0	79.78	79.77	0.0	81.46	81.37	0.1	82.31	82.25	0.1
	100.0	57.84	57.81	0.1	59.53	59.37	0.3	60.63	60.55	0.1
	200.0	30.41	30.36	0.2	31.80	31.61	0.6	32.90	32.82	0.2
10	0.0	9.933	9.816	1.2	9.287	9.334	0.5	10.40	10.08	3.0
	5.0	75.27	72.20	2.6	68.19	69.53	2.0	64.98	66.22	1.9
	10.0	95.02	92.90	2.2	90.79	91.74	1.0	88.26	89.22	1.1
	30.0	94.99	94.97	0.0	97.02	96.78	0.2	97.94	97.70	0.2
	50.0	85.08	85.22	0.2	87.43	87.13	0.3	88.57	88.51	0.1
	100.0	64.36	64.62	0.4	66.54	66.32	0.3	67.34	67.92	0.9
	200.0	36.83	37.15	0.9	38.52	38.40	0.3	38.89	39.96	2.8
18	0.0	7.95	7.95	0.0	8.04	8.09	0.6	8.58	8.53	0.6
	5.0	59.63	59.21	0.1	52.60	52.69	0.2	49.56	49.62	0.1
	10.0	84.25	83.65	0.1	77.09	77.24	0.2	73.66	73.75	0.1
	30.0	99.97	99.32	0.6	99.71	99.99	0.3	99.95	99.96	0.0
	50.0	92.56	91.96	0.6	94.13	94.42	0.3	95.87	95.85	0.0
	100.0	73.46	72.97	0.7	75.11	75.37	0.3	77.05	77.04	0.0
	200.0	46.16	45.83	0.7	47.38	47.57	0.4	48.92	48.94	0.0

generate radiosurgical x-ray beam percentage depth dose data at arbitrary depths and field sizes for 6 MV, 10 MV, and 18 MV x-ray beams. Systematic bi-exponential fits to measured PDD data, followed by a series of second order polynomial fits to the bi-exponential parameters, were obtained for small circular radiosurgical fields with diameters varying from 10 mm to 30 mm.

The quality of the parametrized PDD representation was tested extensively by comparing the calculated percentage depth doses to corresponding experimental points. The results show that an analytical description is a suitable method for PDD calculation, as over 94% of the total calculated data points were reproduced within ±1.5% of the measured values. Furthermore, d_{max} values which are a function of field diameter and beam energy also can be determined accurately with the bi-exponential approximation.

Once the parametrization process is complete, only the resulting four polynomials per beam energy plus one bi-exponential equation are required for calculating the percentage depth doses at given depths and for a given field size. First, the beam energy, i.e., the suitable set of four polynomials is chosen. The four bi-exponential parameters are calculated from the respective four polynomials by substituting the desired field size for the variable ϕ. The four calculated parameters are then substituted into the bi-exponential equation and the percentage depth dose is calculated at the specified depth.

The mathematical equations determined through the fitting procedure can be implemented easily in any computer program that requires fast and accurate PDD calculations. Since they generate only smooth PDD curves, this method will reduce the effect of any measurement

errors. An additional argument in support of an analytical model is the small amount of computer storage space needed to house a large amount of information. We believe that this analytical representation is a viable alternative to large look-up tables needed in computerized calculations of radiosurgical dose distributions, especially if changes in the position of the depth of dose maximum with field diameter are to be accounted for. Preliminary implementation of the analytical beam data in the treatment planning software used at our center has indicated that the time to calculate the percentage depth dose is comparable to the time required to look-up a given value. Thus storage space is saved without compromising quality or speed in treatment planning.

6.5 References

1. R.K. Rice, J.L. Hansen, G.I. Svensson and R.L. Siddon, *Measurements of dose distributions in small beams of 6 MV x-rays*, Phys. Med. Biol. **32**: 1087-1099, 1987.
2. C.F. Serago, P.V. Houdek, G.H. Hartmann, D.S. Saini, D.S. Serage and A. Kaydee, *Tissue maximum ratios (and other parameters) of small circular 4, 6, 15 and 24 MV x-ray beams for radiosurgery*, Phys. Med. Biol. **37**:1943-1956, 1992.
3. G.B. Pike, E.B. Podgorsak, T.M. Peters and C. Pla, *Dose distributions in dynamic stereotactic radiosurgery*, Med. Phys. **14**: 780-789, 1987.
4. G. Luxton, G. Jozsef and M.A. Astrahan, *Algorithm for dosimetry of multiarc linear-accelerator stereotactic radiosurgery*, Med. Phys. **18**: 1211-1221, 1991.
5. E.B. Podgorsak, *Physics for radiosurgery with linear accelerators*, Neurosurgery Clinics of North America **3**: 9-34, 1992.
6. W. Wierzbicki, K.E. Sixel and E.B. Podgorsak, *An analytical representation of radiosurgical depth dose data*, (abstract) Proceedings of the 39th meeting of the Canadian Organization of Medical Physicists (COMP) and the 19th meeting of the Canadian Medical and Biological Engineering Society (CMBE), Ottawa, Ontario, May 12-15, pp. 258-259, 1993.
7. W. Wierzbicki, K.E. Sixel and E.B. Podgorsak, *An analytical representation of radiosurgical depth dose data*, Phys. Med. Biol. **38**: (in press), 1993.
8. D.W. Marquardt, *An algorithm for least squares estimation of nonlinear parameter*, J. Soc. Ind. App. Math. **2**: 431-441, 1963.

9. H.E. Johns, E.K. Darby, R.N.H. Haslam, L. Katz and E.L. Harrington, *Depth dose data and isodose distributions for radiation from a 22 MeV betatron*, Am. J. Roentgenol. **62**: 257-268, 1949.

10. A. Brahme and H. Svensson, *Radiation beam characteristics of a 22 MeV microtron*, Acta. Radiol. Oncol. **18**: 244-270, 1979.

CHAPTER 7

BUILD-UP REGION OF MEGAVOLTAGE X-RAY BEAMS

7.1 Introduction

In general, the depth of dose maximum, d_{max}, of megavoltage x-ray beams produced by linacs is a function of both beam energy and field size. For a given field size, d_{max} increases with photon beam energy, i.e., a high energy x-ray beam is more penetrating than a low energy beam. It is shown in *Chapter 5* that for a given beam energy, d_{max} increases with field size for small diameter x-ray beams. However, at large field sizes, it is well known that the opposite effect occurs, namely, d_{max} decreases with increasing field size. The energy dependence of d_{max} is of major clinical importance since it determines the extent of the dose build-up region. The field size dependence, on the other hand, is relatively unimportant and generally ignored in standard radiotherapy. However, it is of interest from the basic radiotherapy physics point-of-view and should be understood as it can have clinical consequences in some specialized radiation therapy procedures, such as radiosurgery of superficial intracranial lesions with small radiation fields or radiation treatments with very large radiation fields (mantle fields, half-body irradiation, total-body irradiation).

Although both small and large fields exhibit a d_{max} field size dependence, the cause for this effect is different for small fields compared to large fields. For small radiosurgical fields, the increase in d_{max} with increasing field size is discussed in some detail in *Chapter 5*. The d_{max} shift is independent of machine head contaminants, and is attributed to variations in dose deposition by electrons originating in the phantom. In contrast, for large radiotherapeutic field sizes the decrease in d_{max} with an increasing field size is caused by scattered electrons generated in the machine head (1,2).

Work to verify that the surface contaminants of large fields are in fact electrons (3) originating in the linac head (4,5) and attempts to remove these electrons from the x-ray beam (6,7) have resulted in a wealth of literature on this subject over the past decade. Using a bending magnet to sweep electron contamination from the photon beam, Biggs and Ling (1) showed that electrons are responsible for the shift in d_{max} since the field size dependence of d_{max} was eliminated once the magnet removed the electrons from the beam.

Monte Carlo calculations (5,8) have shown that the x-ray field flattening filter of linacs is by far the greatest contributor of scattered electrons. In one of these studies (5), the primary photon beam was traced though the treatment head geometry and the calculated contamination electron spectrum was scored in three stages, corresponding to three electron sources: just below the beam flattening filter and monitor chamber; below the collimator jaws; and at the machine isocenter, with the air volume providing the electron contamination source. The results show that for a 25 MV photon beam about 70% of the contamination electrons originate in the flattening filter, about 10% originate in the collimator jaws and the remaining 20% originate in the volume of the irradiated air.

The apparent source of these electrons has been found experimentally by assuming that they originate at a point source and follow the inverse square law dependence (4). The surface dose was measured as a function of varying source-phantom distance (SPD). A plot of the inverse square root of normalized surface dose *vs* SPD yielded a straight line with an x-intercept at a distance of 12 cm below the primary photon source. Thus, it seems the electrons are produced at this point, which corresponds approximately to the position of the flattening filter.

However, despite the increased understanding provided by the above references, questions concerning the shift in d_{max} at large field sizes remain, the most immediate of which concerns the field size dependence itself. The field flattening filter of standard linacs is only a few cm in diameter and is therefore completely visible from the linac isocenter for all but the smallest field sizes, rather than being partially obstructed for different field sizes set by the linac collimator. Since the electrons leaving the filter travel mostly in the forward direction (5), simple geometric arguments question how a larger field size can then result in more scattered electrons reaching the isocenter and subsequently produce a greater shift in d_{max}.

In this chapter, we generalize the findings of *Chapter 5* where d_{max} of radiosurgical beams was discussed. We reexamine the energy and field size dependence of the depth of dose maximum and present data for field sizes ranging from small size radiosurgical fields to the very large field sizes available from linacs. We study the origin and nature of the shift in d_{max} at large field sizes and provide an explanation for the d_{max} shift that takes the dependence on field size into account (9,10).

7.2 Build-up region and depth of dose maximum

7.2.1 *MEASURED DATA*

The results of our measurements of d_{max} are shown in Fig. 7.1, where we plot depths of dose maxima as a function of the side of a square field for the 6 MV, 10 MV and 18 MV x-ray beams in the field size range

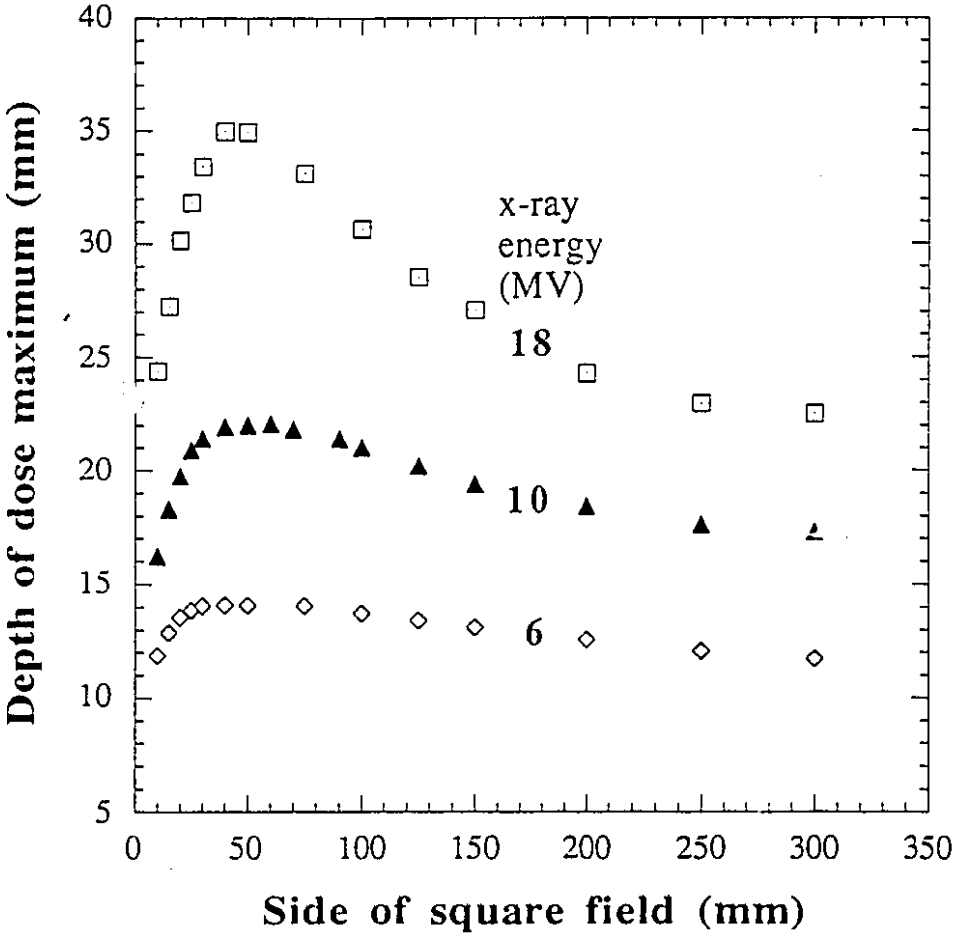

Figure 7.1 Depth of dose maximum, d_{max}, as a function of field size for 6 MV, 10 MV and 18 MV x-ray beams.

from 1x1 cm^2 to 30x30 cm^2. The x-ray beams were obtained from a Clinac-18 (10 MV) and Clinac-2100 C (6 MV and 18 MV), and the dose in the build-up region was measured with the end-window parallel plate chamber in a polystyrene phantom. This equipment is described in detail in *Chapter 2*. To obtain the d_{max} data points plotted on the graph, the bi-exponential curves discussed in *Chapter 6* were fit to the measured build-up region data, and the depths corresponding to the maxima of the curves were calculated. In the build-up region, where phantom scatter is a small proportion of the total dose, the bi-exponential model holds for all field sizes.

The d_{max} dependence on field size and beam energy for both large and small fields is clearly shown in Fig. 7.1. For a given field size, d_{max} increases with beam energy. For a given energy, however, the d_{max} behavior is more complicated, first showing a rapid increase with increasing field size for small fields, a saturation around 5x5 cm^2 and then a slow decrease with increasing field, dropping to a d_{max} value at 30x30 cm^2 that is almost equal to that for the 1x1 cm^2 field. The d_{max} increases in the region of small fields are about 3 mm, 6 mm and 11 mm for the 6 MV, 10 MV and 18 MV beams, respectively.

The d_{max} data of Fig. 7.1 are also given in Table 7.1, along with the percentage surface dose and total scatter correction factors (S_t) for the range of square fields and beam energies studied. Comparing percentage surface dose for a given beam energy, we see that for small field sizes, this value remains relatively constant, at about 14% for the 6 MV beam, 8% for the 10 MV beam and 5%-6% for the 18 MV beam. However, as field size increases beyond 5x5 cm^2, surface dose also increases dramatically, up to a maximum of 42% for the 6 MV, 30x30 cm^2 beam. For high energy beams, the Compton electrons through which most of the beam energy is deposited,

Table 7.1 Depth of dose maximum (d_{max}), percentage surface dose and total scatter correction factor for square fields ranging from 1×1 cm^2 to 30×30 cm^2 for 6 MV, 10 MV and 18 MV x-ray beams. The d_{max} data tabulated here is plotted in Fig. 7.1.

Field size	d_{max} (mm)			% surface dose			Total scatter correction factor		
(mm)	6 MV	10 MV	18 MV	6 MV	10 MV	18 MV	6 MV	10 MV	18 MV
10	11.9	16.2	24.4	13.7	6.4	5.0	0.683	0.584	0.538
15	12.9	18.3	27.2	13.3	7.5	5.4	0.820	0.765	0.701
20	13.6	19.8	30.1	13.3	7.4	5.5	0.870	0.839	0.784
25	13.7	20.9	31.8	13.7	7.5	5.8	0.889	0.882	0.831
30	14.0	21.4	33.4	14.2	7.5	6.3	0.904	0.901	0.863
40	14.1	21.9	35.0	15.4	8.7	7.5	0.923	0.925	0.902
50	14.1	22.0	34.9	16.5	9.6	8.9	0.940	0.940	0.925
100	13.7	21.0	30.7	22.2	15.6	17.1	1.000	1.000	1.000
150	13.1	19.4	27.1	26.4	21.4	26.2	1.027	1.027	1.045
200	12.6	18.4	24.3	33.0	26.8	31.0	1.046	1.055	1.071
250	12.1	17.6	23.0	37.4	31.0	35.8	1.052	1.067	1.083
300	11.7	17.3	22.5	42.1	34.0	39.7	1.066	1.078	1.104

are scattered primarily in the forward direction. Thus the surface dose of these beams is generally expected to be low, as there is little backscatter at high energies. The high measured values of surface dose observed for large fields in Table 7.1 thus reflect an increase in beam contamination with increasing field size.

As expected, the total scatter correction factors in the third group of columns of Table 7.1 increase with field size for a given beam energy. This factor accounts for the change in scatter, relative to a standard 10x10 cm^2 field, resulting from both phantom scatter and machine head scatter: thus we see an increase in S_t at both small and large field sizes.

7.2.2 *MONTE CARLO CALCULATIONS*

As in *Chapter 5*, when analyzing radiosurgical beams, we use a Monte Carlo simulation to study the dose deposition in the build-up region for the given range of field sizes. The Monte Carlo data were calculated with the EGS4 code, a user-writen interface and the PRESTA algorithm, using a published 10 MV photon beam spectrum (11). The code has been described in detail in *Chapter 3*. Incident particles were transported through a semi-infinite water phantom, with minimum electron and photon cut-off energies. Total dose was scored along the beam central axis as a function of depth in phantom for various field sizes. The size of the scoring voxels depended on the field size at isocenter and varied in cross-sectional area from 5x5 mm^2 to 15x15 mm^2. For all field sizes, the depth of the voxels was 2 mm. To obtain statistical uncertainties within a few percent, $1x10^6$ to $2x10^6$ histories were run in 10 batches and the results were

averaged. The number of histories was varied to maintain an approximately constant initial photon flux for each field size.

Typical results of the Monte Carlo simulation of the build-up region as compared to measured data are shown in Fig. 7.2. In parts (a) and (b) the measured data points are represented by open circles, with the bi-exponential curve fitted to this data shown as a dashed curve. The Monte Carlo data points are given by solid circles, with corresponding error bars, and the fitted curves by the solid lines. The results for a 2×2 cm^2 field are shown in part (a), while part (b) shows the measured and calculated build-up region dose for a 30×30 cm^2 field. For the small field size there is excellent agreement between measurement and calculation, similar to what was found for small radiosurgical field sizes. However, at large field sizes, the agreement between measurement and calculation is rather poor at depths shallower than d_{max}. Furthermore, the simulation does not reproduce the measured d_{max}.

In Fig. 7.3 we plot the d_{max} data calculated from the Monte Carlo simulations for the entire range of field sizes and the 10 MV x-ray beam. Also included in this figure is the d_{max} data obtained through measurements, previously plotted in Fig. 7.1. For small field sizes, d_{max} calculated with the Monte Carlo technique agrees well with measured data, rising monotonically with an increasing field size and showing that the dependence of d_{max} on small field sizes is caused by in-phantom scatter. However, at field sizes beyond 5×5 cm^2, the Monte Carlo calculated d_{max} saturates at a depth of about 21 mm and remains essentially independent of field size while the measured d_{max} decreases considerably. The difference between the measured d_{max} and that calculated by the Monte Carlo technique can be attributed to the fact that the Monte Carlo simulation does

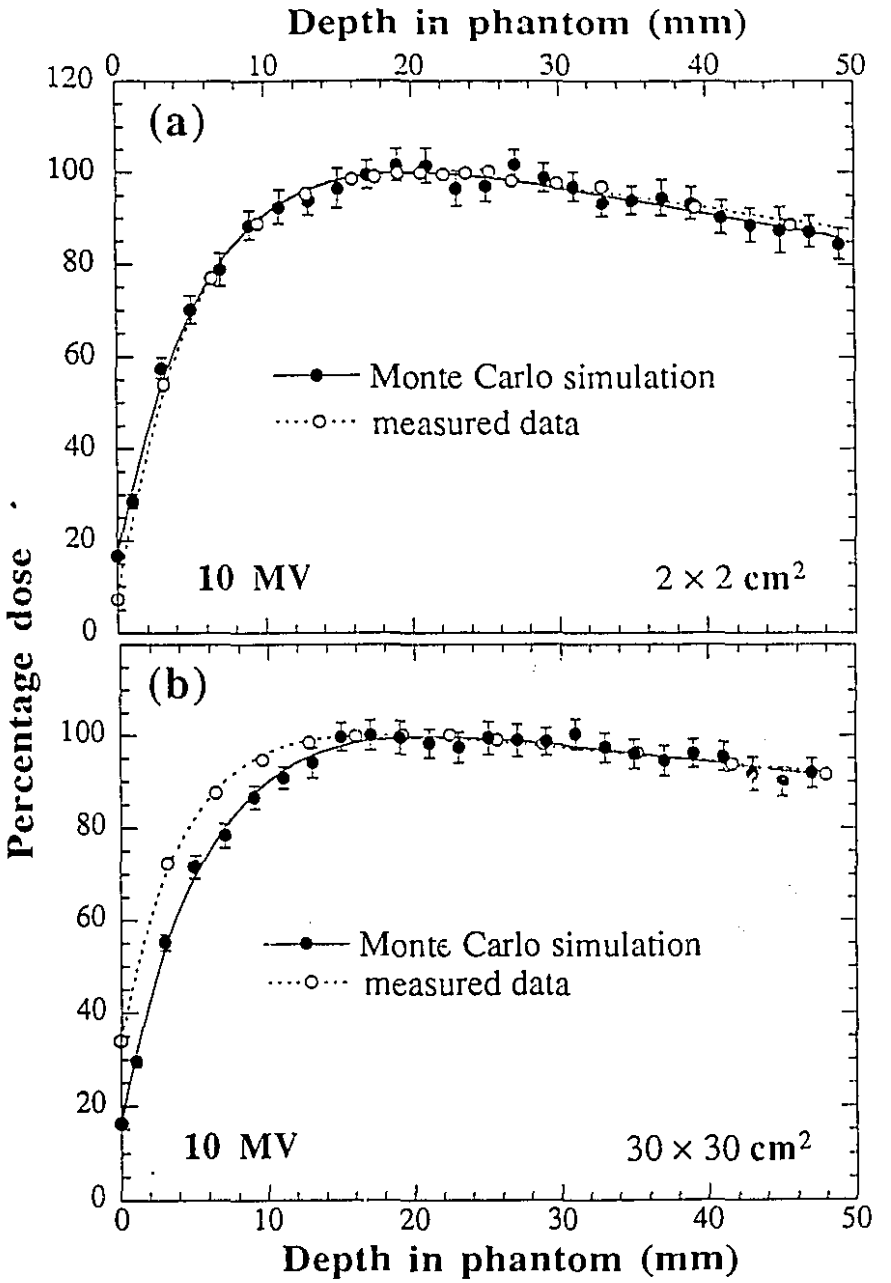

Figure 7.2 Monte Carlo simulations and measurements of percentage depth doses in the build-up region of a 10 MV x-ray beam and, in part (a) a 2x2 cm^2 field and in part (b) a 30x30 cm^2 field. Measured and calculated data points are represented by open and solid circles, respectively.

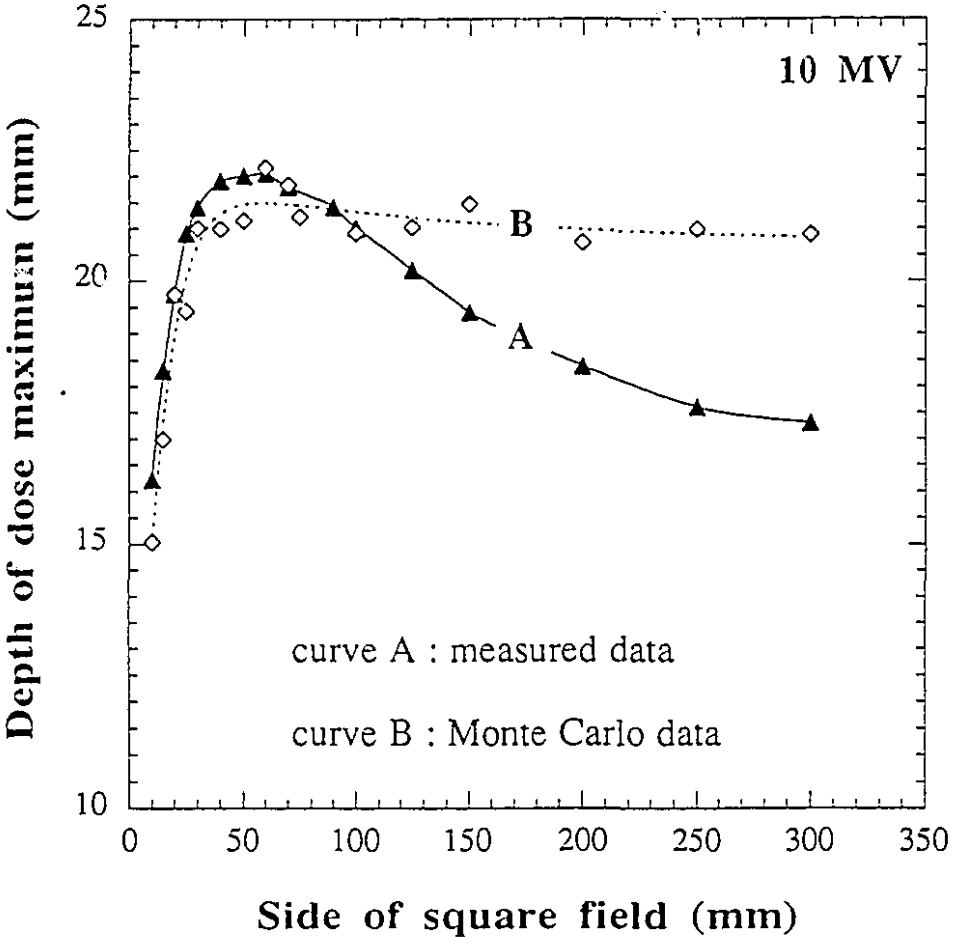

Figure 7.3 Depth of dose maximum as a function of field size for a 10 MV x-ray beam: curve A represents measured data and curve B results from Monte Carlo calculations accounting for phantom scatter but ignoring electron scatter from the flattening filter, collimator and air.

not account for scatter from the machine head. At small field sizes, where head scatter reaching the phantom is negligible, the Monte Carlo calculated d_{max} accurately predicts the measured data. At large field sizes, on the other hand, head scatter may contribute a substantial amount to the dose in the build-up region and the Monte Carlo calculation, which ignores head scatter, no longer agrees with measured data.

7.3 Head scatter contamination at large field sizes

7.3.1 *MEASUREMENT OF THE HEAD SCATTER CONTAMINATION*

To account experimentally for the difference in d_{max} between measured and calculated data at large field sizes, we devised a technique whereby the contaminants which soften the photon beam at large field sizes could be measured with a beam blocking technique and thus subtracted from the total measured dose. This technique is similar to the approach used by Krithivas and Rao (12) who used asymetric jaws in a linear accelerator to block half the primary beam, allowing them to measure electron contamination and phantom scatter.

Figure 7.4 shows schematically the experimental set-up used in our measurements of the head scatter component. Part (a) represents the machine head with an open radiation beam. The diagram traces incident photons from the x-ray target, through the flattening filter and the transmission ionization chamber, past the collimator jaws and to the ionization chamber in a polystyrene phantom at a source-surface distance

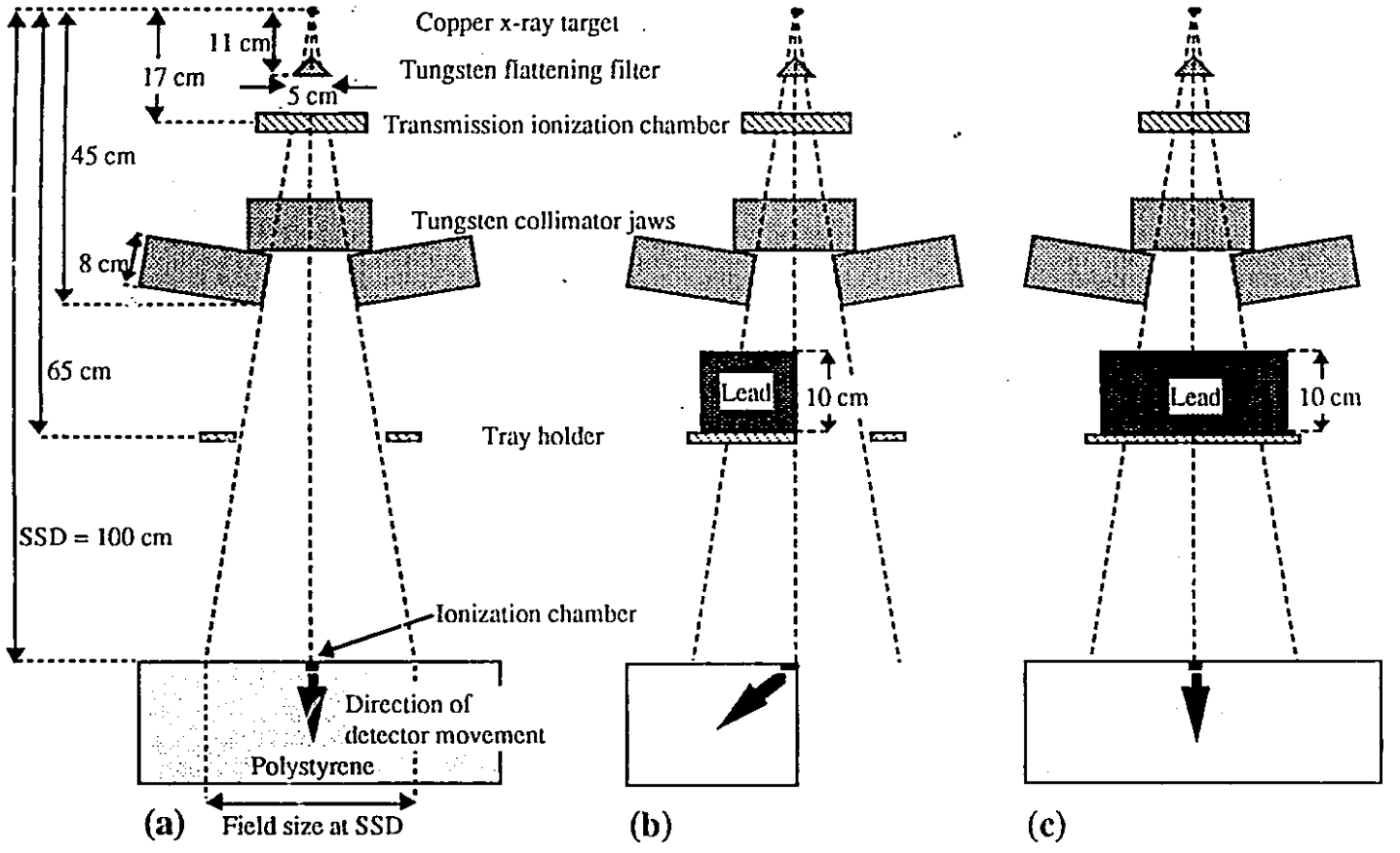

Figure 7.4 Schematic representation of the experimental set-up used to measured dose in the build-up region. Part (a) shows the set-up for the open beam, part (b) shows the set-up used to measure the scatter dose from the machine head with the half block in place, and part (c) shows the set-up used to measure the primary transmission through the 10 cm lead block.

(SSD) of 100 cm. The charge collected by the ionization chamber is due to primary photons, electron and/or photon machine head scatter and phantom scatter.

In part (b) of Fig. 7.4, we show the set-up used to eliminate the charge collected due to primary photons and phantom scatter from the signal read by the ionization chamber. A 10 cm thick lead block large enough to block half of the open beam is placed at the level of the linac accessories tray holder. The detector is placed in polystyrene phantom at an SSD of 100 cm. Half of the primary beam passes through air, avoiding the phantom completely, while the other half is attenuated by the lead block. Thus the primary x-ray beam generates no signal in the ionization chamber and the only radiation that can reach the detector is that transmitted through the half-block or scattered in the collimator jaws or in the volume of air irradiated by one half of the primary beam. To measure the dose from this scatter component as a function of depth in phantom, the detector was moved diagonally through the phantom as indicated in the figure. Any radiation reaching the detector would then have travelled through the given depth in phantom, even if it had scattered sideways in from the edge of the phantom.

Finally, to account for the primary transmission through the lead half block in Fig. 7.4(b), the full field was blocked with 10 cm thick lead and the resulting transmitted radiation was measured as a function of depth in the polystyrene phantom. This set-up is shown schematically in Fig. 7.4(c).

In Fig. 7.5 we show the method we used to determine the total head scatter for a 30x30 cm^2 open 10 MV field from the measurements with the experimental set-ups of Fig. 7.4(b) and (c). All depth dose data are expressed in the form: charge collected per linac monitor unit *vs* the depth

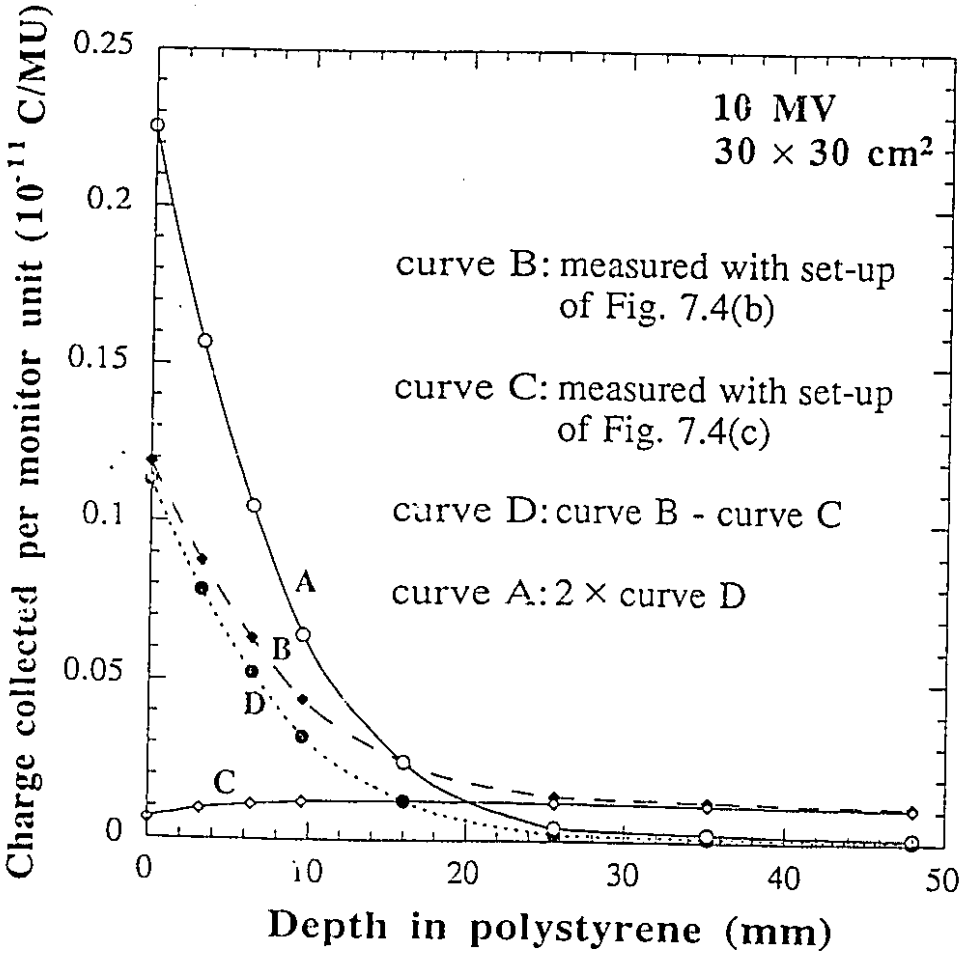

Figure 7.5 Technique used to obtain the total head scatter from the measured data for a 10 MV, 30x30 cm^2 beam. Data are plotted in absolute units of charge collected on the measuring electrode of the ionization chamber per monitor unit as a function of depth in polystyrene phantom. Curve C represents the transmission measured with the set-up of Fig. 7.4(c), curve B represents the dose distribution measured with the set-up of Fig. 7.4(b) (scatter and transmission). Curve D represents scatter alone (curve B - curve C). Curve A represents scatter contamination of the open beam of Fig. 7.4(a) and is equal to curve D multiplied by a factor of 2.

in phantom. The half-block experiment of Fig. 7.4(b) yielded a depth dose distribution given by curve B in Fig. 7.5, while the experiment of Fig. 7.4(c), as expected, yielded a depth dose curve akin to that of the standard 10 MV x-ray beam but of much lower intensity (curve C).

Curve B of Fig. 7.5 represents the radiation scattered from the collimator jaws and air but also includes the primary radiation which is transmitted through the half-block and is represented by curve C. Curves B and C become identical for depths beyond 4 cm in polystyrene indicating that the scattered radiation component is fully absorbed by the superficial layers of the phantom.

To obtain the true scatter component for the half-block experiment of Fig. 7.4(b) we subtract in Fig. 7.5 curve C from curve B to obtain curve D which represents the scatter component for half of the regular open field of Fig. 7.4(a). Thus to obtain the total scatter component for the open 30×30 cm^2 field we multiply the ordinates of curve D by a factor of 2 resulting in curve A.

7.3.2 *NATURE OF THE HEAD SCATTER CONTAMINATION*

From the particular shape of curve A in Fig. 7.5 we can deduce that the scattered radiation is of relatively low energy, we cannot say, however, whether we are dealing with electrons or superficial x-rays, as both radiations could give us similar dose distributions. This is shown in Fig. 7.6(a) where we compare curve A of Fig. 7.5 with dose distributions obtained in polystyrene for 3 MeV electrons and a 50 kVp (half-value layer: 0.3 mm of aluminum) superficial x-ray beam. The 3 MeV electrons were obtained by

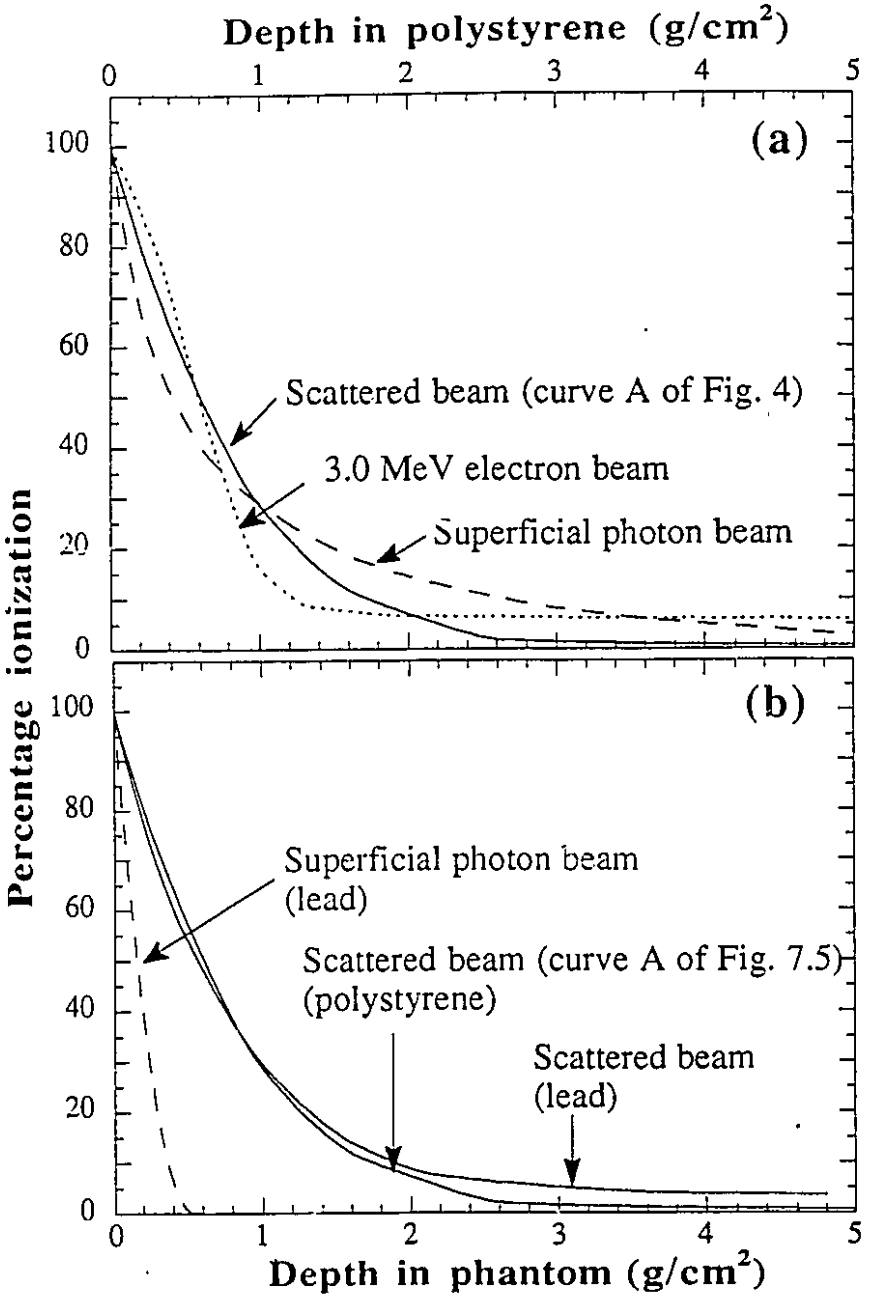

Figure 7.6 (a) Scatter contamination of the 30x30 cm^2 open 10 MV x-ray beam measured in polystyrene (curve A of Fig. 7.5 normalized to 100 on the phantom surface) compared to percentage depth doses in polystyrene of a 3 MeV electron beam and a superficial x-ray beam (50 kVp, 0.3 mm Al HVL). (b) Scatter contamination measured in polystyrene (solid curve in part (a)) compared to the scatter contamination and to the superficial x-ray beam of part (a) both measured in a lead phantom.

filtering the 9 MeV electron beam from the Clinac-18 linac with 35 mm of polystyrene. The superficial x-ray beam was obtained by filtering a 50 kVp x-ray beam with 0.32 mm of aluminum. Both the Clinac-18 and the superficial x-ray unit are described in *Chapter 2*. The three curves of Fig. 7.6(a) have the same general shape, decreasing to about 40% of the surface dose in the first 0.8 g/cm^2 of polystyrene.

However, as shown previously (1), it is relatively easy to make a distinction between low energy photon beams and electron beams by measuring depth dose distributions for the two beams in two phantoms, one of a low atomic number such as polystyrene, and the other of a high atomic number such as lead. When the two dose distributions are plotted as a function of depth in phantom in g/cm^2, an electron beam will yield essentially identical dose distributions in the two phantoms (electron density is essentially independent of atomic number), while an x-ray beam, because of the photoeffect atomic number dependence, will show a much stronger attenuation in the lead phantom compared to the polystyrene phantom.

In order to determine the nature of the scattered component of linac beams we repeated the half-blocked beam depth dose measurement of Fig. 7.4(b) in a lead phantom. The dose distribution for the scattered beam measured in lead (with the transmission through the half-block subtracted) is shown in Fig. 7.6(b). It is nearly identical to that measured in polystyrene which was shown previously as curve A in Fig. 7.5. It is therefore easy to conclude that the scatter component of the open radiation beam results from electrons scattered in the machine head and air, and that scattered photons have no effect on the build-up region of open radiation beams. The higher tail for the dose distribution measured in lead

to that measured in polystyrene is attributed to bremsstrahlung photons produced by electrons in lead. The dashed curve in Fig. 7.6(b) represents the dose distribution measured in lead with the superficial beam of Fig. 7.6(a), clearly showing the influence of the photoeffect on the attenuation of a low energy photon beam in high atomic number phantom materials.

7.3.3 *HEAD SCATTER AS A FUNCTION OF FIELD SIZE*

With the technique described above we also measured the scatter dose distributions for various smaller field sizes of the 10 MV x-ray beam and the results are shown in Fig. 7.7. As the field size decreases from 30×30 cm^2, the surface doses decrease and the scatter doses slowly diminish until at around 5×5 cm^2 they become negligible. Clearly, the megavoltage radiation beams used in radiation therapy contain an electron contamination which is negligible for small radiation fields but slowly increases with field size to reach a sizeable proportion of the total dose in the build-up region for large fields. The scatter contamination is the most pronounced on the surface and becomes negligible at depths around the nominal d_{max} of the x-ray beam, which is on the order of the range of the most energetic electrons produced by photons in the phantom material.

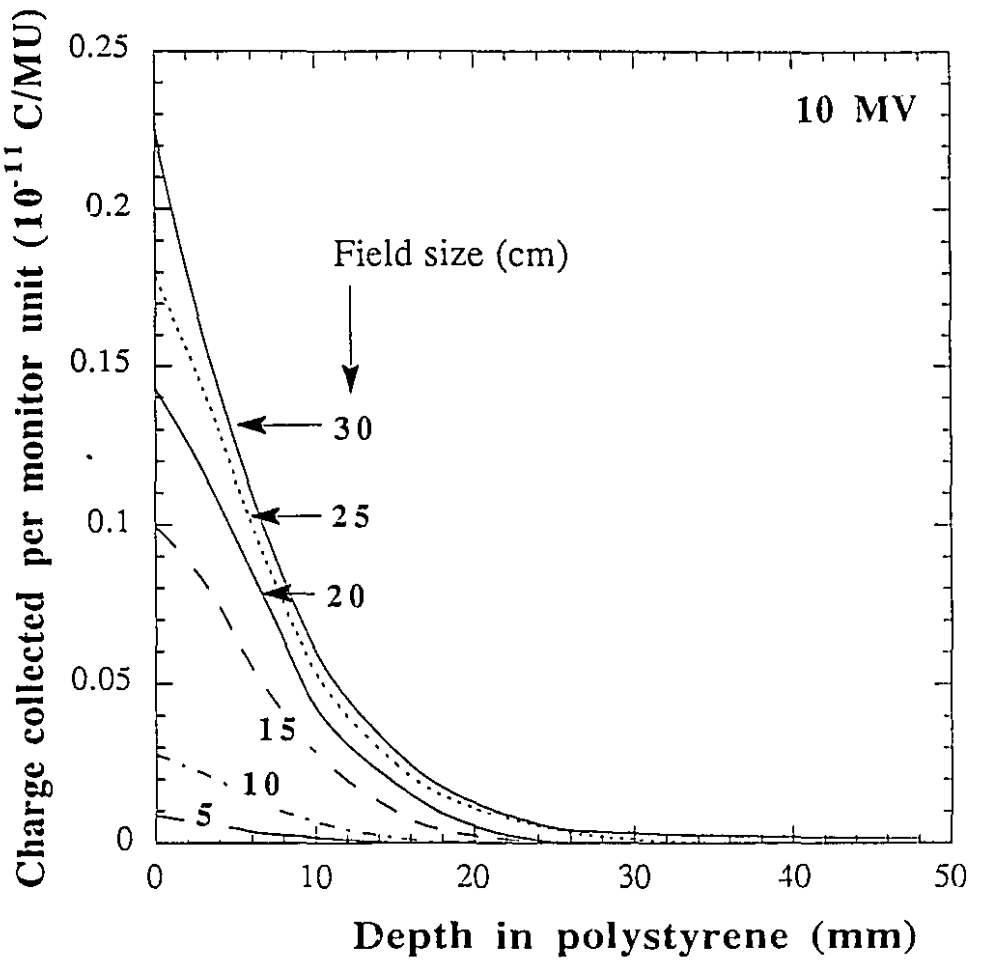

Figure 7.7 Variation of head scatter with field size for a 10 MV photon beam. Charge collected per monitor unit is plotted as a function of depth in polystyrene phantom for field sizes ranging from 5x5 cm^2 to 30x30 cm^2 in steps of 5 cm per side. Data for the 30x30 cm^2 field sizes were given as curve A in Fig. 7.5.

7.3.4 *DOSE IN THE BUILD-UP REGION WITH THE HEAD SCATTER REMOVED*

The electron scatter contamination discussed above obviously has an effect on the build-up region of megavoltage x-ray beams and, when subtracted from the total depth dose curve, will give the dose distribution of the clean photon beam affected only by primary dose and phantom scatter.

An example is given in Fig. 7.8(a) where we plot three dose distributions for a 10 MV x-ray beam and a field of 30×30 cm^2. Curve B represents the dose distribution measured with the open beam set-up of Fig. 7.4(a), curve A represents the electron scatter contamination given in Fig. 7.5, and curve C results from a subtraction of the contamination curve A from the total dose curve B. The subtraction of curve A from curve B not only lowers the absolute dose in the build-up region, it also causes a shift of d_{max} to a larger depth as indicated in Fig. 7.8(a). Since the new d_{max} is identical to that of the open 5×5 cm^2 field and the electron scatter contamination is negligible for the 5×5 cm^2 field, we conclude that this measured electron contamination is responsible for the decrease in d_{max} with increasing field size, shown in Fig. 7.1.

In Fig. 7.8(b), we compare the build-up region dose with the dose from the scattered electrons removed to the Monte Carlo simulation which was previously plotted in Fig. 7.2(b). Now, as expected, we see that there is excellent agreement between the calculated and measured data.

A subtraction of the electron contamination component from the measured depth doses for various other field sizes gives similar results to those shown in Fig. 7.8 for the 30×30 cm^2 field. However, the difference in d_{max} between the open beam and the beam with the subtracted electron

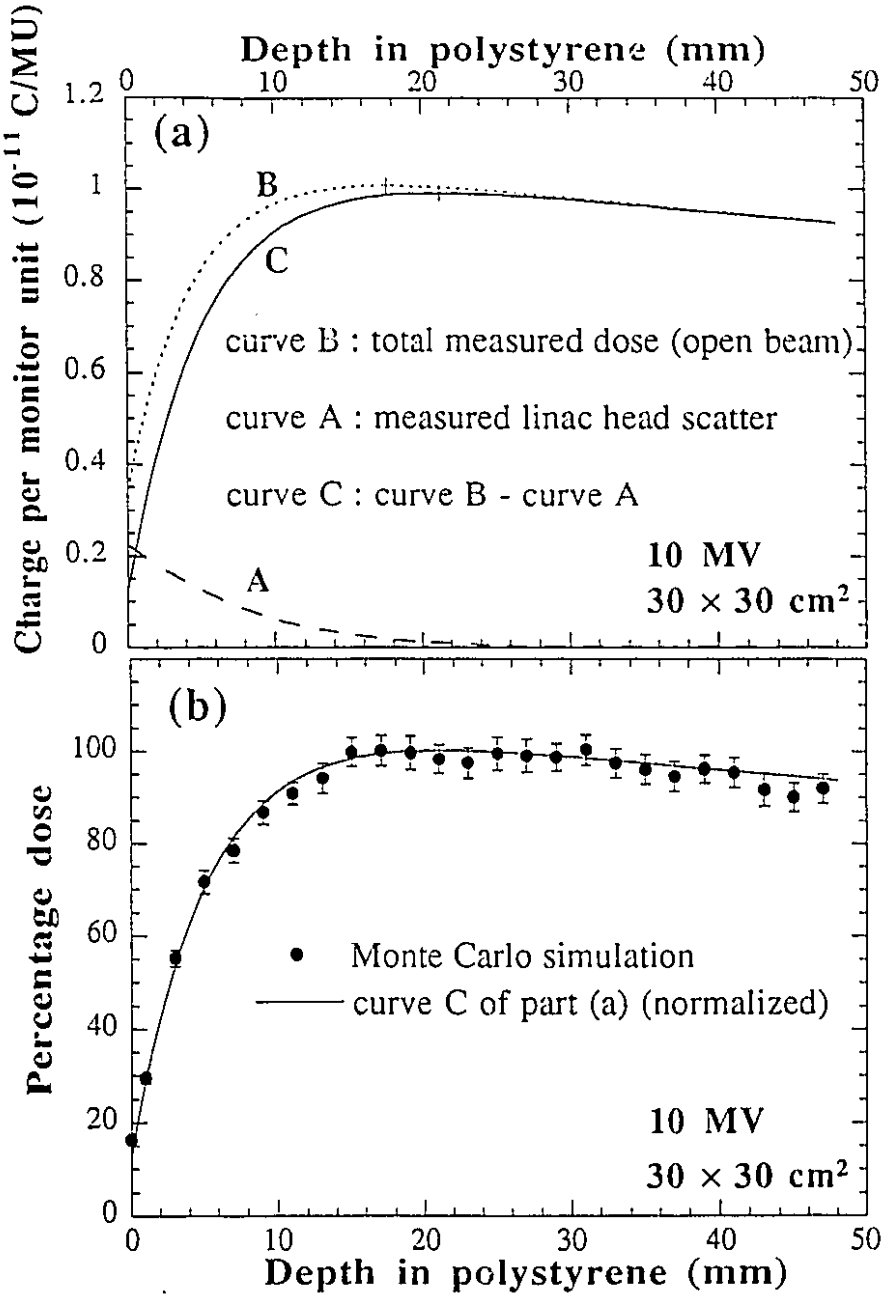

Figure 7.8 (a) Build-up region ionization data of a 30x30 cm^2 open 10 MV x-ray beam plotted as charge collected per monitor unit *vs* depth in a polystyrene phantom. Curve B represents the total depth dose, curve A represents the electron scatter component (curve A of Fig. 7.5) and curve C represents the depth dose data accounting for phantom scatter but with linac head scatter removed. The positions of d_{max} are indicated by data bars for curves B and C. (b) Comparison of Monte Carlo simulations (solid circles) of build-up region dose of the 30x30 cm^2 field and curve C of part (a) normalized to 100% at its maximum value.

contamination becomes less pronounced for smaller field sizes and it disappears for the 5×5 cm^2 field.

Once the head scatter is subtracted from the total open field dose distribution, d_{max} becomes essentially independent of field size for fields larger than 5×5 cm^2. This is shown in Fig. 7.9 with solid data points representing d_{max} values of dose distributions with head scatter effects subtracted. The solid line represents the measured d_{max} values for open radiation fields of Fig. 7.3, and the dotted line represents d_{max} data calculated with Monte Carlo techniques and also given in Fig. 7.3. The agreement between data points for head scatter removed and the Monte Carlo prediction is excellent, confirming that the decrease in d_{max} with an increasing field size is indeed caused by the machine head and air scatter of electrons.

7.3.5 *ORIGIN OF THE HEAD SCATTER*

Previous Monte Carlo studies have suggested that about 70% of the contamination electrons in a high energy x-ray beam originate in the field flattening filter (5). To study the effect of the flattening filter on d_{max} we removed the filter of our 10 MV linac and measured the depth dose curves resulting from the unflattened beam for field sizes ranging from 1×1 cm^2 to 30×30 cm^2. The measured d_{max} data are shown with open circles in Fig. 7.9. Three interesting features are noted: (i) the d_{max} values for unflattened 10 MV beams are smaller than those for the flattened beam, (ii) in the field size range from 1×1 cm^2 to 5×5 cm^2 d_{max} of unflattened beams increases with field size similarly to the behavior observed with flattened beams, and

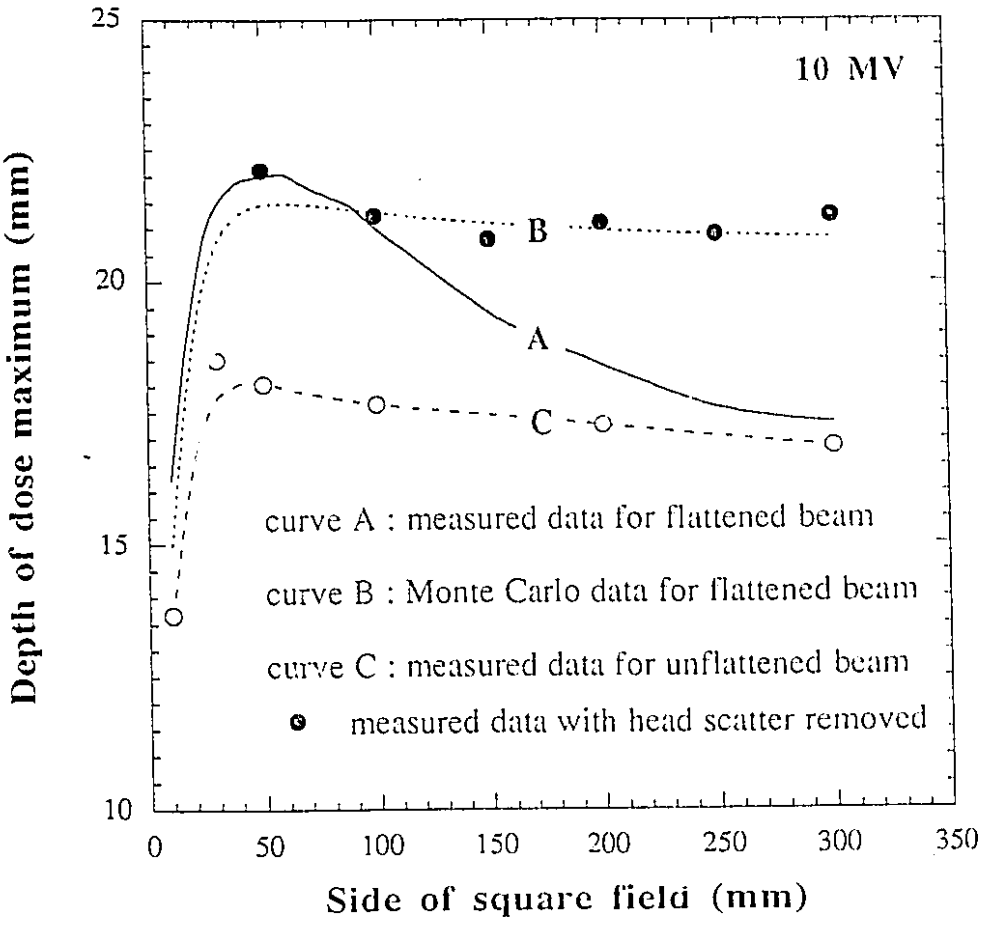

Figure 7.9 Depth of dose maximum as a function of field size for a 10 MV x-ray beam. Curves A and B are from Fig. 7.3 and represent the measured data and Monte Carlo calculations, respectively. The solid circles represent d_{max} data calculated for various field sizes for open beams with head scatter removed, as shown for the 30x30 cm^2 field in Fig. 7.8(a). The open circles (curve C) represent d_{max} data measured for the unflattened 10 MV x-ray beam.

(iii) for fields larger than 5×5 cm^2, the d_{max} of unflattened beams is independent of field size in contrast to the d_{max} of flattened beams which decreases with an increasing field size.

The higher value of d_{max} for flattened beams is attributed to beam hardening effects produced by the flattening filter on the 10 MV radiation beam. The increase in d_{max} in the field size range from 1×1 cm^2 to 5×5 cm^2 for both the flattened and unflattened beams is caused by phantom scatter which for small fields is independent of the flattening filter. For unflattened beams and field sizes larger than 5×5 cm^2 the independence of d_{max} on field size indicates that the field size dependence for flattened beams is caused solely by the insertion of the flattening filter into the radiation beam. The contamination electrons causing the d_{max} shift for flattened beam larger than 5×5 cm^2 thus all originate in the flattening filter and cause the changes in the build-up region through further scattering in the collimator or in the air.

7.5 Summary and conclusions

The depth of dose maximum of megavoltage x-ray beams is a function of beam energy and field size. For all beam energies, d_{max} increases rapidly in the field size range from 1×1 cm^2 to about 5×5 cm^2, reaches a saturation for fields around 5×5 cm^2 and then decreases gradually with an increasing field size, until at around 30×30 cm^2 it returns to a value about equal to that for a 1×1 cm^2 field. Monte Carlo calculations of d_{max} which account for phantom scatter but ignore the electron scatter from the linac head show good agreement with measurement at field sizes

smaller than 5x5 cm^2, reproducing the increase in d_{max} with increasing field size. This shift at small field sizes is caused by the primary dose deposition in the phantom, rather than by contamination of the primary beam. However, at field sizes greater than 5x5 cm^2 the Monte Carlo simulation fails to predict the decrease in d_{max} with increasing field size. This discrepancy is attributed to the fact that the Monte Carlo calculation does not consider scatter originating in the machine head during the simulation. The difference in d_{max} between measured and calculated data, and the shift observed in measured data is thus caused by head scatter from the linac.

The head scatter was measured by placing a primary beam half-block in the large radiation beams. Half of the primary beam was thus absorbed and the scattered dose originating from the other half of the primary beam was measured. When the total scattered dose is subtracted from the measured open field dose, the values obtained for d_{max} agree well with those calculated from the Monte Carlo study, and they too are independent of field size. Further experiments, comparing the attenuation in lead and in polystyrene of the scatter component, prove that the scatter contamination of the open beam consists primarily of electrons.

Measurements of dose in the build-up region with the unflattened 10 MV x-ray beam result in values of d_{max} that increase with field size for small fields but for fields larger than 5x5 cm^2 are independent of field size. Thus the contamination electrons which cause the shift in d_{max} for large flattened beams must originate in the flattening filter. However, given the geometrical conditions under which the scattered dose was measured, these electrons cannot come directly from the filter. If this was the case, these electrons would also be attenuated by the half-block set-up used to

measure the scattered dose. On the other hand, if these electrons are further scattered in the volume of irradiated air or in the collimator jaws they would be detected with the half block in place and furthermore their number would increase as the amount of scattering material increases, i.e., as field size increases. Based on our experiments we conclude that the scattered electrons which cause the decrease in depth of dose maximum with increasing field size of megavoltage x-ray beams are in fact second order scattered electrons, originating in the flattening filter and then scattered into the point of measurement on the central axis by the collimator jaws and the volume of irradiated air.

7.6 References

1. P.J. Biggs and C.C. Ling, *Electrons as the cause of the observed d_{max} shift with field size in high energy photon beams*, Med Phys. **6**: 291-295, 1979.
2. C.C. Ling, M.C. Schell and S.N. Rustgi, *Magnetic analysis of the radiation components of a 10 MV photon beam*, Med. Phys. **9**: 20-26, 1982.
3. D.M. Galbraith and J.A. Rawlinson, *Direct measurement of electron contamination in cobalt beams using a charge detector*, Med. Phys. **12**: 273-280, 1985.
4. T.R. Mackie and J.W. Scrimger, *Contamination of a 15-MV photon beam by electrons and scattered photons*, Radiol. **144**: 403-409, 1982.
5. P.L. Petti, M.S. Goodman, J.M. Sisterson, P.J. Biggs, T.A. Gabriel, R. Mohan, *Sources of electron contamination for the Clinac-35 25-MV photon beam*, Med. Phys. **10**: 856-861, 1983.
6. C.C. Ling and P.J. Biggs, *Improving the build-up and depth-dose characteristics of high energy photon beams by using electron filters*, Med. Phys. **6**: 296-301, 1979.
7. K. Parthasaradhi, S.G. Prasad, B.M. Rao, Y. Lee, R. Ruparel and R. Garces, *Investigation on the reduction of electron contamination with a 6-MV x-ray beam*, Med. Phys. **16**: 123-125, 1989.
8. P.L. Petti, M.S. Goodman, T.A. Gabriel and R. Mohan, *Investigation of build-up dose from electron contamination of clinical photon beams*, Med. Phys **10**: 18-24, 1983.
9. K.E. Sixel and E.B. Podgorsak, *Depth of dose maximum as a function of photon beam energy and field size*, (abstract) Proceedings of the

39th meeting of the Canadian Organization of Medical Physicists (COMP) and the 19th meeting of the Canadian Medical and Biological Engineering Society (CMBE), Ottawa, Ontario, May 12-15, pp. 214-215, 1993.

10. K.E. Sixel and E.B. Podgorsak, *Build-up region and depth of dose maximum of megavoltage x-ray beams as a function of field size*, Med. Phys. (in press), 1993.

11. R. Mohan, C. Chui and L. Lidofsky, *Energy and angular distributions of photons from medical linear accelerators*, Med. Phys. **12**: 592-597, 1985.

12. G. Krithivas and S.N. Rao, *A study of the characteristics of radiation contaminants within a clinically useful photon beam*, Med. Phys. **12**: 764-768, 1985.

CHAPTER 8

CONCLUSIONS

8.1 Summary

Since its inception in the 1950s, radiosurgery has generated much clinical and physical interest. With the recent advances in brain imaging and mapping, this interest has increased considerably, and the role of radiosurgery has expanded to the treatment of a wide variety of brain diseases. Radiosurgery with heavy charged particle beams was developed first, but never remained a serious competitor to x-ray techniques because of the enormous costs of purchasing, operating and maintaining a cyclotron. Historically, the gamma unit offered the first commercially available means of performing radiosurgery. However, in recent years linear accelerator-based radiosurgery has been developed in several centers, and these techniques have become widespread in use. In this thesis, we focus on radiosurgical techniques using isocentric linear accelerators.

We cover a wide variety of aspects concerning radiosurgery in general, from a physical and clinical point-of-view. Physical aspects of radiosurgery include the stereotactic frames used for target localization, patient set-up and immobilization during the treatment, computerized treatment planning systems, as well as the particular treatment techniques. The linac based techniques described are: the single plane rotation, multiple non-conplanar converging arcs (4 and 11 arcs), dynamic rotation and conical rotation.

We also briefly discuss the principles of the gamma unit and heavy charged particle radiosurgery. The clinical aspects of radiosurgery described here consist of the clinical goals and considerations that must be met by a radiosurgical treatment, the diseases responsive to radiosurgery

and an understanding of the complication rates associated with radiosurgery.

The most recent interest in radiosurgery has focussed on obtaining non-spherical dose distributions. We derive a method whereby the rotation of a rectangular collimator and adjustment of its longitudinal opening during the paths followed by the couch and gantry results in a superposition of rectangular fields at the target volume. A cylindrical dose distribution is then obtained during the rotation of the gantry. The equations governing collimator rotation and longitudinal opening are functions of the gantry angle, couch angle and the target longitudinal axis coordinates in a frame of reference which is stationary with the couch. For a given target orientation and size, and for each couch and gantry position, the necessary collimator rotation and longitudinal field size are calculated. The lateral collimator field size is set to the projection of the diameter of the target cylinder in the couch plane. Measurements of dose distributions obtained with the cylindrical dynamic rotation show that we can shape high level isodose surfaces with this technique, resulting in considerable dose savings to healthy tissue if the clinical target is in fact better approximated by a cylinder than by a sphere.

The beam data needed for radiosurgical treatment planning consists of beam profiles, percentage depth dose curves and scatter correction factors. Measurements and Monte Carlo simulations are used as tools to understand the radiosurgical beams as a function of beam energy and field size. Measurements of beam profiles show that the physical collimator size and geometrical beam divergence determine the off-axis ratios. Beam energy plays only a minor role. Percentage depth doses, on the other hand, become more penetrating with increasing beam energy and increasing

field size. The measurements of radiosurgical percentage depth doses show that the depth of dose maximum increases with increasing field size. Monte Carlo simulations confirm this finding and are used to understand the shift in the depth of dose maximum. The Monte Carlo calculations indicate that the primary dose deposition in the phantom, not phantom or collimator scatter, governs the depth of dose maximum. This is in agreement with measured collimator scatter correction factors which remain independent of field size for a given beam energy in the beam diameter range from 10 mm to 30 mm.

The small scatter component of the radiosurgical beams allows the percentage depth dose data to be represented by a simple bi-exponential function. Furthermore, the four bi-exponential fitting parameters change in a monotonic fashion with field size for a given beam energy and these parameters can be described by a 2nd order polynomial. Thus an analytical representation was developed to generate radiosurgical percentage depth dose data at arbitrary depths and field sizes for 6 MV, 10 MV and 18 MV x-ray beams. With this formalism, 94% of calculated percentage depth dose data points are reproduced within ±1% of the corresponding measured values.

It is well known that the depth of dose maximum decreases with increasing field size for large radiotherapy fields. Within this context, the increase in depth of dose maximum with increasing radiosurgical field size was unexpected. To generalize this finding, the build-up region dose was measured for a complete range of field sizes and beam energies: from 1x1 cm^2 field to a 30x30 cm^2 field for 6 MV, 10 MV and 18 MV x-ray beams. For all beam energies, the depth of dose maximum increases rapidly in the field size range from 1x1 cm^2 to 5x5 cm^2, reaches a saturation for fields

around 5×5 cm^2 and then gradually decreases with increasing field size. The two shifts observed are very different in nature. Monte Carlo studies show that at small field sizes, primary dose deposition in the phantom determines the depth of dose maximum. At large field sizes, scatter from the linac head softens the x-ray beam and causes the depth of dose maximum to shift forward. This scatter consists mainly of electrons originating in the field flattening filter. Subtraction of the scattered dose from the total dose results in the depth of dose maximum becoming independent of field size at large field dimensions, and in good agreement with Monte Carlo calculations of dose in the build-up region of large fields. These calculations do not account for machine head scatter. The technique used to measure the head scatter component suggests that the scattered electrons which cause the decrease in depth of dose maximum with increasing field size at large fields are in fact second order scattered electrons originating in the flattening filter and then scattered into the central axis by the collimator jaws and the volume of irradiated air.

8.2 Future work

Clinical radiosurgery has been in practice for many years now, including over a decade of experience with linac-based techniques. As a result, many of the technical and physical aspects of radiosurgery are well known. Once proper detectors and techniques are chosen, the measurement of radiosurgical beam parameters becomes straightforward, and with the help of Monte Carlo simulations, the behaviour of these beams can be understood. Similarly, at large field sizes, the characteristics of dose

deposition can be understood if suitable experimental techniques in the form of measurements and Monte Carlo calculations are applied. In particular, a complete Monte Carlo simulation of the x-ray beam accounting for all components in the linac head, including flattening filter, ionization chamber and collimator jaws, would allow the calculation of the electron contamination at large field sizes, for comparison with the measured electron contamination component.

In the future, we propose that the analytical representation of radiosurgical percentage depth dose data be implemented in treatment planning programs. The method allows for compact and accurate beam data, and overcomes limitations, such as an inaccurate approximation of the depth of dose maximum. Our preliminary tests have shown that the use of parametrized percentage depth dose data for dose distribution calculations saves both time and computer storage space.

Much current work in radiosurgery has gone into the development of techniques to irradiate non-spherical radiosurgical treatment volumes. Most of the proposed methods, including the one presented in this thesis, are at an experimental stage. The largest obstacles preventing routine clinical use of the cylindrical dynamic rotation technique is the lack of remote computer control over the collimator rotation and opening, and the lack of a treatment planning system that can calculate cylindrical dose distributions with arbitrary field parameters for a target of arbitrary orientation within the brain.

The equations governing collimator opening and rotation are quite complex, and greater operator control over the collimator movement would be needed to allow for a continuous irradiation. Furthermore, the question of beam penumbra must be addressed. The additional collimators of

spherical radiosurgery ensure that the beam penumbra is kept to a minimum, and thus make sharp dose fall-offs easier to achieve. If the machine collimator does not meet the criteria of accurately defined fields and a sharp beam penumbra, additional adjustable rectangular collimators may have to be considered. With the advent of miniature multileaf collimators on some newer linac models, these considerations may be addressed. These miniature collimators resemble the multileaf collimators used in large field conformal radiotherapy, but have leaf widths on the order of 1 mm, making them useful for field sizes up to 4x4 cm^2.

BIBLIOGRAPHY

Arcovito G., Piermattei A., D'Abramo G. and Bassi F.A., *Dose measurements and calculations of small radiation fields for 9-MV x rays*, Med. Phys. 12: 779-784, 1985. (103)

Austin-Seymour M., Munzenrider J., Linggood R., Goitein M., Verhey L., Urie M., Gentry R., Birnbaum S., Ruotolo D., Crowell C., McManus P. and Suit H.D., *Fractionated proton radiation therapy of cranial and intracranial tumours*, Am. J. Clin. Oncol. **13**: 327-330, 1990. (23)

Berger M.J. and Seltzer S.M., *ETRAN, Monte Carlo code system for electron and photon transport through extended media*, Documentation for RSIC Computer dose package CCC-107, Oak Ridge Nat. Lab., Oak Ridge, Tennessee, 1973. (66)

Berger M.J. and Seltzer S.M., *Stopping powers and ranges of electrons and positrons*, NBS Report NBSIR 82-2550-A, 1983. (67)

Betti O.O. and Derchinsky V.E., *Hyperselective encephalic irradiation with linear accelerator*, Acta Neurochir. **33**: 385-390, 1984. (4,16)

Bielajew A.F. and Rogers D.W.O., *Variance reduction techniques*, in: Monte Carlo transport of electrons and photons, T.M. Jenkins, W.R. Nelson and A. Rindi (eds.), Plenum Publishing Co., New York, 1987, pp. 407-419. (72)

Bielajew A.F. and Rogers D.W.O., *PRESTA: The parameter reduced electron-step transport algorithm for electron Monte Carlo transport*, Nuc. Instr. Meth. Phys. Res. **B18**: 165-181, 1987. (72)

Biggs P.J. and Ling C.C., *Electrons as the cause of the observed d_{max} shift with field size in high energy photon beams*, Med. Phys. **6**: 291-295, 1979. (113,144,145,160)

Bjärngard B.E., Tsai J.-S. and Rice R.K., *Doses on the central axis of narrow 6-MV x-ray beams*, Med. Phys. **17**: 794-799, 1990. (103)

Brahme A. and Svensson H., *Radiation beam characteristics of a 22 MeV microtron*, Acta. Radiol. Oncol. **18**: 244-270, 1979. (129)

Brown R.D., Wiebers D.O., Forbes G., O'Fallon W.M., Piepgras D.G., Marsh W.R. and Maciunas R.J., *The natural history of unruptured intracranial arteriovenous malformations,* J. Neurosurg. **68**: 352-357, 1988. (25)

Chen G.T.Y., *Dose volume histograms in treatment planning*, Int. J. Radiat. Oncol. Biol. Phys. **14**:1319-1320, 1988. (21)

Chierego G., Marchetti C., Avanzo R.C., Pozza F. and Colombo F., *Dosimetric considerations on multiple arc stereotaxic radiotherapy*, Radio. and Onco. **12**: 141-152, 1988. (116)

Clark B.G., Podgorsak E.B., Souhami L., Olivier A., Sixel K.E. and Caron J.-L., *A halo-ring technique for fractionated stereotactic radiotherapy*, Brit. J. Radiol. **66**: 522-527, 1993. (23)

Colombo F., Benedetti A., Pozza F., Avanzo R.C., Marchetti C., Chierego C. and Zanardo A., *External stereotactic irradiation by linear accelerator*, Neurosurg. **16**:154-160, 1985. (6,16)

Curry T.S., Dowdey J.E. and Murry R C., *Christensen's introduction to the physics of diagnostic radiology*, 3rd edition, Lea & Febiger, Philadelphia, Chap. 10, 1984. (56)

Dahlin H. and Sarby B., *Destruction of small intracranial tumours with ^{60}Co gamma irradiation*, Acta Radiol. TPB **14**: 209-227, 1975. (10,12)

Dutreix J., Dutreix A. and Tubiana M., *Electronic equilibrium and transition stages*, Phys. Med. Biol. **10**: 177-190, 1965. (103)

Flickinger J.C., *An integrated logistic formula for prediction of complications from radiosurgery*, Int. J. Radiat. Oncol. Biol. Phys. **17**: 879-885, 1989. (21)

Flickinger J.C., Lunsford L.D., Coffey R.J., Linskey M.E., Bissonette D.J., Maitz A.H. and Kondziolka D., *Radiosurgery of acoustic neurinomas*, Cancer **67**: 345-353, 1991. (30)

Flickinger J.C., Lunsford L.D., Wu A., Maitz A.H., Kalend A.M., *Treatment planning for gamma knife radiosurgery with multiple isocenters*, Int. J. Radiat. Oncol. Biol. Phys. **18**: 1495-1501, 1990. (78)

Flickinger J.C., Maitz A., Kalend A., Lunsford L.D. and Wu A., *Treatment volume shaping with selective beam blocking using the Leksell gamma unit*, Int. J. Radiat. Oncol. Biol. Phys. **19**: 783-789, 1990. (22,78)

Galbraith D.M. and Rawlinson J.A., *Direct measurement of electron contamination in cobalt beams using a charge detector*, Med. Phys. **12**: 273-280, 1985. (145)

Goldstein H., *Classical Mechanics*, 2nd edition, Addison-Wesley Publishing Co. Inc. Reading Massachusetts, 1980. (83)

Graham J.D., Nahum A.E. and Brada M., *A comparison of techniques for stereotactic radiotherapy by linear accelerator based on 3-dimensional dose distributions*, Radio. Oncol. **22**: 29-53, 1991. (20)

Griffin B.R., Warcola S.H., Mayberg M.R., Eenmaa J., Eskridge J. and Winn H.R., *Stereotactic neutron radiosurgery for arteriovenous malformations of the brain,*. Med. Dosimetry **13**: 179-182, 1988. (4)

Hartmann G.H., Schlegel W., Sturm V., Kober B., Pastyr O. and Lorenz W.J., *Cerebral radiation surgery using moving field irradiation at a linear accelerator facility*, Int. J. Radiat. Oncol. Biol. Phys. **11**: 1185-1192, 1985. (4,16)

Houdek P.V., Fayos J.V., Van Buren J.M. and Ginsberg M.S., *Stereotaxic radiotherapy technique for small intracranial lesions*, Med. Phys. **12**: 469-472, 1985. (4,14)

Houdek P.V., Van Buren J.M. and Fayos J.V., *Dosimetry of small radiation field for 10-MV x rays*, Med. Phys. **10**: 333-336, 1983. (103)

ICRU Report #37, *Stopping powers for electrons and positrons*, ICRU, Washington DC, 1984. (67)

Johns H.E. and Cunningham J.R., *The physics of radiology*, 4th edition, Charles C. Thomas, Springfield, Illinois, 1983. (59,109)

Johns H.E., Darby E.K., Haslam R.N.H., Katz L. and Harrington E.L., *Depth dose data and isodose distributions for radiation from a 22 MeV betatron*, Am. J. Roentgenol. **62**: 257-268, 1949. (129)

Karzmark C.J. and Morton R.J., *A primer on theory and operation of linear accelerators in radiation therapy*, U.S. Department of Health and Human Services, Food and Drug Administration, Bureau of Radiological Health, Rockville, Maryland, 1981. (45)

Khan F.M., Sewchand W., Lee J. and Williamson J.F., *Revision of tissue-maximum-ratio and scatter-maximum-ratio concepts for cobalt-60 and higher energy x-ray beams*, Med. Phys. **7**: 230-237, 1980. (111)

Kjellberg R.N., Davis K.R., Lyons S., Butler W. and Adams R.D., *Bragg peak proton beam therapy for arteriovenous malformations of the brain*, Clin. Neurosurg **31**: 248-290, 1983. (29)

Kjellberg R.N., Sintani A., Frantz A.G. and Kliman B., *Proton beam therapy in acromegaly*, N. Engl. J. Med. **278**: 689-695, 1968. (3,9,28)

Krithivas G. and Rao S.N., *A study of the characteristics of radiation contaminants within a clinically useful photon beam*, Med. Phys. **12**: 764-768, 1985. (154)

Larsson B., Leksell L., Rexed B., Sourander P., Mair W. and Anderson B., *The high energy proton beam as a neurosurgical tool*, Nature **182**: 1222-1223, 1958. (3,7)

Larsson B., Liden K. and Sarby B., *Irradiation of small structures through intact skull*, Acta Radiol. TPB **13**:513-534, 1974. (4)

Lawrence J.H., Tobias C.A., Born J.L., Wang C. and Linfoot J.A., *Heavy-particle irradiation in neoplastic and neurologic disease*, J. Neurosurg. **19**: 717-722, 1962. (3,7)

Leavitt D.D., Gibbs F.A., Heilbrun M.P., Moeller J.H. and Takach G.A., *Dynamic field shaping to optimize stereotactic radiosurgery*, Int. J. Radiat. Oncol. Biol. Phys. **21**: 1247-1255, 1991. (78,79)

Leksell L., *The stereotaxis method and radiosurgery of the brain*, Acta Chir. Scan. **102**: 316-319, 1951. (3)

Leksell L., *Gezielte Hirnoperationen*, in: Handbuch der Neurochirurgie, H. Olivecrona and W. Tonnis (eds), Springer Verlag, New York, 1957, pp. 178-218. (3)

Leksell L., *Cerebral radiosurgery I Gamma thalamotomy in two cases of intractable pain*, Acta Chir. Scan. **134**: 385-395, 1968. (3,4)

Ling C.C. and Biggs P.J., *Improving the build-up and depth-dose characteristics of high energy photon beams by using electron filters*, Med. Phys. **6**: 296-301, 1979. (145)

Ling C.C., Schell M.C. and Rustgi S.N., *Magnetic analysis of the radiation components of a 10 MV photon beam*, Med. Phys. **9**: 20-26, 1982. (144)

Lutz W., Winston K.R. and Maleki N., *A system for stereotactic radiosurgery with a linear accelerator*, Int. J. Radiat. Oncol. Biol. Phys. **14**: 373-381, 1988. (16)

Luxton G. and Jozsef G., *Dosimetric considerations in linac radiosurgery treatment planning of off-center and elongated targets* (abstract), Int. J. Radiat. Oncol. Biol. Phys. **19** Suppl. 1: 262, 1990. (79)

Luxton G., Jozsef G. and Astrahan M.A., *Algorithm for dosimetry of multiarc linear-accelerator stereotactic radiosurgery*, Med. Phys. **18**: 1211-1221, 1991. (127)

Lyman J.T. and Howard J., *Dosimetry and instrumentation for helium and heavy ions*, Int. J. Radiat. Oncol. Biol. Phys. **3**: 81-85, 1977. (4)

Lyman J.T., Kanstein L., Yeater F., Fabrikant J.I. and Frankel K.A., *A helium-ion beam for stereotactic radiosurgery of central nervous system disorders*, Med. Phys. **13**: 695-699, 1986. (4)

Mackie T.R. and Scrimger J.W., *Contamination of a 15-MV photon beam by electrons and scattered photons*, Radiol. **144**: 403-409, 1982. (145)

Maleki N., Lutz W. and DeWyngaert K., *Parameter specification for two-isocenter-technique in radiosurgery* (abstract), Med. Phys. **16**: 461, 1989. (78)

Marquardt D.W., *An algorithm for least squares estimation of nonlinear parameter*, J. Soc. Ind. App. Math. **2**: 431-441, 1963. (128)

McGinley P.H., Butker E.K., Crocker I.R. and Aiken R., *An adjustable collimator for stereotactic radiosurgery*, Phys. Med. Biol. **37:** 413-419, 1992. (79)

McGinley P.H., Butker E.K., Crodker I.R. and Landry J.C., *A patient rotator for stereotactic radiosurgery*, Phys. Med. Biol. **35**:649-657, 1990. (17)

McKenzie M.R., Souhami L., Podgorsak E.B., Olivier A., Caron J.-L. and Villemure J.-G., *Photon radiosurgery: a clinical review*, Can. J. Neurol. Sci. **19**: 212-221, 1992. (23,26,27,28)

Mohan R., Chui C. and Lidofsky L., *Energy and angular distributions of photons from medical linear accelerators*, Med. Phys. **12**: 592-597, 1985. (116, 150)

Nelson W.R., Hirayama H. and Rogers D.W.O., *The EGS4 code system*, SLAC report 265, Stanford Linear Accelerator Center, Stanford, California, 1985. (66,68,69,74)

Norén G., Arndt J., Hindmarsh T. and Hirsch A., *Stereotactic radiosurgical treatment of acoustic neurinomas*, in: Modern Stereotactic Neurosurgery, L.D. Lunsford (ed.), Martinus Nijhoff, Boston, 1988, pp. 481-489. (30)

Parthasaradhi K., Prasad S.G., Rao B.M., Lee Y., Ruparel R. and Garces R., *Investigation on the reduction of electron contamination with a 6-MV x-ray beam*, Med. Phys. **16**:123-125, 1989. (145)

Phillips M.H., Frankel K.A., Lyman J.T., Fabrikant J.I. and Levy R.P, *Comparison of different radiation types and irradiation geometries in stereotactic radiosurgery*, Int. J. Radiat. Oncol. Biol. Phys. **18**: 211-220, 1990. (20)

Peters T.M., Clark J.A., Olivier A., Marchand A.P., Mawko G., Dieumegarde M., Muresan L.V. and Ethier R., *Integrated stereotaxic imaging with CT, MR imaging and Digital Subtraction Angiography*, Radiol. **161**: 821-826, 1986. (5,6)

Petti P.L., Goodman M.S., Gabriel T.A. and Mohan R., *Investigation of build-up dose from electron contamination of clinical photon beams*, Med. Phys **10**: 18-24, 1983. (145)

Petti P.L., Goodman M.S., Sisterson J.M., Biggs P.J., Gabriel T.A., Mohan R., *Sources of electron contamination for the Clinac-35 25-MV photon beam*, Med. Phys. **10**: 856-861, 1983. (145,146,166)

Pike G.B., Podgorsak E.B., Peters T.M. and Pla C., *Dose distributions in dynamic stereotactic radiosurgery*, Med. Phys. **14**: 780-789, 1987. (127)

Pla C., Sixel K.E. and Podgorsak E.B., *Calculation of cylindrical isodose distributions in stereotactic radiosurgery*, (abstract) Med. Phys. **19**: 843, 1992. (21)

Pla C., Sixel K.E. and Podgorsak E.B., *Cylindrical versus multiple isodose isodose distributions in stereotactic radiosurgery*, (abstract) Proceedings of the 39th meeting of the Canadian Organization of Medical Physicists (COMP) and the 19th meeting of the Canadian Medical and Biological Engineering Society (CMBE), Ottawa, Ontario, May 12-15, pp. 260-261, 1993. (21)

Podgorsak E.B., *Physics for radiosurgery with linear accelerators*, Neurosurg. Clin. North Amer. **3**: 9-34, 1992. (2,10,14,127)

Podgorsak E.B., Olivier A., Pla M., Hazel J., de Lotbinière A. and Pike B., *Physical aspects of dynamic stereotactic radiosurgery*, Appl. Neurophysiol. **50**: 63-68, 1987. (17)

Podgorsak E.B., Olivier A., Pla M., Lefebvre P.Y. and Hazel J., *Dynamic stereotactic radiosurgery*, Int. J. Radiat. Oncol. Biol. Phys. **14**: 115-125, 1988. (17,23)

Podgorsak E.B., Pike G.B., Olivier A., Pla M. and Souhami L., *Radiosurgery with high energy photon beams: a comparison among techniques*, Int. J. Radiat. Oncol. Biol. Phys. **16**: 857-865, 1989. (97)

Podgorsak E.B., Souhami L., Caron J.-L., Pla M., Clark B., Pla C. and Cadman P., *A technique for fractionated stereotactic radiotherapy in the treatment of intracranial tumours*, Int. J. Radiat. Oncol. Biol. Phys. (in press) 1993. (24)

Pozza F., Colombo F., Chierego G., Avanzo R.C., Marchetti C., Benedetti A., Casentini L. and Pisciotta V.J., *Low grade astrocytomas: treatment with unconventionally fractionated external beam stereotactic radiation therapy*, Radiol. **171**: 565-569, 1989. (23)

Rice R.K., Hansen J.L., Svensson G.K. and Siddon R.L., *Measurements of dose distributions in small beams of 6-MV x rays*, Phys. Med. Biol. **32**: 1087-1099, 1987. (103,127)

Rogers D.W.O. and Bielajew A.F., *Monte Carlo techniques of electron and photon transport for radiation dosimetry*, in: The dosimetry of ionizing radiation, vol. III, K.R. Kase, B.E. Bjärngard and F.H. Attix (eds.), Academic Press, San Diego, California, 1990, pp. 427-540. (66)

Schell M.C., Smith V., Larson D.A., Wu A. and Flickinger J.C., *Evaluation of radiosurgery techniques with cumulative dose volume histograms in linac-based stereotactic external beam irradiation*, Int. J. Radiat. Oncol. Biol. Phys. **20**: 1325-1330, 1991. (20)

Schwade J.G., Houdek P.V., Landy H.J., Bujnoski J.L., Lewin A.A., Abitol A.A., Serago C.F. and Pisciotta V.J., *Small field stereotactic external beam radiation therapy of intracranial lesions: fractionated treatment with a fixed-halo immobilization*, Radiol. **176**: 563-565, 1990. (23)

Serago C.F., Houdek P.V., Bauer-Kirpes B., Lewin A.A., Abitbol A.A., Gonzales-Arias S., Marcial-Vega V.A. and Schwade J.G., *Stereotactic radiosurgery: Dose-volume analysis of linear accelerator techniques*, Med. Phys. **19**: 181-185, 1992. (20)

Serago C.F., Houdek P.V., Hartmann G.H., Saini D.S., Serago M.E.. and Kaydee A., *Tissue maximum ratios (and other parameters) of small circular 4, 6, 15 and 24 MV x-ray beams for radiosurgery*, Phys. Med. Biol. **37**:1943-1956, 1992. (127)

Serago C., Lewin A., Houdek P., Abitol A., Gonzales-Arias S., Pisciotti V. and Schwade J., *Improved linac dose distributions for radiosurgery with irregularly shaped fields*, Int. J. Radiat. Oncol. Biol. Phys. **21**: 1321-1325, 1991. (79)

Sixel K.E., *Physical parameters of narrow photon beams in radiosurgery*, M.Sc. thesis, McGill University, 1990. (13,79,103,104,122)

Sixel K.E. and Podgorsak E.B., *Cylindrical dose distributions in dynamic rotation radiosurgery*, (abstract) Med. Phys. **18**:621, 1991. (79)

Sixel K.E. and Podgorsak E.B., *Build-up region of high energy photon beams in radiosurgery*, (abstract) Med. Phys. **19**: 843, 1992. (103)

Sixel K.E. and Podgorsak E.B., *Depth of dose maximum as a function of photon beam energy and field size*, (abstract) Proceedings of the 39th meeting of the Canadian Organization of Medical Physicists (COMP) and the 19th meeting of the Canadian Medical and Biological Engineering Society (CMBE), Ottawa, Ontario, May 12-15, pp. 214-215, 1993. (146)

Sixel K.E. and Podgorsak E.B., *Build-up region of high energy x-ray beams in radiosurgery*, Med. Phys. **20**: 761-764, 1993. (103)

Sixel K.E. and Podgorsak E.B., *Build-up region and depth of dose maximum of megavoltage x-ray beams as a function of field size*, Med. Phys. (in press), 1993. (146)

Sixel K.E., Podgorsak E.B. and Souhami L., *Cylindrical dose distributions in pseudodynamic rotation radiosurgery: an experimental study*, Med. Phys. **20**: 163-170, 1993. (79)

Souhami L. and Podgorsak E.B., *Radiosurgery: a review of clinical aspects*, in: Advances in Radiology and Oncology, T. Benulic, G. Sersa and V.

Kovac (eds.) Radiologia Iugoslavica, Ljubljana, Slovenia, 1992, pp. 151-166. (23,25,26,27,28,29,30)

Souhami L., Olivier A., Podgorsak E.B., Villemure J.-G., Pla M. and Sadikot A.F., *Fractionated dynamic stereotactic radiotherapy for intracranial tumours*, Cancer **68**: 2101-2108, 1991. (23)

Steiner L., *Treatment of arteriovenous malformations by radiosurgery*, in: Intracranial Arteriovenous Malformations, C.B. Wilson and B.M. Stein (eds), Williams and Wilkins, Baltimore, 1984, pp. 295-313. (23)

Steiner L., *Stereotactic radiosurgery with the Cobalt-60 gamma unit in the surgical treatment of intracranial tumours and arteriovenous malformations*, in: Operative Neurosurgical Techniques - Indications, Methods and Results, H.H. Schnidek, W.H. Sweet (eds.), W.B. Saunders, Philadelphia, 1988, pp. 515-529. (28)

Steiner L., Leksell L., Greits T., Forster D.M.C. and Backlund E.-O., *Stereotaxic radiosurgery for cerebral arteriovenous malformations. Report of a case*, Acta Chir. Scan. **138**: 459-464, 1972. (25)

Walker S., Bielajew A.F., Hale M.E. and Jette D., *Installation of EGS4 Monte Carlo dose on an 80386-based microcomputer*, Med. Phys. **19**: 305-306, 1992. (74)

Walton L., Bomford C.K. and Ramsden D., *The Sheffield stereotactic radiosurgery unit: physical characteristics and principles of operation*, Brit. J. Radiol. **60**: 897-906, 1987. (10,12)

Wierzbicki W., Sixel K.E. and Podgorsak E.B., *An analytical representation of radiosurgical depth dose data*, (abstract) Proceedings of the 39th meeting of the Canadian Organization of Medical Physicists (COMP) and the 19th meeting of the Canadian Medical and Biological

Engineering Society (CMBE), Ottawa, Ontario, May 12-15, pp. 258-259, 1993. (127)

Wierzbicki W., Sixel K.E. and Podgorsak E.B., *An analytical representation of radiosurgical depth dose data*, Phys. Med. Biol. **38**: (in press) 1993. (127)

Winston K.R. and Lutz W., *Linear accelerator as a neurosurgical tool for stereotactic radiosurgery*, Neurosurg. **22**: 454-464, 1988. (16)

Wu A., Lindner G., Maitz A.H., Kalend A.M., Lundsford L.D., Flickinger J.C. and Bloomer W.D., *Physics of gamma knife approach on convergent beams in stereotactic radiosurgery*, Int. J. Radiat. Oncol. Biol. Phys. **18**: 941-950, 1990. (10)